

# Advances in Fine Structure Optimizations of Layered Transition-Metal Oxide Cathodes for Potassium-Ion Batteries

Xuanpeng Wang,\* Zhitong Xiao, Kang Han, Xiao Zhang, Ziang Liu, Chen Yang, Jiashen Meng, Ming Li, Meng Huang, Xiujuan Wei, and Liqiang Mai\*

Potassium-ion batteries (PIBs) have attracted significant research interest in the context of driving the advancement of grid energy storage due to K's elemental abundance and high theoretical output voltage. The main challenge facing PIBs is to find suitable cathode materials with fast transport kinetics and stable framework structures to intercalate/de-intercalate the large-size  $K^+$ . Among these candidates, transition-metal layered oxides have excellent potential and have been extensively exploited due to their stable skeleton structure, simple synthetic chemistry, and high working potential. Herein, the current research status and prospects of layered transition-metal oxide cathodes are summarized, especially focussing on the fine structure optimization engineering and energy storage mechanism. In addition, a brief overview of the research on advanced characterization techniques for PIBs is introduced in detail. Finally, the main research directions and hot spots of new-type transition-metal layered oxide cathode are also predicted, in order to guide the future development of advanced PIBs.

Therefore, energy storage equipment and technology are essential to promote the development of human social civilization.

Sodium-ion batteries (SIBs) have been focused on special attention in energy storage field due to their abundant sodium resource reserves, high energy storage efficiency, and low-cost.<sup>[9–14]</sup> However, the commercialization of SIBs is also hindered by their low energy density, low power density, and short actual cycling life.<sup>[15,16]</sup> Recently, new-type potassium-ion batteries (PIBs) own huge advantage for grid storage because of the abundant resource of the K-containing raw materials and similar output potentials to lithium-ion batteries (LIBs).<sup>[17–24]</sup> Compared with LIBs and SIBs,<sup>[25]</sup> PIBs have a similar working principle, that is, the  $K^+$  shuttle forth and back between anode and cathode electrodes to achieve the energy storage (Figure 1).<sup>[26–31]</sup>

## 1. Introduction

With the increasingly prominent environmental problems and the continuous shortage of fossil energy, the development and application of new green/clean energy are imperative.<sup>[1–3]</sup> However, effective integration of new green/clean energy into the daily power grid is a great challenge urgently.<sup>[4–6]</sup> The applications of large-scale energy storage devices is the core technology of the accommodation and integration of new green/clean energy, and electrochemical energy storage technology is evaluated as an effective energy storage techniques in the current and future.<sup>[2,3,7,8]</sup>

Moreover, the advantages of PIBs are mainly reflected in the following aspects: 1) The earth reserves of potassium element resources are abundant. The earth's potassium element resource reserves are  $\approx 1000$  times that of lithium element resources (close to sodium element resource), and the cost of the electrolyte and electrode in PIBs is the lowest, compared with LIBs and SIBs.<sup>[19,32–34]</sup> 2) PIBs are expected to achieve high output voltage. The standard reduction potential of  $K^+/K$  ( $-2.93$  V) is closer to that of  $Li^+/Li$  ( $-3.04$  V), but 0.22 V lower than that of  $Na^+/Na$  ( $-2.71$  V).<sup>[29,35,36]</sup> 3) PIBs are expected to achieve excellent high-rate characteristics.  $K^+$  ions have weak Lewis acidity, and

X. Wang  
Department of Physical Science & Technology  
School of Science  
Wuhan University of Technology  
122 Luoshi Road, Wuhan, China  
E-mail: wxp122525691@whut.edu.cn

X. Wang, L. Mai  
Hubei Longzhong Laboratory  
Wuhan University of Technology (Xiangyang Demonstration Zone)  
Xiangyang, Hubei 441000, China

 The ORCID identification number(s) for the author(s) of this article can be found under <https://doi.org/10.1002/aenm.202202861>.

Z. Xiao, K. Han, X. Zhang, Z. Liu, C. Yang, J. Meng, M. Li, M. Huang, L. Mai  
School of Materials Science and Engineering  
State Key Laboratory of Advanced Technology for Materials Synthesis and Processing  
Wuhan University of Technology  
122 Luoshi Road, Wuhan 430070, China  
E-mail: mlq518@whut.edu.cn

X. Wei  
Guangzhou Key Laboratory of Clean Transportation Energy Chemistry  
School of Chemical Engineering and Light Industry  
Guangdong University of Technology  
Guangzhou 510006, China

DOI: 10.1002/aenm.202202861

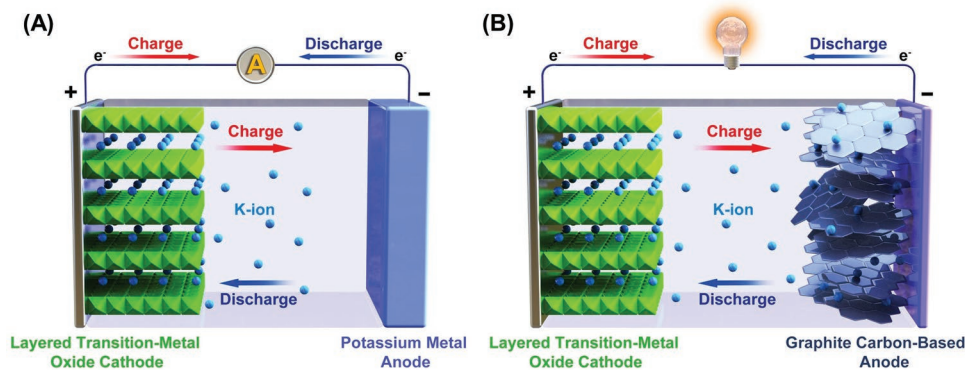


**Figure 1.** Schematic illustration of the cell configuration and operational mechanism of typical A) half and B) full PIBs.

solvated  $K^+$  ions show a smaller Stokes radius, resulting in the extremely high fluidity and fast transport kinetics of  $K^+$  ions in the electrolyte.<sup>[37–39]</sup> 4)  $K^+$  ion can be embedded in the graphite-based materials, which is similar to the behavior of  $Li^+$  ions.<sup>[40,41]</sup> However,  $Na^+$  ions cannot be embedded in graphite-based materials. Therefore, PIBs have an advantage over SIBs in developing commercial high-performance anode materials. 5) The safety issues of PIBs can be solved by Na/K alloying anode. The Na/K alloy is liquid at a certain ratio, which avoids the generation of K dendrites and provides new potentials for the advance of high-safety PIBs.<sup>[19,42–44]</sup> In addition, the Na/K alloy anode can provide a high capacity of  $\approx 580 \text{ mAh g}^{-1}$  and superior cycle performance.<sup>[45]</sup> 6) Al foil can be considered as a current collector instead of Cu foil on the anode side. The use of copper foil in PIBs as a current collector is avoided, and the overall manufacturing cost price of PIBs is reduced to a certain extent.<sup>[7,40]</sup>

Based on the above analysis, the development of PIBs is of great significance for the realization of large-scale application of high-energy and low-cost energy storage devices.<sup>[29]</sup> Nevertheless, because  $K^+$  ion has a larger ionic radius, and the insertion/extraction processes will cause serious structural degradation of the material skeleton, which seriously affects the actual rate performance and cycling life of PIBs.<sup>[37,46,47]</sup> Critical characteristics of the rechargeable secondary battery such as reversible specific capacity, output voltage, rate capability, and cycling stability are primarily determined by the intrinsic electrochemical properties of the cathodes.<sup>[48]</sup> Compared with  $Na^+$  ion, the radius of  $K^+$  ion is larger, and the atomic occupation will be different in similar structures. It is not suitable to directly use the derivative of the electrode materials of the SIBs as the electrode material of the PIBs.<sup>[49,50]</sup> Therefore, the main concern in the PIB system is to find suitable cathode materials with a robust frame structure upon the de-intercalation/intercalation of large-size  $K^+$ .<sup>[10,18,51]</sup>

In recent years, the research interests of PIBs cathode materials have been continuously growing, and the pioneering literature reports have been gradually increased. The reported PIB cathode materials are classified as four groups: layered transition-metal oxides, metal hexacyanometalates, organic compounds, and polyanionic compounds.<sup>[52]</sup> The layered transition-metal oxides are considered the most potential cathodes for SIBs and LIBs, so they have also drawn both scientific and practical attention in PIB system.<sup>[29,53–56]</sup> Metal hexacyanometalates compounds such as Prussian blue (white) also have a high

specific capacity as a cathode material, but the material has poor electronic conductivity, so it is difficult to improve the rate performance. Organic electrode materials exhibit the advantages of being renewable, green, low-cost, and high-capacity. However, the problem of high solubility in electrolyte, poor conductivity, and low density, especially, the lack of potassium-containing and insolubility organic cathodes, which greatly limits the applicability of organic cathode materials in PIBs. Polyanionic compounds usually have high electrochemical reaction stability and working voltage, but the disadvantage is that such materials have low ionic and electronic conductivities. And the larger molecular mass also lowers the specific capacity. Among these candidates, layered transition-metal oxides ( $A_xMO_2$ ,  $A = K, Na$ , and their combinations;  $M = V, Mn, Fe, Ni, Cr, Co$ , and their combinations) are particularly potential and have been extensively exploited due to their stable skeleton structure, simple synthetic chemistry, high output voltage, and feasibility for commercial production.<sup>[57–60]</sup> The first seminal work on potassium-based layered oxides ( $K_xCoO_2$ ) were reported at 1975.<sup>[61]</sup> Until 2016, Vaalma et al. developed the layered oxide  $K_{0.3}MnO_2$  as cathode materials for PIBs.<sup>[62]</sup> Since then, more and more research groups have studied various types of layered oxides with better electrochemical performance and deeper understanding of the potassium storage mechanism.<sup>[63]</sup>

Herein, we will summarize the current study advance and prospective of layered transition-metal oxide cathodes in PIBs, starting with the classifications, advantages, and challenges, followed by a detailed focus on the fine structure optimization and energy storage mechanisms along with their crystal structure, phase composition, structural characterization analysis, and electrochemical properties. In addition, a brief overview on advanced characterization techniques for PIBs will be introduced in detail. Finally, the main research directions and hot spots in the field of PIBs in the future will be presented along with prospects. Overall, this review will provide insights and perspectives into the engineer of new-type layered oxide cathodes for advanced PIBs.

## 2. Classifications, Advantages, and Challenges

In general, layered transition-metal oxides are classified based on the stacking order of alkali ions between edge-sharing  $MO_6$  octahedral layers. There are mainly two coordination

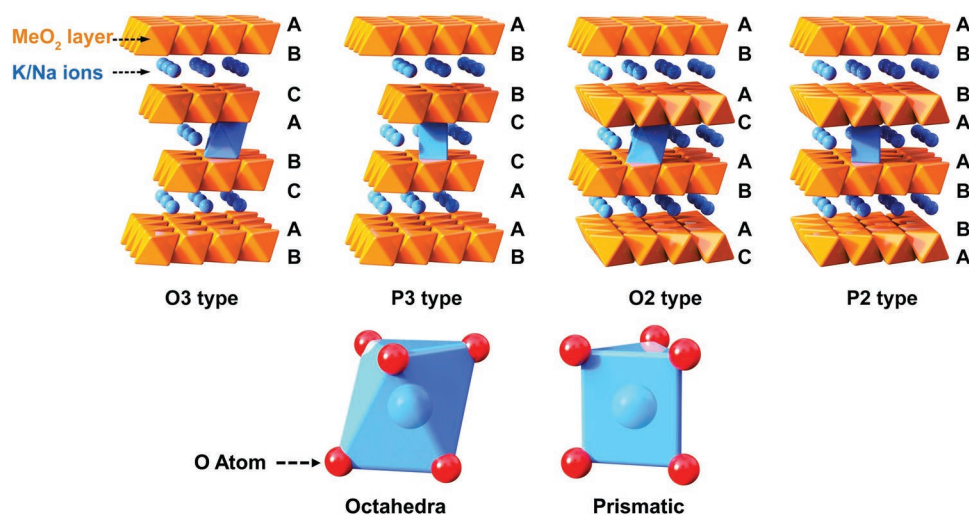


**Figure 2.** Schematic illustrations of the crystal structures of O3-, P3-, O2-, and P2- $A_{1-x}MeO_2$  ( $A = K, Na$ ).

environments for alkali ions in  $A_{1-x}MO_2$ : face shared prismatic (P) and edge-sharing octahedral (O) sites.<sup>[64]</sup> Here, the number of  $MO_6$  layers in one repetitive stacking unit is 3 or 2 (**Figure 2**). For instance, O2 and O3 phases are stacked in an ABAC and ABCABC pattern with the octahedral-alkali-metal, respectively. P3 and P2 phases are usually packed in the ABBCCA and ABBA manners with the prismatic-alkali-metal, respectively.<sup>[17]</sup>

At present, most of the reported layered oxides are K-containing compounds, only a few are Na-containing compounds. Most of the transition-metal elements are concentrated in the third period (Sc, Mn, V, Co, Cr, Ni, and Fe) of the periodic table, and there is only one transition-metal element (Ru) in the fourth period (**Figure 3**). Obviously, there are still many layered cathode materials composed of other transition-metal elements that have not been studied and reported as cathodes in PIBs, from the periodic table.

The redox energies of the  $M^{3+/4+}$  couples in  $K_xMO_2$  ( $M = Mn, V, Co, Cr, Ni, \text{ and } Fe$ ) are illustrated in **Figure 4**. Obviously,  $V^{3+/4+}$ ,  $Cr^{3+/4+}$ , and  $Fe^{3+/4+}$  redox couples exhibit the high potential in PIB systems (Figure 4A,B,D), and  $Mn^{3+/4+}$  and  $Co^{3+/4+}$  redox couples display moderate potential, while  $Ni^{3+/4+}$  redox couples show the lowest potential (Figure 4C,E,F). In addition, all the reported  $K_xMeO_2$  cathodes are referred to oxides, which are similar with the layered  $Na_xMO_2$ .<sup>[10,16]</sup> Although layered oxide cathodes generally exhibit high reversible specific capacity, it is still a tough work to improve the stability and thermal safety of layered compounds for their applications, particularly in PIBs.<sup>[16,58]</sup> The composition and arrangement modification of the  $MO_6$  octahedral layer may enhance the structural stability of layered oxides compounds by doping inactive high-energy element into the  $MO_6$  octahedral, such as Ti, Zr, Al, Cu, Ru, Nb, W, etc.<sup>[16,58,65–68]</sup>

According to the number of composed transition-metal elements, we divided the reported layered transition-metal oxides into three groups: single-, binary-, and multi-transition-metal oxides. A timeline summarizing the main milestones is illustrated in **Figure 5**, which indicates the history of the development of layered oxide for PIBs. As mentioned above, layered transition-metal oxide cathode materials typically undergo

extensive phase transitions during electrochemical cycling owing to the of  $K^+$  extraction/insertion. Interlayer stacking control, high-energy ion doping, surface modification/coating and interlamellar space optimization are believed effectively to alleviate the slow  $K^+$  transport kinetics and limited  $K^+$  storage sites caused by structural issues, according to the accumulated knowledge of the LIBs and SIBs systems. Therefore, some unique nano/micro-structures have also been introduced into K-containing layered transition-metal oxide to enhance its electrochemical potassium storage properties, such as interconnected  $K_{0.7}Fe_{0.5}Mn_{0.5}O_2$  nanowires,<sup>[51]</sup> P2- $K_{0.6}CoO_2$  microspheres,<sup>[69]</sup> P2- $K_{0.65}Fe_{0.5}Mn_{0.5}O_2$  microspheres,<sup>[70]</sup> bilayered  $\delta$ - $K_{0.51}V_2O_5$  nanobelts,<sup>[71]</sup> etc. The optimizing strategies, synthetic method, electrochemical properties, and energy storage mechanism of these unique nano/micro-structure cathodes will be discussed in this section.

## 3. Single-Transition-Metal Oxide Cathode

### 3.1. Co-Based Single-Transition-Metal Oxide Cathode

$Na_xCoO_2$  was an early option as the Na-containing oxide in the 1980s, and the structural variation of  $Na_xCoO_2$  was first studied via Delmas.<sup>[72,73]</sup> Reversible electrochemical  $K^+$  intercalation/deintercalation in P2- $Na_xCoO_2$  was first reported by Sada et al.<sup>[74]</sup> Phase-pure  $Na_{0.84}CoO_2$  was obtained via solution combustion preparation, achieved a satisfactory capacity of  $82 \text{ mAh g}^{-1}$ . This work indicates that  $Na_xCoO_2$  can be considered to be a suitable cathode material for  $K^+$  de-intercalation/intercalation.

$K_xCoO_2$  have been studied since the 1970s,<sup>[62,75]</sup> while its  $K^+$  intercalation/de-intercalation performances have not been verified until 2017 by Kim et al.<sup>[76]</sup> Therefore, the electrochemical behavior of  $A_xCoO_2$  ( $A = K, Na, Li$ ) compounds was compared among LIBs, SIBs, and PIBs. The structural stability of K ordering tendencies and phases in the O1/O3/P3  $K_xCoO_2$  were systematically studied by Van der Ven group.<sup>[77]</sup> Layered  $K_xCoO_2$  is made up of 2D  $CoO_2$  layers composed of  $CoO_6$  octahedra edge sharing, with K occupying positions between the layers.

Periodic Table of the Elements

**Figure 3.** Extract of periodic table showing the transition-metal elements that make K-containing and Na-containing layered transition-metal-oxide cathode materials, collected from the literature of PIBs.

Oxygen anions are arranged in a tightly packed triangular lattice, followed by ABABAB in O1 (Figure 6A), ABBCCA in P3 (Figure 6B), and ABCABC in O3 (Figure 6C). A hybrid stack consisting of interfacing layers alternating between O1 stacks and O3 or P3 stacks perpendicular to the  $\text{CoO}_2$  layer is also provided. (Figure 6D,E). When  $3/4 \leq x \leq 9/10$ , the  $\text{K}_x\text{CoO}_2$  material also has a highly distorted phase family, denoted as M (Figure 6F,G). The M phase is different from the O3/O1/P3 phases, which consists of undulating  $\text{CoO}_2$  layers alternating octahedral and prismatic coordination K bands in a single intercalation. The convex hull of each host is shown in Figure 6H. The global shell is bolded in black, indicating the ground state order of the different K components. O1 hosts are stable only at  $x = 0$ , mixed O1–O3 hosts are globally stable at  $x = 1/6$ , and O3 hosts are stable at  $x = 1/3$  or 1. P3 is stable at  $7/17 \leq x \leq 2/3$  and

M is stable at  $3/4 \leq x \leq 9/10$ . Structures initialized with O3 and P3 appear M-phase during energy relaxation. The calculated voltage profile of  $\text{K}_x\text{CoO}_2$  is shown in Figure 6I. Obviously, the predicted voltage curve is made up of a multitude of smaller steps and several obvious steps, each of which corresponds to a unique ground state order. This work reveals a new family of layered host structures in the high-K composition, consisting of undulating, highly strained  $\text{CoO}_2$  layers, allowing the existence of octahedral and triangular prismatic K-sites in each interlayer.

The reversible  $\text{K}^+$  de-intercalation/intercalation in  $\text{P2-K}_x\text{CoO}_2$  was first demonstrated by Ceder group.<sup>[76]</sup> Figure 7A exhibits the X-ray diffraction (XRD) pattern of  $\text{K}_{0.6}\text{CoO}_2$ . The layered structure is P2-type, and the  $P63/mmc$  space group is hexagonally symmetric (Figure 7B). The initial discharge capacity of  $\text{K}_{0.6}\text{CoO}_2$  cathode is  $80 \text{ mAh g}^{-1}$ , with  $\approx 2.7 \text{ V}$  average voltage

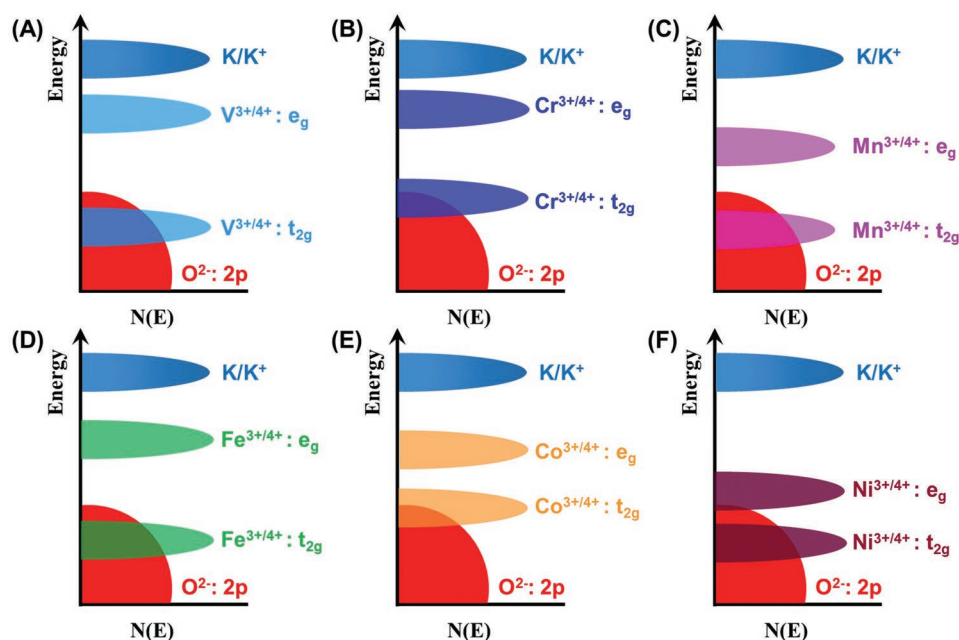


**Figure 4.** A–F) Schematic diagram of the redox energies of the  $\text{M}^{3+/4+}$  couple in  $\text{K}_x\text{MO}_2$  ( $\text{M} = \text{V}, \text{Cr}, \text{Mn}, \text{Fe}, \text{Co}, \text{Ni}$ ).

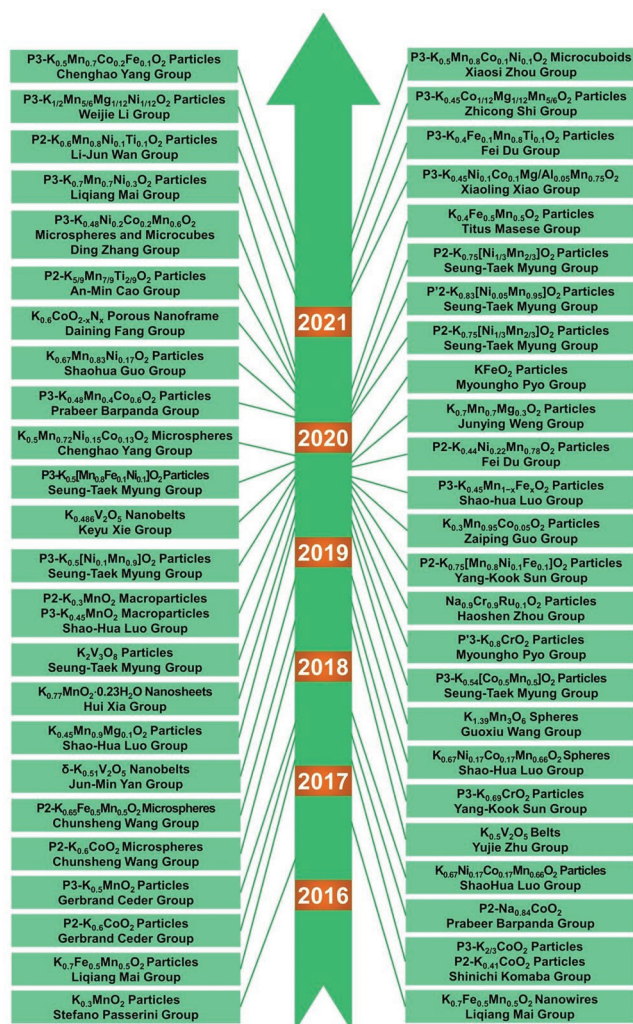


**Figure 5.** A brief chronology of layered transition-metal-oxide cathode materials for PIBs.

(Figure 7C). Multiple phase transformation upon K inserted/extracted are observed, which may be ascribed to the  $K^+$ /vacancy ordered structure. The  $K_{0.6}CoO_2$  cathode maintained  $\approx 60\%$  of its initial capacity after 120 cycles at  $100 \text{ mA g}^{-1}$ . Moreover, the practical capability of  $K_{0.6}CoO_2$  cathode is proved through fabricating PIB full cells coupled with a graphite anode.

Subsequently,  $P2/P3-K_xCoO_2$  and phase transition on the base of  $K^+$  content was studied by Komaba group.<sup>[78]</sup> Almost all diffraction peaks are matched with the  $P2$ -type layered phase when the  $K_{0.41}CoO_2$  obtained at  $600 \text{ }^\circ\text{C}$  (Figure 7D). The SEM image shows the morphology of 5–10 nm diameter hexagonal platelet particles (Figure 7E). However, all diffraction lines of  $K_{2/3}CoO_2$  prepared at  $400 \text{ }^\circ\text{C}$  match well with the  $P3$  type layered phase (Figure 7G). The  $P3-K_{2/3}CoO_2$  exhibits smaller hexagonal particles of  $\approx 500 \text{ nm}$  (Figure 7H). The  $K^+$  intercalation behaviors of  $P3-K_{2/3}CoO_2$  and  $P2-K_{0.41}CoO_2$  were tested in 2.0–3.9 V (Figure 7F,I). For  $P2-K_{0.41}CoO_2$ , the cell exhibits good capacity retention and excellent rate capability. For  $P3-K_{2/3}CoO_2$ , the cell performance resembles that of  $P2-K_{0.41}CoO_2$  (Figure 7I).

It is generally known that microscale hierarchical spheres composed of the nano-/micro- particles have been used as cathodes for SIBs and LIBs, which exhibit excellent electrochemical property.<sup>[79]</sup> The primary nanosized particles provide the rapid ion transport, while the microspheres increase the volumetric energy densities and alleviate the parasitic reactions.<sup>[65,80]</sup> The  $P2-K_{0.6}CoO_2$  microspheres layered cathode that be made up of primary aggregated nanoplates was successfully constructed a self-templating two-step approach (Figure 8A).<sup>[69]</sup> The structure and morphology of the  $CoCO_3$  precursors, the  $Co_3O_4$  intermediates, and final  $P2-K_{0.6}CoO_2$  microspheres were illustrated in Figure 8B–D. The SAED patterns revealed that the homogeneous distribution of Co, O, and K elements in  $P2-K_{0.6}CoO_2$  microspheres (Figure 8E–H). Moreover, the high-resolution transmission electron microscopy (HRTEM) image presents the 0.62 nm lattice fringes, which corresponds to the (002) planes (Figure 8I,J). Rietveld-refined XRD pattern demonstrates the layered structure of  $P2$ -type with hexagonal symmetry (Figure 8K). Obviously, the  $P2-K_{0.6}CoO_2$  microspheres cathode exhibits multiple pairs of redox peaks during cyclic voltammetry (CV) tests (Figure 8L). The multiple pairs of redox peaks is resulting from the changes in the  $K^+$ /vacancy ordering state.<sup>[11,81]</sup> The  $P2-K_{0.6}CoO_2$  microspheres exhibit a high capacity of  $82 \text{ mAh g}^{-1}$  at  $10 \text{ mA g}^{-1}$  in half PIB cells. Furthermore, PIB full cells based on hard carbon and  $P2-K_{0.6}CoO_2$  microspheres are assembled (Figure 8M–O). The PIB full cells delivered outstanding electrochemical property by showing an excellent capacity ( $71 \text{ mAh g}^{-1}$  at  $30 \text{ mA g}^{-1}$ ), a good fast rate capability ( $\approx 100\%$  recovery rate), and superior cycle stability ( $>80\%$  retention over 100 cycles).

### 3.2. Mn-Based Single-Transition-Metal Oxide Cathode

Manganese is a plentiful transition-metal element with crucial benefits based on capacity, sustainability, and affordability. Mn-based layered transition-metal oxides have stood out in PIBs because of their safety, stability and price advantage. Although the  $KMnO_2$  structure is non-layered and consists of  $[MnO_5]$  square pyramidal chains that share edges, the  $K_xMnO_2$  ( $0 < x < 1$ ) oxide crystallizes into layered  $P2$  and  $P3$  phases.<sup>[82]</sup> Moreover, even at the same synthetic temperature, the K content  $x$  significantly affects the  $K_xMnO_2$  structural type.<sup>[83]</sup> For example, Delmas et al. developed the preparation of  $P'2$ -type ( $0.55 < x < 0.67$ ) and  $P'3$ -type ( $x = 0.5$ ).<sup>[84]</sup> Liu et al.<sup>[85]</sup> reported  $P'2$ -type ( $x = 0.3$ ) and  $P'3$ -type ( $x = 0.45$ ). The  $K^+$  extraction/insertion electrochemical behavior of layered  $K_xMnO_2$  was first investigated by Stefano group.<sup>[62]</sup> Layered  $K_{0.3}MnO_2$  was prepared by pyrolyzing the  $KMO_4$ , forming an orthorhombic lattice with a  $Cmcm$  space group (Figure 9A). Layered  $K_{0.3}MnO_2$  cathode possesses a capacity of  $\approx 70 \text{ mAh g}^{-1}$  within 3.5–1.5 V and  $\approx 130 \text{ mAh g}^{-1}$  within 4.0–1.5 V in half cells (Figure 9B). It should be noted that layered  $K_{0.3}MnO_2$  presents a good cycling performance in 1.5–3.5 V after 685 cycles at  $279 \text{ mA g}^{-1}$  (Figure 9C). Subsequently, the electrochemical properties of layered  $P3-K_{0.5}MnO_2$  were reported by Ceder group.<sup>[86]</sup> The refined results of XRD patterns manifest a  $P3$ -type layered structure (Figure 9D). Two pronounced oxidation peaks were observed at  $\approx 4.1$  and  $\approx 3.7 \text{ V}$ , while their reduction peaks were not obvious

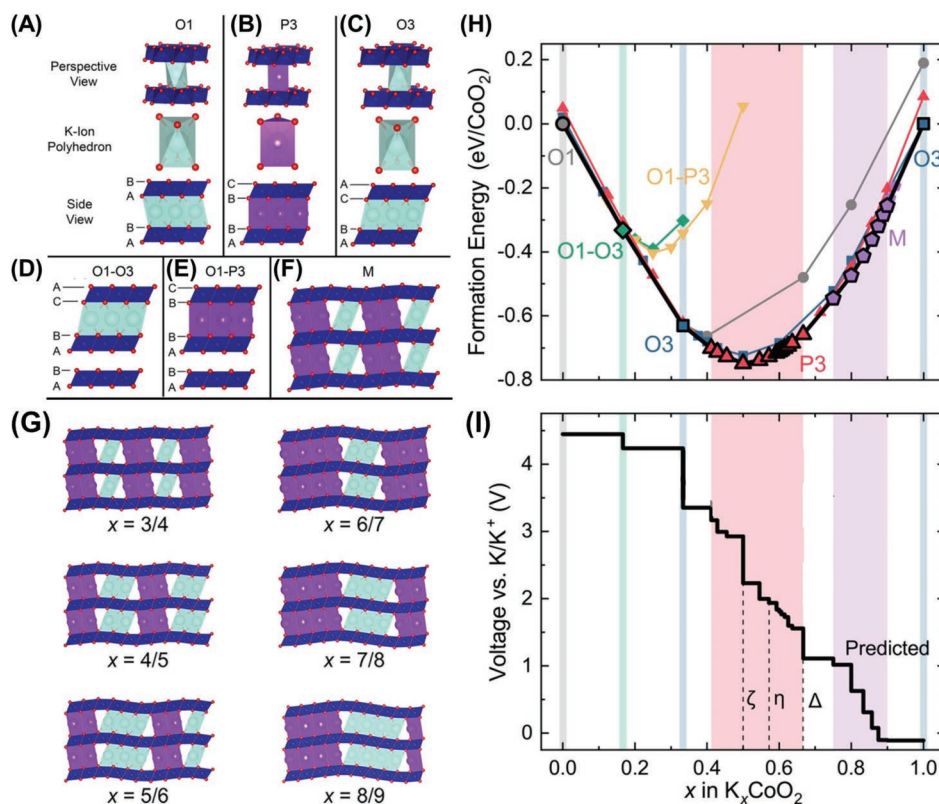


**Figure 6.** Side views show the stacking sequences of the O layers in A) O1, B) P3, C) O3, D) O1–O3, E) O1–P3, F) M, and G) relaxed M ground state structures at select compositions for  $K_x\text{CoO}_2$  host structures. H) Calculated zero-temperature phase diagram and I) predicted voltage curve derived from the zero-temperature formation energies of  $K_x\text{CoO}_2$  for  $0 \leq x \leq 1$ . Reproduced with permission.<sup>[77]</sup> Copyright 2019, American Chemical Society.

when scanning within 1.5–4.2 V. (Figure 9F). On the contrary, the redox peaks are well matched in 1.5–3.9 V (Figure 9H). These electrochemical behaviors suggest that the  $\text{K}^+$  de-intercalation and intercalation processes may lead to the irreversible structural variation at high-voltage region. Two obvious plateau-like features at  $\approx 4.1$  and  $\approx 3.7$  V were observed during charge process, while the voltage plateaus were less obvious during the subsequent cycles (Figure 9G). When cycling in 1.5–3.9 V, P3- $\text{K}_{0.5}\text{MnO}_2$  holds a plateau at  $\approx 3.6$  V and exhibits  $\approx 53$  and  $\approx 106$   $\text{mAh g}^{-1}$  specific capacities during the initial charging/discharging process, respectively (Figure 9I). It should be pointed out that the voltage curve of P3- $\text{K}_{0.5}\text{MnO}_2$  shares the same features as that of  $\text{K}_{0.3}\text{MnO}_2$ , and its layered structure is P2-type with an orthorhombic distortion. This indicates that the working voltage window depended on the distributions of K content and  $\text{K}^+$ /vacancy ordering, instead of by the polymorphism of  $\text{MnO}_2$  stacking same as found in  $K_x\text{CoO}_2$ .

It is generally believed that crystal water can expand the interlayer space, act as interlayer pillars, and suppress the Jahn–Teller effect of Na-birnessite in SIBs.<sup>[87]</sup> Gao et al. first investigated K-birnessite cathodes ( $\text{K}_{0.27}\text{Mn}_{0.98}\text{O}_2 \cdot 0.53\text{H}_2\text{O}$ ) for PIBs and achieved enhanced  $\text{K}^+$  ion transport kinetics.<sup>[88]</sup> However, the low K content limits its reversible capacity and structural stability, especially in the charged state, resulting in decreased cycling performance. Therefore, a high K-content birnessite with reinforced layered structure is designed by Lin et al. The “hydrothermal potassiation” strategy reported in

this paper achieves a significant increase in the K content in birnessite (Figure 9J).<sup>[10]</sup> This optimized birnessite can show an ultrahigh capacity of  $\approx 134$   $\text{mAh g}^{-1}$  at 100  $\text{mA g}^{-1}$  within 1.5–4.0 V (vs  $\text{K}^+/\text{K}$ ) and excellent cycling stability (Figure 9K,L). The  $\text{K}^+$  ion diffusion kinetics were enhanced as increasing K content, attributed to the concerted  $\text{K}^+$  ion diffusion kinetics in K slab and large interlayer space. It is particularly important that enough  $\text{K}^+$  ions are retained between the layers in the extract state, which can maintain the layered structure and inhibit the degradation of the structure after the delamination of  $\text{K}^+$  ions.

Surface modification is considered to be one of the easiest and most effective methods to enhancing the electrochemical capabilities of secondary battery systems.<sup>[89,90]</sup> Numerous coating materials such as  $\text{ZrO}_2$ ,<sup>[91,92]</sup>  $\text{TiO}_2$ ,<sup>[93–95]</sup>  $\text{Al}_2\text{O}_3$ ,<sup>[96,97]</sup> and  $\text{AlF}_3$ <sup>[98–100]</sup> have been applied to improve the cycle performance of layered transition-metal oxide cathodes for LIBs and SIBs. Among them,  $\text{AlF}_3$  coating can efficiently prevent the layered oxides from being attacked by the by-products, such as HF and  $\text{CO}_2$ , produced by the oxidation of electrolyte at high voltage, thereby stabilizing the electrolyte/electrode interface and preventing the generation of a robust cathode–electrolyte interphase film.<sup>[98,99,101,102]</sup>  $\text{AlF}_3$ -coated layered  $\text{K}_{1.39}\text{Mn}_3\text{O}_6$  microspheres ( $\text{AlF}_3@K_{1.39}\text{Mn}_3\text{O}_6$ ) are investigated as PIB cathode materials by Wang group.<sup>[103]</sup>  $\text{AlF}_3@K_{1.39}\text{Mn}_3\text{O}_6$  microspheres are prepared through a precipitation approach followed by heat treatment process (Figure 10A).

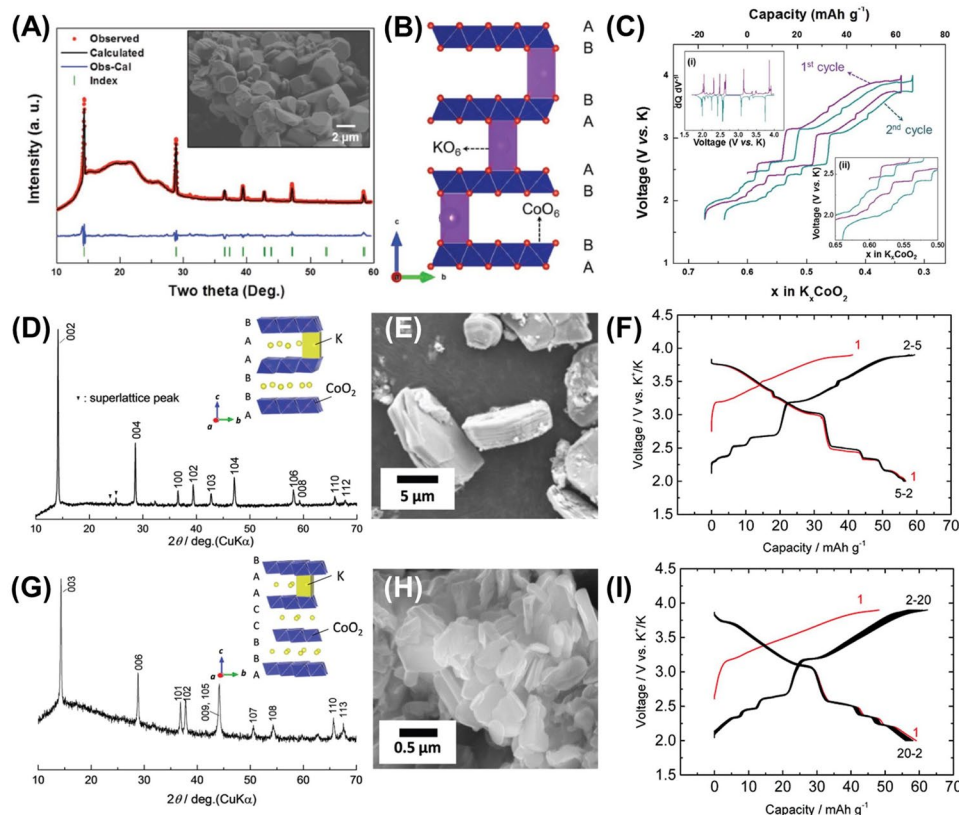


**Figure 7.** A) Rietveld-refined XRD profile, scanning electron micrograph, and B) crystal structure diagram of P2-K<sub>0.6</sub>CoO<sub>2</sub>. C) Typical charge/discharge profiles of P2-K<sub>0.6</sub>CoO<sub>2</sub> at a current rate of 2 mA g<sup>-1</sup> in the voltage window between 4.0 and 1.7 V versus K<sup>+/K</sup>. (Inset i): Derivative curve of the second cycle and inset ii): Enlarged charge/discharge curves with K content between 0.5 and 0.65). Reproduced with permission.<sup>[76]</sup> Copyright 2017, John Wiley and Sons. XRD patterns and SEM images of D, E) P2-K<sub>0.41</sub>CoO<sub>2</sub> and G, H) P3-K<sub>2/3</sub>CoO<sub>2</sub>. The corresponding crystal models are inserted. Charge/discharge curves of F) P2-K<sub>0.41</sub>CoO<sub>2</sub> and I) P3-K<sub>2/3</sub>CoO<sub>2</sub>. Reproduced with permission.<sup>[78]</sup> Copyright 2017, The Royal Society of Chemistry.

SEM image illustrates AlF<sub>3</sub>@K<sub>1.39</sub>Mn<sub>3</sub>O<sub>6</sub> microspheres maintain the morphology of hierarchical microsphere after AlF<sub>3</sub> coating (Figure 10B). The HRTEM image of AlF<sub>3</sub>@K<sub>1.39</sub>Mn<sub>3</sub>O<sub>6</sub> proves the formation of an amorphous AlF<sub>3</sub> coating layer (Figure 10C). No impurity was observed in the XRD results, which suggests that the AlF<sub>3</sub> surface coating does not influence the crystalline structure of K<sub>1.39</sub>Mn<sub>3</sub>O<sub>6</sub> microspheres (Figure 10D). After the first scan in CV curves, four couples of redox peaks at 3.5/3.83, 2.78/3.18, 2.53/2.95, and 2.14/2.51 V (Figure 10E). Moreover, AlF<sub>3</sub>@K<sub>1.39</sub>Mn<sub>3</sub>O<sub>6</sub> microspheres electrode exhibits better cycling stability than other two electrodes over 50 cycles (Figure 10F).

Luo and co-workers reported P2/P3-K<sub>x</sub>MnO<sub>2</sub> materials by the oxalate-assisted coprecipitation approach.<sup>[85]</sup> Despite the same preparation conditions, the K<sub>0.45</sub>MnO<sub>2</sub> shows smaller particle sizes and different structure compared to the K<sub>0.3</sub>MnO<sub>2</sub>. The crystalline structure of K<sub>0.3</sub>MnO<sub>2</sub> was studied by refined XRD and all the diffraction peaks corresponds with an orthorhombic system (Figure 10G). XRD pattern of the K<sub>0.45</sub>MnO<sub>2</sub> sample displays the rhombohedral system (Figure 10H). P3-K<sub>0.45</sub>MnO<sub>2</sub> gives an initial discharge capacity with 128.6 mAh g<sup>-1</sup> (Figure 10I). The CV curve clearly shows four oxidation peaks at approximately 3.80, 3.20, 2.90, and 2.50 V and corresponding four reduction peaks at 3.50, 2.76, 2.56, and 2.25 V (Figure 10J). K<sub>x</sub>MnO<sub>2</sub> maintains a reversible capacity of 71.5 mAh g<sup>-1</sup> with

70.8% capacity retention for  $x = 0.45$ , and 66.7 mAh g<sup>-1</sup> with 61.1% capacity retention for  $x = 0.3$  (Figure 10K). Moreover, the P3-K<sub>0.45</sub>MnO<sub>2</sub> exhibits higher rate capability than P2-K<sub>0.3</sub>MnO<sub>2</sub>. When recovered to 20 mA g<sup>-1</sup>, both the two K<sub>x</sub>MnO<sub>2</sub> materials exhibit good capability to recover capacity, which suggests outstanding stability of structure (Figure 10L).

### 3.3. V-Based Single-Transition-Metal Oxide Cathode

Layered vanadates have drawn extensive interest as cathodes for SIBs and LIBs because of their high specific capacities, outstanding electrochemical activity, multiple valence states, and diverse structures. A variety of layered potassium vanadates containing KV<sub>3</sub>O<sub>8</sub>,<sup>[104,105]</sup> K<sub>0.25</sub>V<sub>2</sub>O<sub>5</sub>,<sup>[106–109]</sup> and K<sub>x</sub>V<sub>2</sub>O<sub>5</sub><sup>[71,104,110–113]</sup> have been reported in secondary battery systems. Yan research group successfully prepared bilayered single-crystalline δ-K<sub>0.51</sub>V<sub>2</sub>O<sub>5</sub> nanobelts with large interlayered structure and an optimized growth orientation through a chemical pre-intercalation strategy.<sup>[71]</sup> The structural evolution from α-V<sub>2</sub>O<sub>5</sub> to KVO is illustrated in Figure 11A. Rietveld-refined XRD result demonstrated the monoclinic phase (Figure 11B). Figure 11C is the corresponding refined structural models. The bilayered KVO presents a nanobelt morphology (Figure 11D). The precise potential of KVO is further analyzed using the

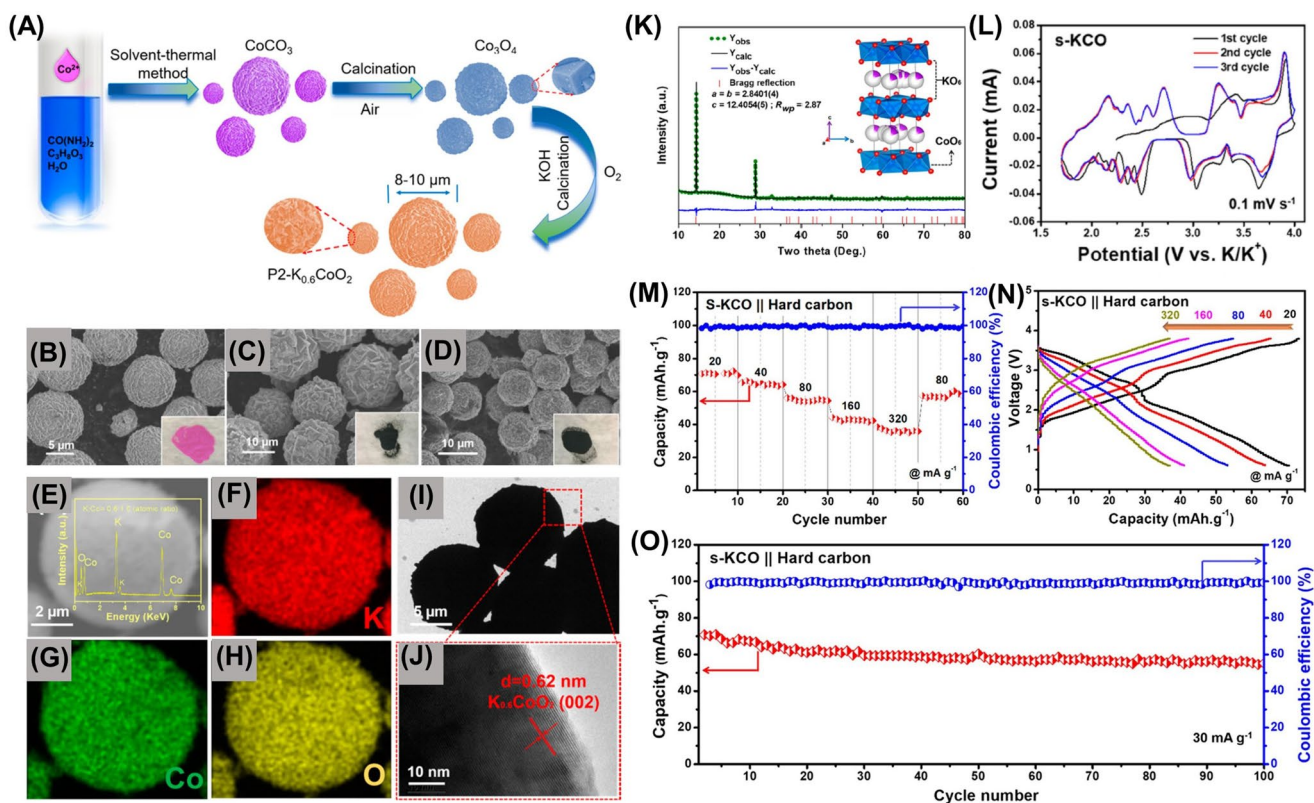


**Figure 8.** A) Schematic illustration for the synthesis of uniform P2-K<sub>0.6</sub>CoO<sub>2</sub> microspheres. SEM images of B) CoCO<sub>3</sub> precursor microspheres, C) Co<sub>3</sub>O<sub>4</sub> intermediate microspheres, and D) P2-K<sub>0.6</sub>CoO<sub>2</sub> microspheres. E) Typical SEM images of P2-K<sub>0.6</sub>CoO<sub>2</sub> microspheres and corresponding elemental mapping of F) K, G) Co, and H) O elements. I, J) Different magnification HRTEM images of P2-K<sub>0.6</sub>CoO<sub>2</sub> microspheres. K) Rietveld refinement of X-ray diffraction data and schematic structure of the P2-K<sub>0.6</sub>CoO<sub>2</sub> microspheres. L) CV curves for the s-KCO electrode at a scanning rate of 0.1 mV s<sup>-1</sup>. M) Rate capability of PIBs at different current rates, increasing from 20 to 320 mA g<sup>-1</sup>. N) Voltage–capacity curves of PIBs at different current densities, increasing from 20 to 320 mA g<sup>-1</sup>. O) Cycling performance of PIBs at a constant current of 30 mA g<sup>-1</sup>. Reproduced with permission.<sup>[69]</sup> Copyright 2019, American Chemical Society.

differential constant current ( $dQ/dV$ ) curve, exhibiting three distinct redox peaks (Figure 11E). KVO presented reversible capacities of 77.8 and 45.6 mAh g<sup>-1</sup> over 100 charge/discharge at 0.1 and 4 A g<sup>-1</sup>, respectively (Figure 11F).

As another potassium vanadate, K<sub>0.5</sub>V<sub>2</sub>O<sub>5</sub> was also studied as the PIB cathode material by Deng et al.<sup>[110]</sup> The K<sub>0.5</sub>V<sub>2</sub>O<sub>5</sub> cathode owns a large interlayer distance of ≈9.505 Å. The K<sub>0.5</sub>V<sub>2</sub>O<sub>5</sub> shows the phase of monoclinic phase with the C2/m space group (Figure 11G). The K<sub>0.5</sub>V<sub>2</sub>O<sub>5</sub> exhibits a belt-like morphology (Figure 11H). During the initial discharging process, a high discharge capacity of 87.5 mAh g<sup>-1</sup> is demonstrated (Figure 11I). Moreover, the K<sub>0.5</sub>V<sub>2</sub>O<sub>5</sub> exhibits a discharge capacity of 72.2 mAh g<sup>-1</sup> over 80 cycles (Figure 11J).

Jo et al.<sup>[114]</sup> reported K<sub>2</sub>V<sub>3</sub>O<sub>8</sub> with hendecahedrally coordinated K<sup>+</sup> ions as a PIB cathode material in 2019. The structural refinement of K<sub>2</sub>V<sub>3</sub>O<sub>8</sub>/C material was tetragonal structure with *P4bm* space group (Figure 11K). During the charging process, a voltage plateau was presented at 3.65 V, after which the voltage increased to 4.2 V. During the discharging process, the K<sub>2</sub>V<sub>3</sub>O<sub>8</sub>/C presents a large polarization, and the corresponding slope and voltage plateau appeared at low voltages as a downslope in 2.7–3.2 V and a voltage plateau at 2.5 V (Figure 11L). The cycling performance of K<sub>2</sub>V<sub>3</sub>O<sub>8</sub>/C exhibits good reversibility with capacity retention of ≈80% over 200 cycles, (Figure 11M).

### 3.4. Fe-/Cr-Based Single-Transition-Metal Oxide Cathode

Other single-transition-metal oxide cathodes, such as K<sub>x</sub>FeO<sub>2</sub>,<sup>[115–118]</sup> K<sub>x</sub>CrO<sub>2</sub>,<sup>[119–122]</sup> K<sub>x</sub>NiO<sub>2</sub>,<sup>[123,124]</sup> and K<sub>x</sub>ScO<sub>2</sub>,<sup>[20,125]</sup> have been reported and their electrochemical performances have been preliminarily researched in energy storage systems. Recently, KFeO<sub>2</sub> was prepared and measured as cathode for PIBs by Han et al.<sup>[117]</sup> It is curious that the crystal structure of KFeO<sub>2</sub> is not conventional layered structure. The KFeO<sub>2</sub> exhibits a reversible capacity of 60 mAh g<sup>-1</sup> (≈0.28 K<sup>+</sup>) with a plateau-like voltage at 3.43 V. Structural analysis of K<sub>0.7</sub>FeO<sub>2</sub> shows that the volume and quadrilateral corners of FeO<sub>4</sub> have undergone significant changes, resulting in decreased crystallinity and electrochemical performance of KFeO<sub>2</sub>. Using the electrochemical ion-exchange method, Sun et al. successfully prepared a P3-K<sub>0.69</sub>CrO<sub>2</sub>.<sup>[121]</sup> The P3-K<sub>0.69</sub>CrO<sub>2</sub> cathode exhibits a high capacity of 100 mAh g<sup>-1</sup> and a long cycle life of 1000 cycles with 65% retention at 100 mA g<sup>-1</sup>. In addition, the K<sup>+</sup> ion, hop into P3-K<sub>0.69</sub>CrO<sub>2</sub> structure quickly, which leads to excellent rate performance at 1000 mA g<sup>-1</sup>. Naveen et al. reported a solid-state synthesis of P3''-K<sub>0.8</sub>CrO<sub>2</sub> from commercially K<sub>2</sub>CrO<sub>4</sub>.<sup>[122]</sup> P3''-K<sub>0.8</sub>CrO<sub>2</sub> delivered 99% of the initial capacity at 1 C over 300 cycles, which is a significantly enhanced compared with O3-KCrO<sub>2</sub>. These above pioneering works demonstrate that

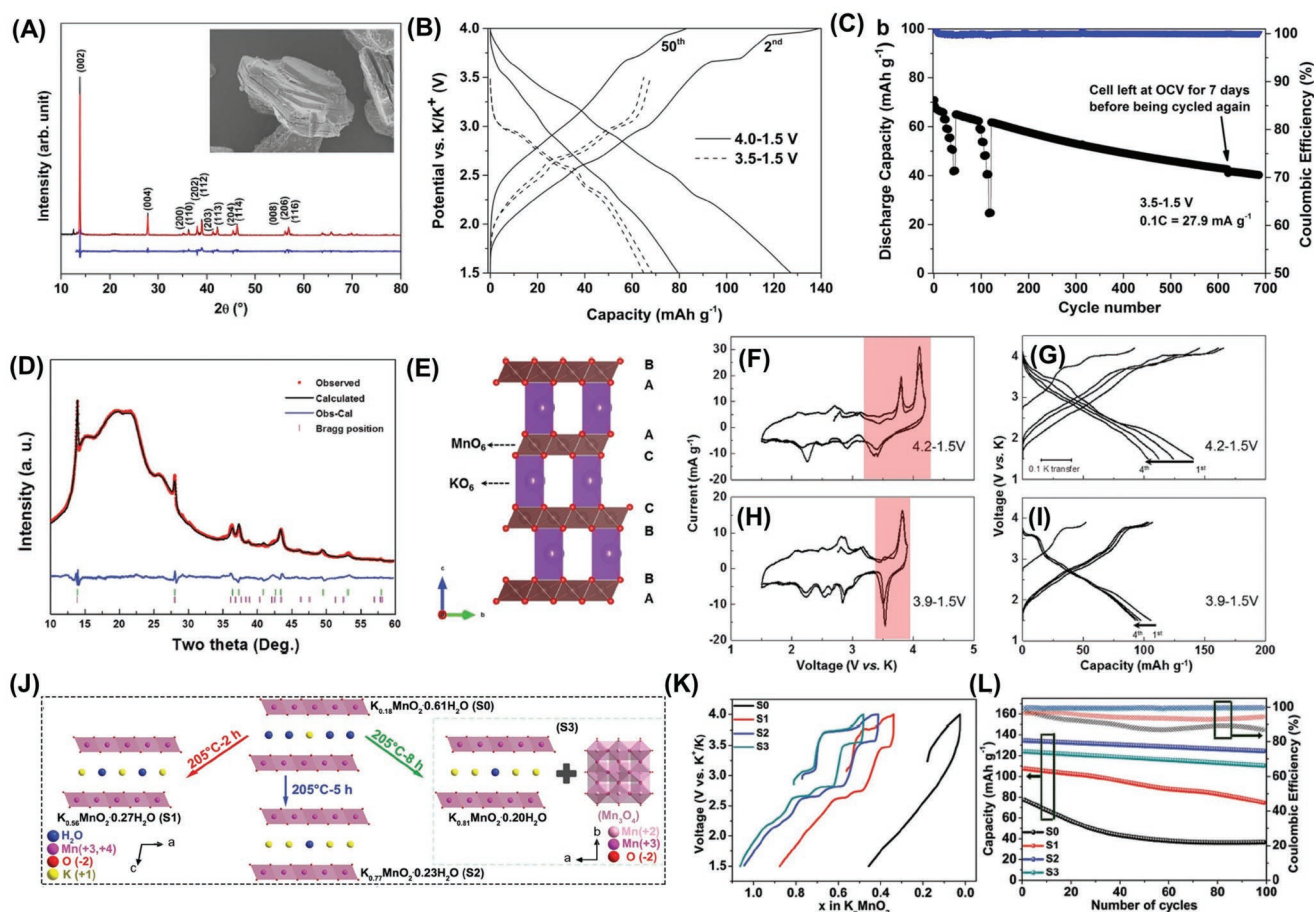


**Figure 9.** A) X-ray diffraction pattern and scanning electron micrographs of dried layered  $K_{0.3}MnO_2$ . B) Potential profiles of the 2nd and 50th cycle at 0.1 C in the voltage ranges 1.5–3.5 V and 1.5–4.0 V. C) Galvanostatic long-term cycling between 3.5 and 1.5 V at 0.1 C. Cycles 21–45 and 96–120 correspond to C-rate tests with 5 cycles at 0.2, 0.5, 1, 2, and 5 C. Reproduced with permission.<sup>[62]</sup> Copyright 2016, Elsevier. D) Rietveld-refined XRD profile and E) crystal structure diagram of  $K_{0.5}MnO_2$ . F,G) Cyclic voltammograms at a scan rate of  $0.03 \text{ mV s}^{-1}$  and H,I) galvanostatic voltage–capacity profiles of P3- $K_{0.5}MnO_2$  with two different voltage cutoffs. Reproduced with permission.<sup>[76]</sup> Copyright 2017, John Wiley and Sons. J) Structural evolutions from S0 to S1, S2, and S3 during the “hydrothermal potassiation.” K) The charge/discharge curves of the 1st formation cycle for the S0–S3 electrodes at a current density of  $100 \text{ mA g}^{-1}$ . L) Cycle performances and corresponding coulombic efficiencies of the four electrodes at a current density of  $100 \text{ mA g}^{-1}$  for 100 cycles. Reproduced with permission.<sup>[10]</sup> Copyright 2017, John Wiley and Sons.

single-transition-metal oxide can be applied as a promising PIB cathode, but that its intrinsic electrochemical behavior mechanism and further structural stabilization still need to be further explored. Due to the potassium storage mechanism of the material itself, the single-transition-metal oxides usually undergo the complex phase transition process upon  $K^+$  deintercalated/intercalated, resulting in structural deterioration and inferior cycling and rate performance.

## 4. Binary-Transition-Metal Oxide Cathode

To improve the electrochemical performance of single-transition-metal oxides, introducing other transition-metal elements to design binary-transition-metal oxide system or multi-transition-metal oxide system is an efficient approach. Through the synergistic effect between transition-metal ions, binary-transition-metal oxide, and multi-transition-metal oxide can exhibit excellent comprehensive electrochemical performance. The

binary-transition-metal oxide system can increase reversible capacity, smooth the voltage profiles and raise average working voltage as well as exhibit high  $K^+$  ion mobility, excellent conductivities, richer redox sites, and better electrochemical activities.<sup>[126–130]</sup> Owing to these features, some binary-transition-metal oxides have attracted increased attention for PIB systems.<sup>[51,59,70,126,131–136]</sup> The currently reported binary-transition-metal oxides mainly include: Fe/Mn-based, Ni/Mn-based, Co/Mn-based, Cr/Ru-based, and Cr/Ru-based.

### 4.1. Fe/Mn-Based Binary-Transition-Metal Oxide Cathode

Layered Fe/Mn-based oxides combination with high operating voltage originated from  $Fe^{3+}/Fe^{4+}$  and large capacity originated from  $Mn^{3+}/Mn^{4+}$  stand out as a good choice. Wang et al. studied a novel interconnected  $K_{0.7}Fe_{0.5}Mn_{0.5}O_2$  nanowires for the first time.<sup>[51]</sup> The XRD pattern shows that the  $K_{0.7}Fe_{0.5}Mn_{0.5}O_2$  is a layered structure of P3-type with  $R3m$  space group

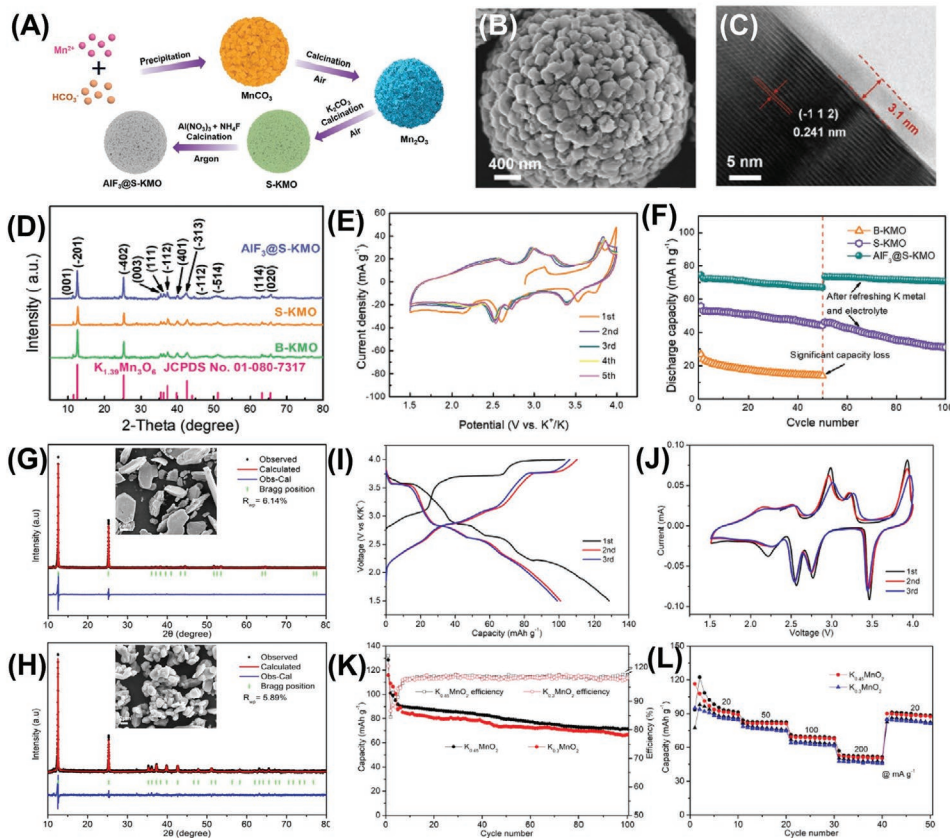


**Figure 10.** A) Schematic illustration of the synthesis process of  $\text{AlF}_3@K_{1.39}\text{Mn}_3\text{O}_6$  microspheres. B) SEM images and C) HRTEM image of  $\text{AlF}_3@K_{1.39}\text{Mn}_3\text{O}_6$  microspheres. D) XRD patterns of  $K_{1.39}\text{Mn}_3\text{O}_6$  blocks,  $K_{1.39}\text{Mn}_3\text{O}_6$  microspheres, and  $\text{AlF}_3@K_{1.39}\text{Mn}_3\text{O}_6$  microspheres. E) Cyclic voltammetry of  $\text{AlF}_3@K_{1.39}\text{Mn}_3\text{O}_6$  microsphere electrode between 1.5 and 4 V (vs  $\text{K}^+/\text{K}$ ) at a scan rate of  $0.1 \text{ mV s}^{-1}$ . F) Cycling performance of cells with  $K_{1.39}\text{Mn}_3\text{O}_6$  blocks,  $K_{1.39}\text{Mn}_3\text{O}_6$  microspheres, and  $\text{AlF}_3@K_{1.39}\text{Mn}_3\text{O}_6$  microspheres at  $50 \text{ mA g}^{-1}$  before and after refreshing the potassium metal anodes and electrolyte. Reproduced with permission.<sup>[103]</sup> Copyright 2019, John Wiley and Sons. XRD patterns, Rietveld refinement plot and SEM images of the as-prepared G)  $\text{P2-K}_{0.3}\text{MnO}_2$  and H)  $\text{P3-K}_{0.45}\text{MnO}_2$ . I) Galvanostatic charge–discharge curves of the  $\text{P3-K}_{0.45}\text{MnO}_2$  between 1.5 and 4 V at a rate of  $20 \text{ mA g}^{-1}$ , J) cyclic voltammetry of the  $\text{P2-K}_{0.3}\text{MnO}_2$ , K) cycling performance, and L) rate capabilities of  $\text{P2-K}_{0.3}\text{MnO}_2$  and  $\text{P3-K}_{0.45}\text{MnO}_2$  at  $20 \text{ mA g}^{-1}$ . Reproduced with permission.<sup>[85]</sup> Copyright 2019, Elsevier.

(Figure 12A). The individual  $\text{K}_{0.7}\text{Fe}_{0.5}\text{Mn}_{0.5}\text{O}_2$  nanowires exhibited the diameters of 50–150 nm and numerous particles are interconnected (Figure 12B). In GITT discharge test, a high theoretical discharge capacity of  $220 \text{ mAh g}^{-1}$  is exhibited in the  $\text{K}_{0.7}\text{Fe}_{0.5}\text{Mn}_{0.5}\text{O}_2$  nanowires (Figure 12C). The CV curves present two oxidation peaks at 2.77 and 2.33 V during the initial charge process (Figure 12D). Followed by cathodic process, two reduction peaks at 1.78 and 2.33 V appeared. The initial discharge capacity of  $\text{K}_{0.7}\text{Fe}_{0.5}\text{Mn}_{0.5}\text{O}_2$  nanowires is as high as  $178 \text{ mAh g}^{-1}$  at  $20 \text{ mA g}^{-1}$ . Furthermore, a capacity of  $125 \text{ mAh g}^{-1}$  is maintained over 45 cycles with  $\approx 70\%$  capacity retention (Figure 12E). When measured at  $1000 \text{ mA g}^{-1}$ ,  $\approx 87\%$  capacity retention after 450 discharge/charge is obtained (Figure 12F). The full cells are fabricated by combining  $\text{K}_{0.7}\text{Fe}_{0.5}\text{Mn}_{0.5}\text{O}_2$  nanowires with soft carbon (Figure 12G). The lighted LED belts powered by full cells demonstrated practical application ability (Figure 12H). The full cell exhibits a capacity of  $82 \text{ mAh g}^{-1}$  at  $40 \text{ mA g}^{-1}$  and an impressive capacity retention of  $\approx 90\%$  over 50 discharge/charge (Figure 12I). Moreover, the full cell also exhibits a good rate capability (Figure 12J). Subsequently, Wang and co-workers synthesized homogeneous  $\text{P2-K}_{0.65}\text{Fe}_{0.5}\text{Mn}_{0.5}\text{O}_2$  microspheres

through a modified solvent-thermal approach (Figure 12K).<sup>[70]</sup> The XRD data of the prepared  $\text{P2-K}_{0.65}\text{Fe}_{0.5}\text{Mn}_{0.5}\text{O}_2$  matches well the layered structure of P2-type with a  $P63/mmc$  space group (Figure 12L). The HRTEM image presents that the hierarchical  $\text{K}_{0.65}\text{Fe}_{0.5}\text{Mn}_{0.5}\text{O}_2$  particles are made up of agglomerated nanometers (Figure 12M). The Mn, Fe, O, and K elements are homogeneous distributed on  $\text{P2-K}_{0.65}\text{Fe}_{0.5}\text{Mn}_{0.5}\text{O}_2$  microspheres (Figure 12N,O). The two redox peaks during the low voltage range in the CV curves are attributed to  $\text{Mn}^{4+}/\text{Mn}^{3+}$  redox couple. While one redox peak during the high voltage range is fit for  $\text{Mn}^{3+}/\text{Mn}^{4+}$  redox couple.  $\text{Fe}^{3+}/\text{Fe}^{4+}$  redox couple (Figure 12P). When tested back to  $0.1 \text{ A g}^{-1}$ ,  $\text{P2-K}_{0.65}\text{Fe}_{0.5}\text{Mn}_{0.5}\text{O}_2$  microspheres possessed a high reversible capacity of  $104 \text{ mAh g}^{-1}$  (Figure 12Q).

#### 4.2. Ni/Mn-Based Binary-Transition-Metal Oxide Cathode

In Ni/Mn-based layered oxides, the multi-electron redox reaction of successive  $\text{Ni}^{2+}/\text{Ni}^{3+}$  and  $\text{Ni}^{3+}/\text{Ni}^{4+}$  can give rise to the energy density with high voltage range. Moreover, the

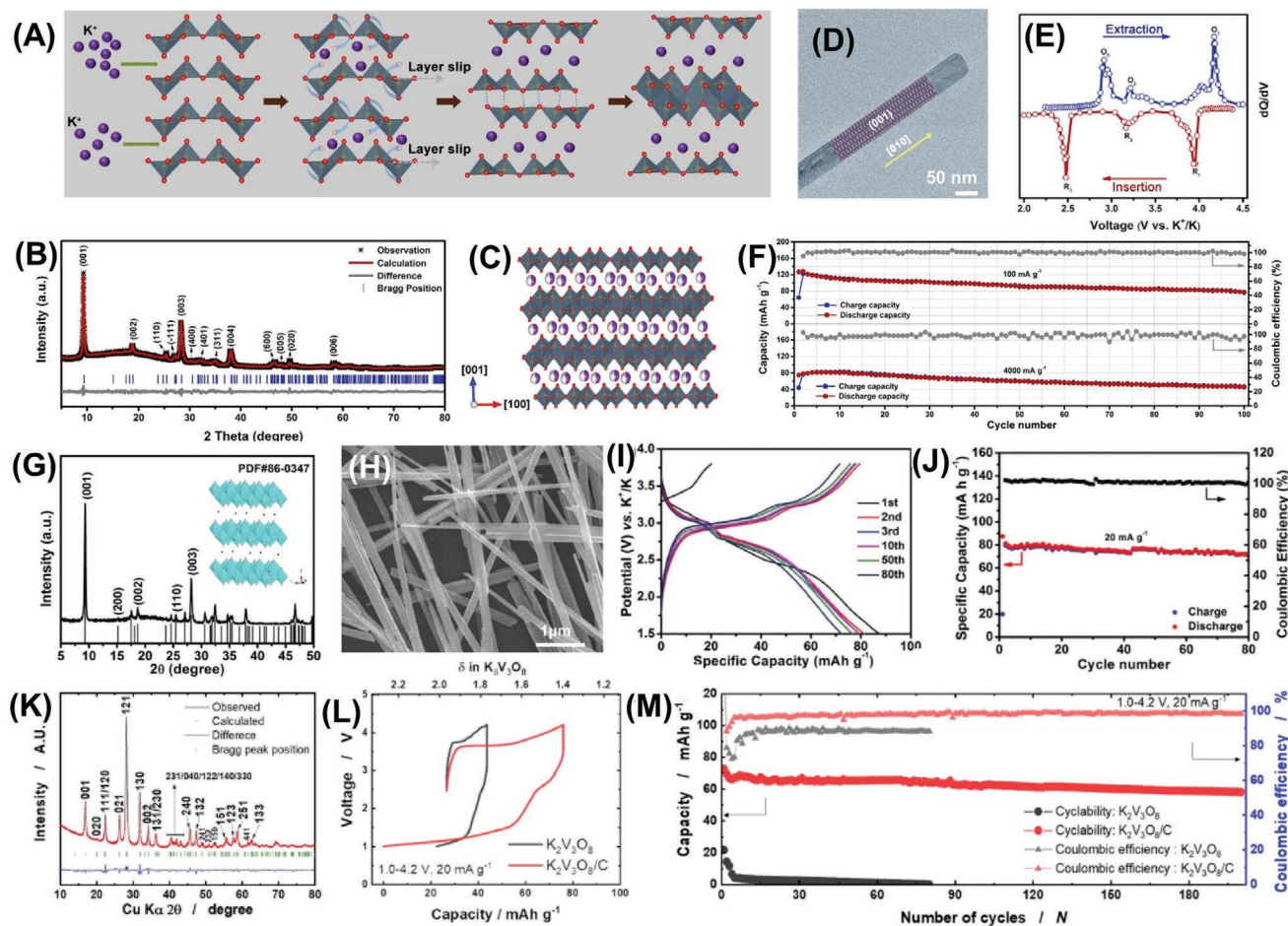


**Figure 11.** A) Schematic diagrams of the structural evolution from  $\alpha$ - $V_2O_5$  to KVO. B) XRD pattern, C) crystal structure schematic, and D) TEM images of KVO of the KVO. E)  $dQ/dV$  curves of KVO at a current density of  $30 \text{ mA g}^{-1}$ . F) Cycle performance of the KVO electrodes at different current densities. Reproduced with permission.<sup>[71]</sup> Copyright 2019, Elsevier. G) The Powder XRD pattern and crystal structure of  $K_{0.5}V_2O_5$ . H) FESEM image of  $K_{0.5}V_2O_5$ . I) Galvanostatic charge/discharge voltage profiles and J) cycling performance when the  $K_{0.5}V_2O_5$  was first charged to 3.8 V (vs  $K^+/K$ ) at a current density of  $20 \text{ mA g}^{-1}$ . Reproduced with permission.<sup>[110]</sup> Copyright 2018, John Wiley and Sons. K) Rietveld refinement of XRD data for  $K_2V_3O_8/C$  composite. L) The initial charge and discharge profile of  $K_2V_3O_8$  and  $K_2V_3O_8/C$  composite electrodes; M) cyclability of  $K_2V_3O_8/C$  composite. Reproduced with permission.<sup>[114]</sup> Copyright 2019, Elsevier.

substitution of  $Mn^{3+}$  by a small amount of  $Ni^{2+}$  is demonstrated as an effective approach to improve the electrochemical performance. Zhang et al. synthesized a  $P2$ - $K_{0.44}Ni_{0.22}Mn_{0.78}O_2$  with excellent structural stability and high reversible capacity.<sup>[126]</sup> Rietveld refinement shows that the  $p2$ -type material pertains hexagonal symmetry and the  $P63/mmc$  space group (Figure 13A).  $K_{0.44}Ni_{0.22}Mn_{0.78}O_2$  crystallizes as hexagonal close-packed crystals with typical oxygen layer ABBA stacking (Figure 13B). The transition metals oxidation states in  $K_{0.44}Ni_{0.22}Mn_{0.78}O_2$  were analyzed by X-ray photoelectron spectroscopy (XPS) (Figure 13C,D). The two redox peaks in measured CV curves originated from the stepped oxidation of  $Ni^{2+}$  into  $Ni^{3+}$  and  $Ni^{4+}$ . During the low voltage region ( $<2.75 \text{ V}$ ), two redox peaks at 2.61/2.40 and 2.23/2.02 V are attributed to the redox reactions of Mn (Figure 13E). In the rate performance test,  $K_{0.44}Ni_{0.22}Mn_{0.78}O_2$  possessed a reversible capacity of  $112 \text{ mAh g}^{-1}$  at  $20 \text{ mA g}^{-1}$  (Figure 13F). Moreover, the  $K_{0.44}Ni_{0.22}Mn_{0.78}O_2$  retained a capacity retention of 67% over 500 cycles (Figure 13G). Encouraged by good structural reversibility

and outstanding K storage property of  $K_{0.44}Ni_{0.22}Mn_{0.78}O_2$ , the full cell was fabricated against soft carbon (Figure 13H). It could exhibit an initial discharge capacity of  $69.2 \text{ mAh g}^{-1}$  and 90% capacity retention over 500 times (Figure 13I,J).

A study proposed  $P2$ - $K_{0.75}[Ni_{1/3}Mn_{2/3}]O_2$ , prepared by electrochemical ion-exchange as a PIB cathode with excellent electrochemical property.<sup>[131]</sup> The presence of  $K^+$  at vacant atomic sites along the ab plane between infinite layers consist of  $[Ni, Mn]O_6$  octahedra (Figure 14A). The detailed structural information of  $K_{0.75}[Ni_{1/3}Mn_{2/3}]O_2$ , that is, the  $P2$  layer structure and the  $P63/mmc$  space group, were verified by XRD patterns. (Figure 14B). The particle shape is block with a size of  $2 \mu\text{m}$  (Figure 14C). The elemental mapping figure demonstrated an evenly distribution of Ni, K, and Mn elements, while the Na element was not detectable (Figure 14D).  $P2$ - $K_{0.75}[Ni_{1/3}Mn_{2/3}]O_2$  demonstrates a high capacity of  $110 \text{ mAh g}^{-1}$  at  $20 \text{ mA g}^{-1}$  and a satisfactory cycle life over 300 cycles (Figure 14E). Moreover, it shows decent rate capability with  $91 \text{ mAh g}^{-1}$  at  $1400 \text{ mA g}^{-1}$  (Figure 14F,G).

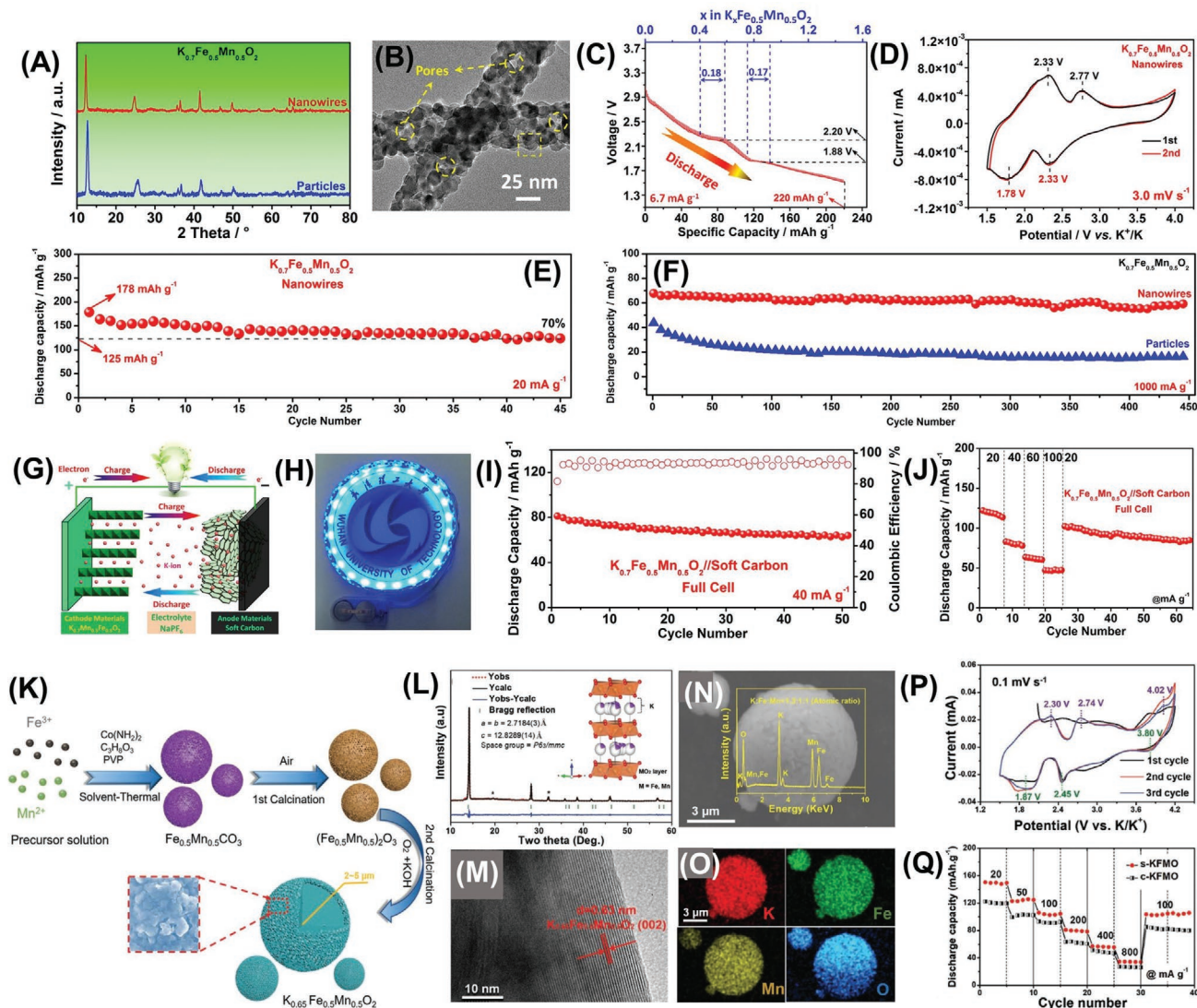


**Figure 12.** A) XRD patterns of interconnected  $K_{0.7}Fe_{0.5}Mn_{0.5}O_2$  nanowires and  $K_{0.7}Fe_{0.5}Mn_{0.5}O_2$  particles. B) TEM image of interconnected  $K_{0.7}Fe_{0.5}Mn_{0.5}O_2$  nanowires. C) The GITT test for interconnected  $K_{0.7}Fe_{0.5}Mn_{0.5}O_2$  nanowires tested at a current density of  $6.7 \text{ mA g}^{-1}$  in a potassiation process. D) Cycling performance tested at  $20 \text{ mA g}^{-1}$ . E) Rate performance of the PIBs. F) Reproduced with permission.<sup>[51]</sup> Copyright 2019, American Chemical Society. G) Schematic illustration of the K-ion full battery. H) The lighted LED belts driven by the PIBs. I) Cycling performance at  $100 \text{ mA g}^{-1}$  and J) rate performance of the PIBs. Reproduced with permission.<sup>[51]</sup> Copyright 2019, American Chemical Society. K) Schematic illustration for the synthesis of uniform P2- $K_{0.65}Fe_{0.5}Mn_{0.5}O_2$  microspheres with hierarchical structure. L) Pawley refinement of powder X-ray diffraction data, the inset is the schematic structure of P2- $K_{0.65}Fe_{0.5}Mn_{0.5}O_2$  microspheres (s-KFMO). M) TEM image of s-KFMO particles. N) Typical SEM image of s-KFMO particles and corresponding elemental mapping of O) K, Fe, Mn, and O elements. P) CV curves for the s-KFMO electrode at a scanning rate of  $0.1 \text{ mV s}^{-1}$ . Q) Rate capability of s-KFMO and c-KFMO electrodes at current rates of 20, 50, 100, 200, 400, 800  $\text{mA g}^{-1}$ . Reproduced with permission.<sup>[70]</sup> Copyright 2018, John Wiley and Sons.

#### 4.3. Cr/Ru-Based Binary-Transition-Metal Oxide Cathode

Zhang and coworkers reported a layered oxide through electrochemical ion-exchange from  $Na_{0.9}Cr_{0.9}Ru_{0.1}O_2$  (NCRO) as cathode material for PIBs.<sup>[59]</sup> After the first discharge, the uniform lattice fringes with  $0.552 \text{ nm}$  interlayer spacing of the cathode are fitted by the (003) plane of the Na-containing O3 type layer structure (Figure 14H). The HRTEM image also demonstrated different lattice fringes with  $0.625 \text{ nm}$  d-spacing, belongs to (003) plane of the K-containing P3-type layered structure (Figure 14I). The XRD patterns present a two-phase structure,

which is consistent with the d-spacing of  $0.625$  and  $0.552 \text{ nm}$  (Figure 14J). The NCRO fully varies from the initial O3 to P3 after 400 cycles (Figure 14K). According to the charge capacity of  $96.1 \text{ mAh g}^{-1}$ , the chemical compositions of charged NCRO can be determined as  $Na_{0.5}Cr_{0.9}Ru_{0.1}O_2$ . When discharged to  $1.5 \text{ V}$ ,  $0.38 \text{ K}^+$  ions can be accommodated in the cathode material, so its chemical formula should be  $K_{0.38}Na_{0.5}Cr_{0.9}Ru_{0.1}O_2$  (Figure 14L). When tested at  $0.1 \text{ C}$  in rate tests, it could deliver a specific discharge capacity of  $91.9 \text{ mAh g}^{-1}$  (Figure 14M). Moreover, NCRO exhibits a good capacity retention of  $81.2\%$  over 500 discharge/charge at  $500 \text{ mA g}^{-1}$  (Figure 14N).

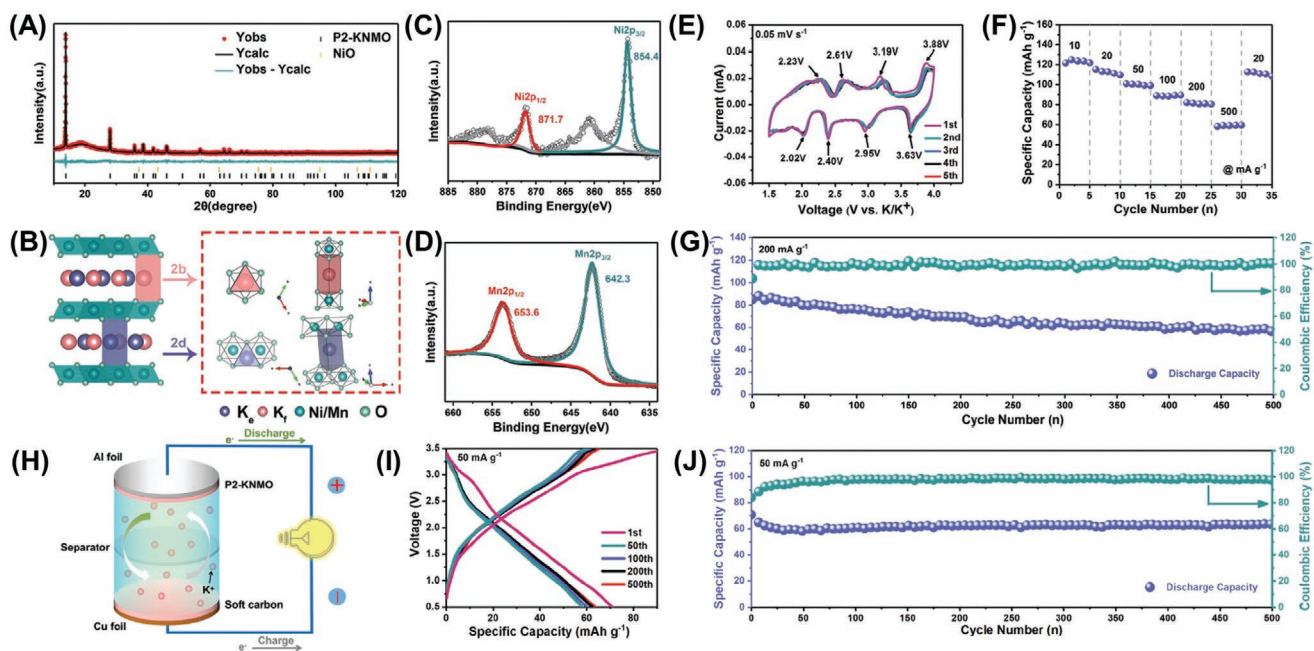


**Figure 13.** A) XRD Rietveld refinement of  $K_{0.44}Ni_{0.22}Mn_{0.78}O_2$  material. B) Schematic illustration of the hexagonal  $K_{0.44}Ni_{0.22}Mn_{0.78}O_2$  obtained from Rietveld refinement of XRD data. XPS spectra for C) Ni 2p and D) Mn 2p. E) CV curves for the P2- $K_{0.44}Ni_{0.22}Mn_{0.78}O_2$  electrode at a scanning rate of  $0.05 \text{ mV s}^{-1}$ . F) Rate capability of P2- $K_{0.44}Ni_{0.22}Mn_{0.78}O_2$ . G) Cycling performance of P2- $K_{0.44}Ni_{0.22}Mn_{0.78}O_2$  at  $200 \text{ mA g}^{-1}$ . H) Schematic illustration of the PIBs. I) Electrochemical charge–discharge voltage profiles and J) cycling performance of PIBs at a constant current of  $50 \text{ mA g}^{-1}$ . Reproduced with permission.<sup>[126]</sup> Copyright 2019, John Wiley and Sons.

#### 4.4. Co/Mn-Based Binary-Transition-Metal Oxide Cathode

Although cobalt resources are relatively expensive, it is undeniable that by replacing Mn with Co, the Jahn–Teller effect of  $Mn^{3+}$  can be suppressed, thereby effectively avoiding the structural disorder of the material during the  $K^+$  intercalation/deintercalation. Moreover, increasing the Co content can also smooth the voltage curve, which may contribute to the enhanced structural stability. Choi et al. synthesized  $P3-K_{0.54}[Co_{0.5}Mn_{0.5}]O_2$  material by occupying half of Mn with Co.<sup>[134]</sup> It demonstrated a specific capacity of  $120.4 \text{ mAh g}^{-1}$ , and the charge/discharge curve is smooth, which may be due to the increasement of the Mn average valence caused by introduction of Co, thereby inhibiting the Jahn-Teller effect of  $Mn^{3+}$  (Figure 15A). Meanwhile, the  $K_{0.54}[Co_{0.5}Mn_{0.5}]O_2$  shows good rate capability at  $500 \text{ mA g}^{-1}$ . Such performance is because of the overlap of the  $O2p$  orbital with the  $Co^{4+/3+}$  redox pair and the low activation energy of the  $K^+$  migration (Figure 15B). Furthermore, the in situ XRD measurement demonstrated that the  $K_{0.54}[Co_{0.5}Mn_{0.5}]O_2$  experiences single-phase reactions and reversible structural variation during the  $K^+$  de-intercalation/intercalation (Figure 15C). The coexistence of Mn and Co between the transition-metal layer is efficient in enhancing the layered stability by tuning the degree of irreversible transition, thereby providing robust stability for long cycle life and excellent rate performance. Sada et al. prepared  $P3-K_{0.48}Mn_{0.4}Co_{0.6}O_2$  via solid-phase approach.<sup>[137]</sup> Despite its high redox voltage of 3.0 V, it exhibits only a capacity of  $65 \text{ mAh g}^{-1}$  within 1.0–4.2 V, desorbed from the pristine material structure (Figure 15D,E). All these experimental results demonstrate that a properly balanced composition is crucial to obtain

outstanding electrochemical performance in Co/Mn-based binary-transition-metal oxide.

#### 4.5. Mg/Mn-Based and Ti/Mn Binary-Transition-Metal Oxides Cathode

The above-mentioned binary-transition-metal oxides are all composed of two electrochemically active elements. In addition, the electrochemically inert elements, such as Mg and Ti, can also be introduced, which usually improves the stability of the electrode materials. Liu et al. synthesized  $K_{0.45}Mn_{0.9}Mg_{0.1}O_2$  by doping 10% Mg into layered Mn-based oxides.<sup>[83]</sup> This material delivered a capacity of  $81 \text{ mAh g}^{-1}$  and good cycling performance (75% capacity retention of over 100 cycles), which is better than the undoped  $K_{0.45}MnO_2$  material. The good performance is ascribed to the expanded interlayer spacing and the reduced irreversible phase transition during depotassium/potassium by Mg doping. Additionally, the incorporation of Mg can also form a stable P3 phase and accelerate the diffusion of  $K^+$  in the material. A combined strategy of morphology modification and Mg doping can further enhance the electrochemical stability of layered oxide materials. The graded  $P3-K_{0.7}Mn_{0.7}Mg_{0.3}O_2$  microparticles reported by Weng et al. exhibited high capacities ( $145 \text{ mAh g}^{-1}$  at  $20 \text{ mA g}^{-1}$  and  $58 \text{ mAh g}^{-1}$  at  $400 \text{ mA g}^{-1}$ ).<sup>[138]</sup> A capacity retention of 83% after 400 cycles, and the rate capability of  $58 \text{ mAh g}^{-1}$  can be possessed (Figure 16A,B). Compared with the  $K_{0.7}Mn_{0.7}Mg_{0.3}O_2$  bulk, the enhanced electrochemical performance of the hierarchical  $P3-K_{0.7}Mn_{0.7}Mg_{0.3}O_2$  microparticles originated from their

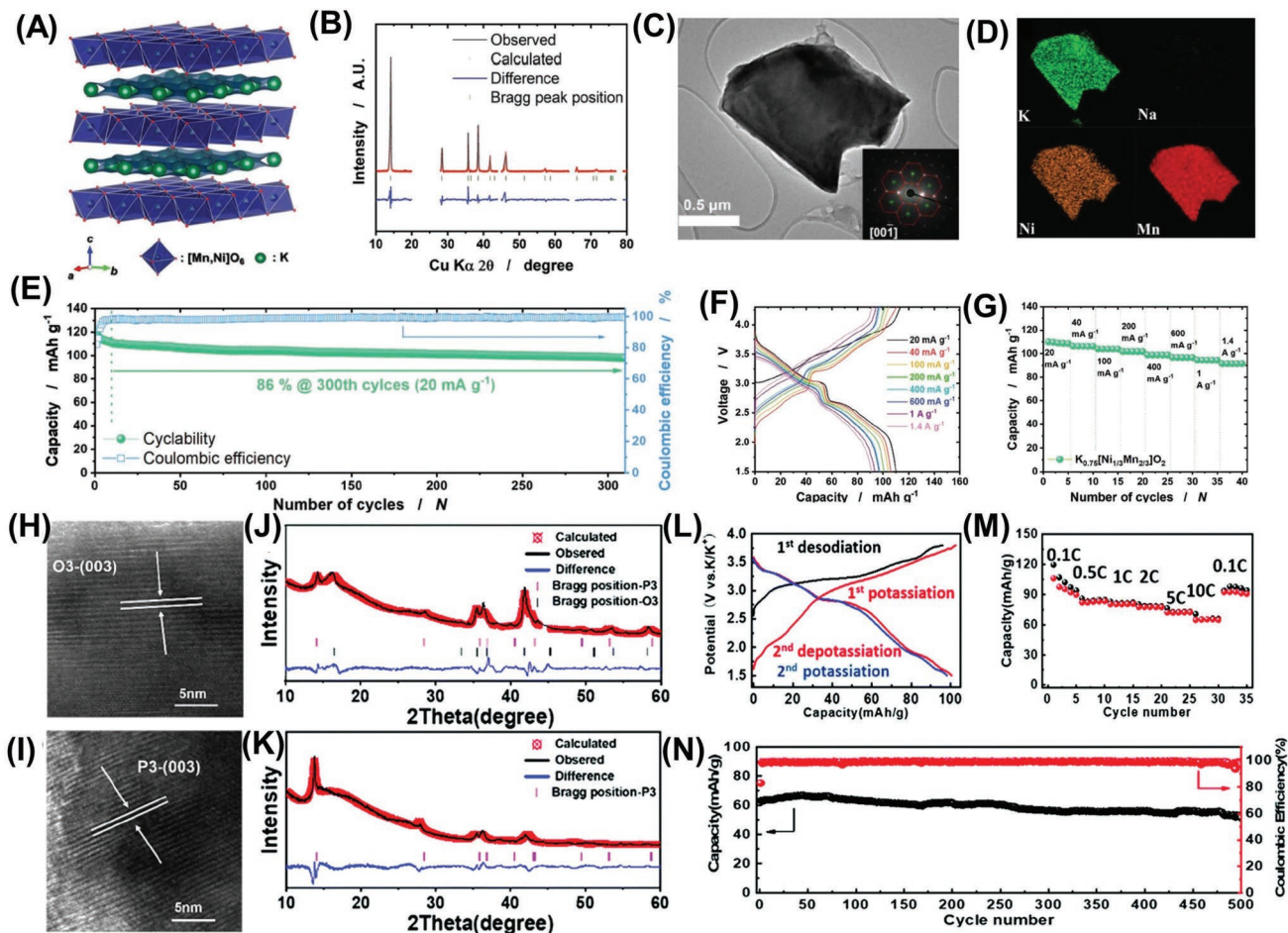


**Figure 14.** A)  $K^+$  sites in  $P2\text{-}K_{0.75}[\text{Ni}_{1/3}\text{Mn}_{2/3}]\text{O}_2$  structure predicted through BVOL analyses. B) Rietveld refinement of XRD data for the  $P2\text{-}K_{0.75}[\text{Ni}_{1/3}\text{Mn}_{2/3}]\text{O}_2$  obtained after the electrochemical ion-exchange. C) TEM image of  $P2\text{-}K_{0.75}[\text{Ni}_{1/3}\text{Mn}_{2/3}]\text{O}_2$  (inset: SAED pattern) and D) the resulting EDS mapping images. E) Long term cyclability of K metal|0.5 M KPF<sub>6</sub> in EC:DEC = 1:1 (v/v) ||  $P2\text{-}K_{0.75}[\text{Ni}_{1/3}\text{Mn}_{2/3}]\text{O}_2$  cell tested at 20 mA g<sup>-1</sup>. F) Charge/discharge curves at various currents from 20 to 1400 mA g<sup>-1</sup> and G) the resulting rate capacities plot. Reproduced with permission.<sup>[131]</sup> Copyright 2019, John Wiley and Sons. H) TEM image of the NCRO cathode belonging to the O3 phase showing an interlayer spacing of 0.625 nm. Ex situ XRD pattern of NCRO after J) 1 cycle and K) 400 cycles. L) Galvanostatic voltage–capacity profiles of NCRO. M) Rate capability of the NCRO. N) Cycling performance of NCRO at 500 mA g<sup>-1</sup>. Reproduced with permission.<sup>[59]</sup> Copyright 2019, The Royal Society of Chemistry.

unique hierarchical structure, which accelerates  $K^+$  transport, reduces the diffusion path and minimizes the occurrence of side reactions. In addition, high Mg doping content (30%) can effectively suppress the irreversible phase transition reaction and lower the migration energy barrier of  $K^+$  (Figure 16C).

In addition to Mg, Ti is also a common inactive doping element in layered oxide materials, which can enhance the cyclic stability and stabilize the crystalline structure of materials. Cao research group introduced Ti element into  $K_{5/9}\text{MnO}_2$  to synthesize  $P2\text{-}K_{5/9}\text{Mn}_{7/9}\text{Ti}_{2/9}\text{O}_2$  layered oxide material. The existence of Ti can effectively resist the transition-metal of P2 type structure in the electrochemical reaction process layer slip, thereby suppressing the destructive phase transitions that typically occur in layered oxides. More importantly, even  $P2\text{-}K_{5/9}\text{Mn}_{7/9}\text{Ti}_{2/9}\text{O}_2$  charged to 4.2 V, only the reversible OP4 mesophase structural evolution from P2 occurs, which ensures the structural integrity of the material during cycling (Figure 16D). In contrast, the

$K_{5/9}\text{MnO}_2$  material without Ti doping will experience a complex phase transformation process from P2 to P'2 to O2, with large structural changes and part irreversible phase transition (Figure 16E). Although the Mg/Mn-Based and Ti/Mn binary-transition-metal oxides have been reported to show good electrochemical property, Mg and Ti are electrochemically inert elements after all, and the introduction of too much into the material will reduce the theoretical capacity. Therefore, these two elements are usually added in small amounts into layered oxides as doping elements to achieve effective regulation of electrochemical performance.

## 5. Multi-Transition-Metal Oxide Cathode

The binary-transition-metal ions can enhance the electrochemical performances of layered oxide materials by the synergistic

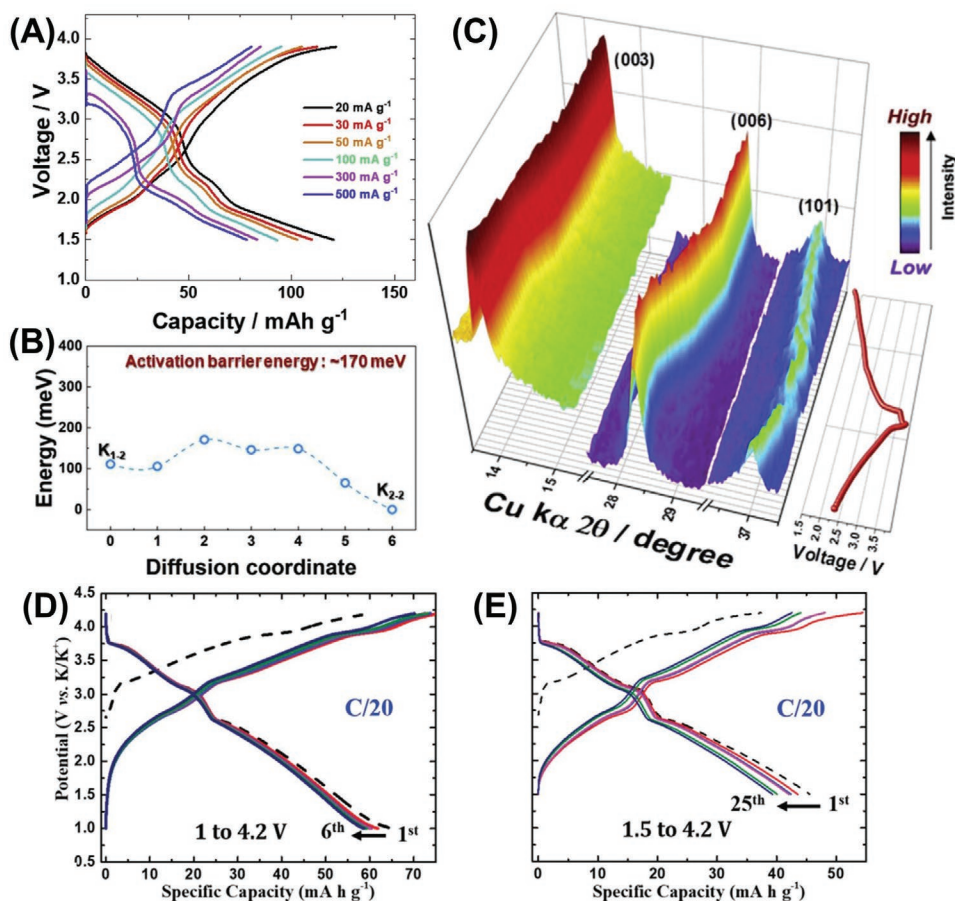


**Figure 15.** A) Rate performance of P3- $\text{K}_{0.54}[\text{Co}_{0.5}\text{Mn}_{0.5}]\text{O}_2$ . B)  $\text{K}^+$  diffusion paths predicted with activation barrier energy on P3- $\text{K}_{0.75}[\text{Co}_{0.5}\text{Mn}_{0.5}]\text{O}_2$ . C) In situ XRD patterns of P3- $\text{K}_{0.54}[\text{Co}_{0.5}\text{Mn}_{0.5}]\text{O}_2$ . Reproduced with permission.<sup>[134]</sup> Copyright 2019, Elsevier. Galvanostatic charge/discharge profiles of P3- $\text{K}_{0.48}\text{Mn}_{0.4}\text{Co}_{0.6}\text{O}_2$  in the potential window range of D) 1.0 to 4.2 V and E) 1.5 to 4.2 V. Reproduced with permission.<sup>[137]</sup> Copyright 2020, The Royal Society of Chemistry.

effect to some extent, and the introduction of more transition-metal ions into them to form multi-metal layered oxides can further exert the improved advantages. This idea is also one of the mainstream research directions of potassium-electric layered oxide materials. The reported multi-transition-metal oxide are mainly ternary materials of various compositions, including Mn/Co/Ni-based, Mn/Ni/Fe-based, and other systems.

### 5.1. Mn/Co/Ni-Based Multi-Transition-Metal Oxide Cathode

Mn/Co/Ni-based multi-transition-metal oxide have been extensively researched in SIBs and LIBs.<sup>[140–143]</sup> Especially in LIBs, NCM (Ni-Co-Mn) cathode materials are the most potential cathode materials. Nevertheless, the research on Mn/Co/Ni-based multi-transition-metal oxide in PIBs is still in its infancy. In 2017, Liu et al. prepared  $\text{K}_{0.67}\text{Ni}_{0.17}\text{Co}_{0.17}\text{Mn}_{0.66}\text{O}_2$  through coprecipitation-assisted solid-phase method for the first time. It delivered an average potential of 3.1 V with a capacity of  $76.5 \text{ mAh g}^{-1}$ .<sup>[144]</sup> The  $\text{K}_{0.67}\text{Ni}_{0.17}\text{Co}_{0.17}\text{Mn}_{0.66}\text{O}_2$  also exhibits good cycling performance at  $20 \text{ mA g}^{-1}$  (87% capacity retention over 100 discharge/charge). Although the electrochemical

performance of the material is not outstanding and requires further improvement, this research work demonstrates the potential of Mn/Co/Ni-based multi-transition-metal oxide as cathodes for PIBs. Subsequently, the researchers mainly achieved the improvement of the electrochemical properties of Mn/Co/Ni-based multi-transition-metal oxide by micro/nano structure construction and ion doping. Deng et al. prepared P3-type  $\text{K}_{0.5}\text{Mn}_{0.72}\text{Ni}_{0.15}\text{Co}_{0.13}\text{O}_2$  microspheres by a solvothermal method as a PIB cathode material (Figure 17A).<sup>[145]</sup> It is a secondary microsphere composed of densely packed submicron primary particles. Due to the short diffusion distance, the layered structure can not only efficiently promote the transport of  $\text{K}^+$ , but also release the stress change induced by the  $\text{K}^+$  continuous insertion/extraction (Figure 17B). Therefore, it exhibited a capacity of  $82.5 \text{ mAh g}^{-1}$  at  $10 \text{ mA g}^{-1}$ , an excellent rate performance at  $500 \text{ mA g}^{-1}$ , and an outstanding cycling stability over 300 discharge/charge (Figure 17D). Moreover, the microspheres can improve the compaction density of the electrode. Based on the cathode volume, its volume energy density can reach  $121.1 \text{ Wh L}^{-1}$  (Figure 17C). In addition, Dang et al. doped  $\text{Mg}^{2+}$  and  $\text{Al}^{3+}$  into P3-type  $\text{K}_{0.45}\text{Ni}_{0.1}\text{Co}_{0.1}\text{Mn}_{0.8}\text{O}_2$ , respectively, to prepare  $\text{K}_{0.45}\text{Ni}_{0.1}\text{Co}_{0.1}\text{Mg}_{0.05}\text{Mn}_{0.75}\text{O}_2$  and

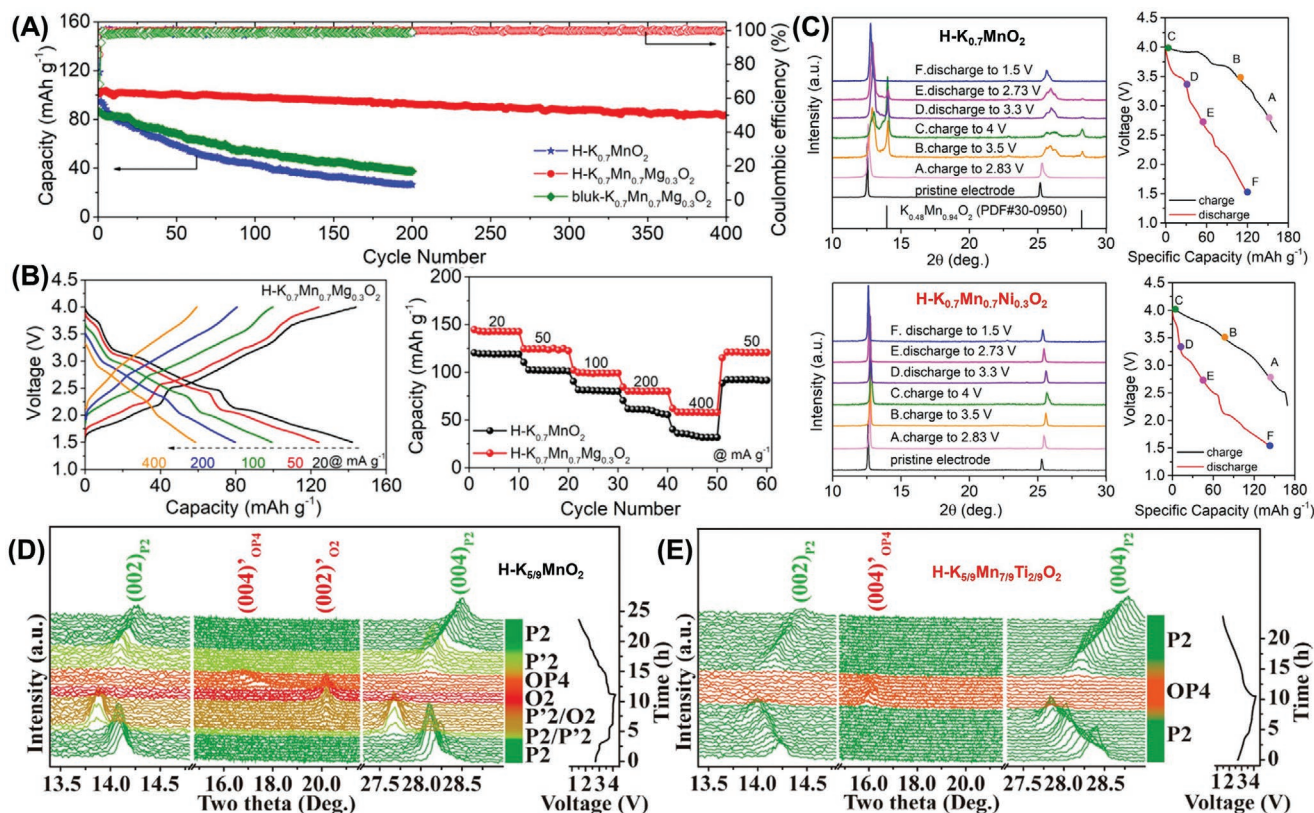


**Figure 16.** A) Long-term cycling performance of  $\text{H-K}_{0.7}\text{MnO}_2$ ,  $\text{H-K}_{0.7}\text{Mn}_{0.7}\text{Mg}_{0.3}\text{O}_2$ , and  $\text{bulk-K}_{0.7}\text{Mn}_{0.7}\text{Mg}_{0.3}\text{O}_2$ . B) Charge/discharge profiles of  $\text{H-K}_{0.7}\text{Mn}_{0.7}\text{Mg}_{0.3}\text{O}_2$  at selected cycles (left) and rate performance of  $\text{H-K}_{0.7}\text{MnO}_2$  and  $\text{H-K}_{0.7}\text{Mn}_{0.7}\text{Mg}_{0.3}\text{O}_2$  (right). C) Ex situ XRD patterns collected at different electrochemical states of  $\text{H-K}_{0.7}\text{MnO}_2$  (top) and  $\text{H-K}_{0.7}\text{Mn}_{0.7}\text{Mg}_{0.3}\text{O}_2$  (bottom). Reproduced with permission.<sup>[138]</sup> Copyright 2020, Elsevier. In situ XRD patterns of D) P2-type P2- $\text{K}_{5/9}\text{MnO}_2$  and E) P2- $\text{K}_{5/9}\text{Mn}_{7/9}\text{Ti}_{2/9}\text{O}_2$ , respectively. Reproduced with permission.<sup>[139]</sup> Copyright 2020, Elsevier.

$\text{K}_{0.45}\text{Ni}_{0.1}\text{Co}_{0.1}\text{Ag}_{0.05}\text{Mn}_{0.75}\text{O}_2$  material.<sup>[146]</sup> The Al-doped material shows the best electrochemical property, with a capacity retention of 77.1% over 100 discharge/charge, and still has a high capacity of  $137 \text{ mAh g}^{-1}$  at  $500 \text{ mA g}^{-1}$  (Figure 17E,F). In addition, the authors discovered the charge compensation of the  $\text{Co}^{3+}/\text{Co}^{4+}$ ,  $\text{Ni}^{2+}/\text{Ni}^{3+}$ , and  $\text{Mn}^{3+}/\text{Mn}^{4+}$  redox pairs through ex situ XPS analysis (Figure 17G). Recently, Zhou research group successfully prepared uniform P3- $\text{K}_{0.5}\text{Mn}_{0.8}\text{Co}_{0.1}\text{Ni}_{0.1}\text{O}_2$  porous microcubes via an ethanol-mediated coprecipitation method.<sup>[147]</sup> Such unique porous microcube structure greatly shortens the  $\text{K}^+$  diffusion distance and alleviates the internal strain caused by continuous insertion/extraction of  $\text{K}^+$ , resulting in improved reaction kinetics and structural integrity, and ultimately improved electrochemical performance (Figure 17H).  $\text{K}_{0.5}\text{Mn}_{0.8}\text{Co}_{0.1}\text{Ni}_{0.1}\text{O}_2$  porous microcubes exhibit a high capacity of  $94.5 \text{ mAh g}^{-1}$  at  $20 \text{ mA g}^{-1}$  and an outstanding rate capability at  $500 \text{ mA g}^{-1}$ , as well as, the remarkable cycling stability (Figure 17I,J).

## 5.2. Mn/Ni/Fe-Based Multi-Transition-Metal Oxide Cathode

In order to reduce the cost of electrodes mainly from the expensive Ni and Co, cheap Fe was added in the multi-transition-metal system. Sun et al. reported a  $\text{K}_{0.5}\text{Mn}_{0.8}\text{Fe}_{0.1}\text{Ni}_{0.1}\text{O}_2$

layered cathode by partially replacing Mn with Fe and Ni.<sup>[148]</sup> The  $\text{Ni}^{2+/3+}$ ,  $\text{Mn}^{3+/4+}$ , and  $\text{Fe}^{3+/4+}$  redox pairs provide charge compensation within 1.5–3.9 V, so that  $\text{K}_{0.5}\text{Mn}_{0.8}\text{Fe}_{0.1}\text{Ni}_{0.1}\text{O}_2$  shows high voltage and high capacity, fast  $\text{K}^+$  migration rate and low  $\text{K}^+$  diffusion barrier. The sharing of O atoms in  $\text{FeO}_6$ ,  $\text{NiO}_6$ , and  $\text{MnO}_6$  ( $\text{O-Fe-O-Ni-O-Mn-O}$ ) can prevent the generation of structural defects such as the Jahn–Teller effect in the  $\text{MnO}_6$  octahedron. In situ synchrotron XRD measurements observed that  $\text{K}_{0.5}\text{Mn}_{0.8}\text{Fe}_{0.1}\text{Ni}_{0.1}\text{O}_2$  undergoes a reversible phase transformation ( $\text{P3} \rightarrow \text{O3}$  upon  $\text{K}^+$  extraction,  $\text{O3} \rightarrow \text{P3} \rightarrow \text{P'3}$  upon  $\text{K}^+$  insertion) during cycling with minimal structural changes (Figure 18A–D). Because of the outstanding structural stability, a reversible capacity of  $120 \text{ mAh g}^{-1}$  at  $50 \text{ mA g}^{-1}$  and a capacity retention of 74% over 300 charge/discharge were exhibited (Figure 18E). In particular, a discharge capacity of  $76 \text{ mAh g}^{-1}$  is maintained at high rate of  $2.5 \text{ A g}^{-1}$  (Figure 18F). Then, Sun et al. synthesized a high potassium content materials with the same combination of Fe, Ni, and Mn by ion exchange method, namely P2- $\text{K}_{0.75}[\text{Mn}_{0.8}\text{Ni}_{0.1}\text{Fe}_{0.1}\text{O}_2]$  (Figure 18G).<sup>[149]</sup> Upon the charged and discharged, it can release and store 0.5 mol of  $\text{K}^+$  in 1.5–3.9 V without phase transition (Figure 18H). Due to the highly stable layered framework, it provides a high capacity of  $110 \text{ mAh g}^{-1}$  at  $10 \text{ mA g}^{-1}$  and a cycle retention of 70% in 200 charge/discharge (Figure 18I–K).

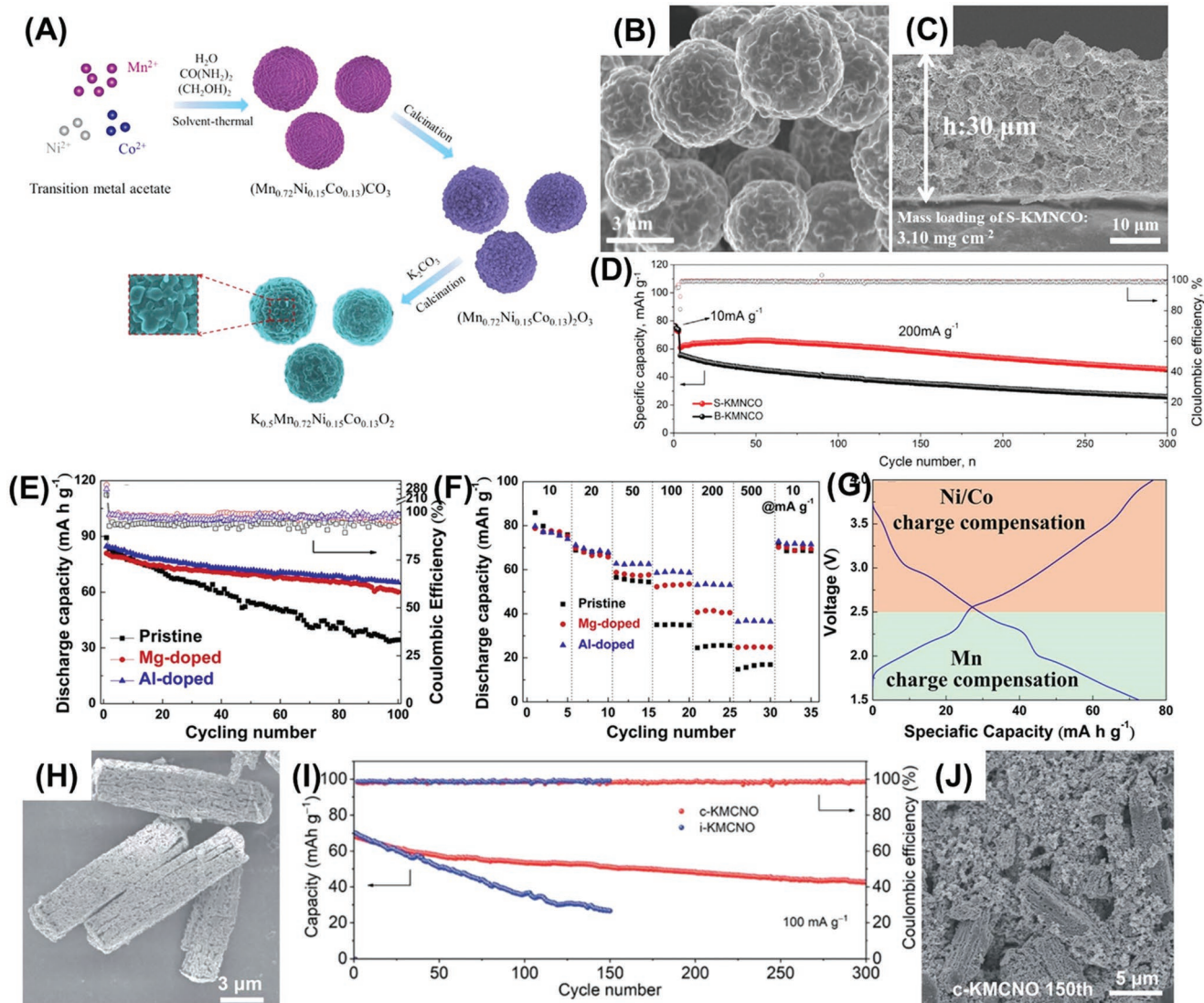


**Figure 17.** A) Schematic illustration of the synthetic route of P3- $K_{0.5}Mn_{0.72}Ni_{0.15}Co_{0.13}O_2$  microsphere. B) SEM image of P3- $K_{0.5}Mn_{0.72}Ni_{0.15}Co_{0.13}O_2$  microsphere. C) Cross sectional SEM image of  $K_{0.5}Mn_{0.72}Ni_{0.15}Co_{0.13}O_2$  electrode. D) Cycling performance of P3- $K_{0.5}Mn_{0.72}Ni_{0.15}Co_{0.13}O_2$  at  $200\text{ mA g}^{-1}$ . Reproduced with permission.<sup>[145]</sup> Copyright 2020, Elsevier. E) Cycling performance at  $20\text{ mA g}^{-1}$  and F) rate performance of the pristine, Mg-doped, and Al-doped P3- $K_{0.45}Ni_{0.1}Co_{0.1}Mn_{0.8}O_2$ . G) Different elements' charge compensation contribution for capacity during different voltage range for P3- $K_{0.45}Ni_{0.1}Co_{0.1}Mn_{0.8}O_2$ . Reproduced with permission.<sup>[146]</sup> Copyright 2020, Elsevier. H) SEM image of P3- $K_{0.5}Mn_{0.8}Co_{0.1}Ni_{0.1}O_2$  porous microcuboids. I) Long-term cycling performance of P3- $K_{0.45}Ni_{0.1}Co_{0.1}Mn_{0.8}O_2$  at  $100\text{ mA g}^{-1}$ . J) SEM image of P3- $K_{0.5}Mn_{0.8}Co_{0.1}Ni_{0.1}O_2$  porous microcuboid electrode after 150 cycles. Reproduced with permission.<sup>[147]</sup> Copyright 2021, The Royal Society of Chemistry.

### 5.3. Other Multi-Transition-Metal Oxide Cathode

In addition to Mn/Co/Ni-based and Mn/Ni/Fe-based multi-transition-metal oxides, there are some multi-transition-metal oxides of other components; but due to the wide classification of components, and only a few materials of each component are reported. Therefore, the multi-transition-metal oxides of these components are unified and introduced in this section. Recently, the Shi research group reported two similar multi-transition-metal oxides: P3-type  $K_{0.45}Co_{1/12}Mg_{1/12}Mn_{5/6}O_2$ <sup>[153]</sup> and  $K_{1/2}Mn_{5/6}Mg_{1/12}Ni_{1/12}O_2$ .<sup>[154]</sup> Among them, for Co-Mg co-doped  $K_{0.45}Co_{1/12}Mg_{1/12}Mn_{5/6}O_2$ , the  $Co^{3+}Mg^{2+}$  occupying  $Mn^{3+}$  sites can effectively alleviate the Jahn–Teller effect of  $Mn^{3+}$ . The  $Co^{3+}$  can also participate in

electrochemical reactions and contribute additional capacity; inactive  $Mg^{2+}$  can act to generate a smooth charge/discharge process and stabilize the layered structure. Experiments demonstrate that  $K_{0.45}Co_{1/12}Mg_{1/12}Mn_{5/6}O_2$  exhibits highly reversible structural evolution, excellent structural stability, and fast  $K^+$  diffusion during cycling (Figure 19B). Therefore,  $K_{0.45}Co_{1/12}Mg_{1/12}Mn_{5/6}O_2$  exhibits better electrochemical performance owing to the synergistic effect of Mg-Co co-doping. In another P3- $K_{1/2}Mn_{5/6}Mg_{1/12}Ni_{1/12}O_2$  material, part of  $Ni^{2+}$  and  $Mg^{2+}$  occupy the  $K^+$  layer, acting as “pillar” and inhibiting the sliding of the oxide layer during  $K^+$  extraction/insertion. The “Ni-Mg pillar effect” not only relieves the volume change of the material, but also suppresses the phase transition, thereby improving the cycling performance (Figure 19A).

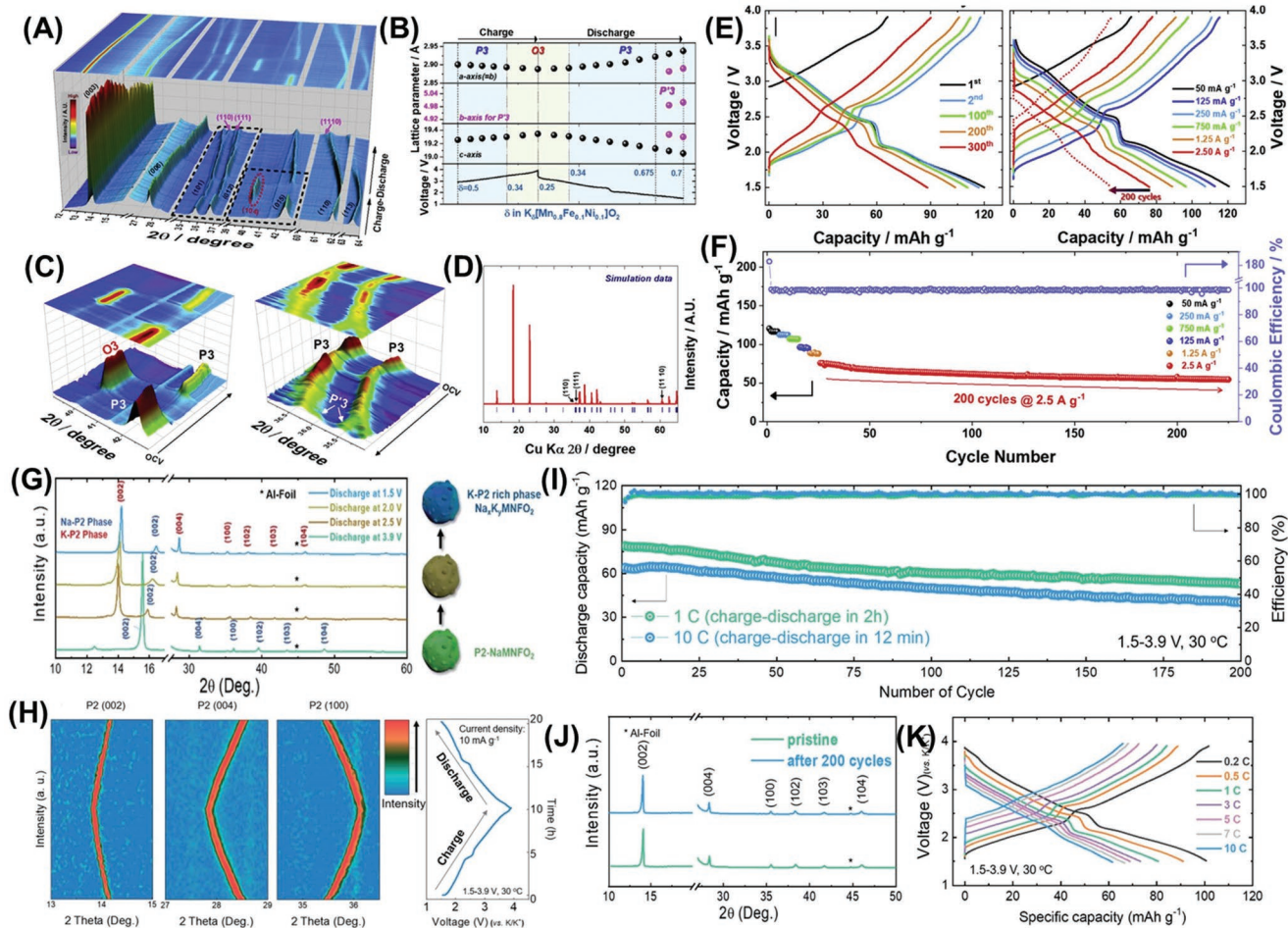


**Figure 18.** A) Operando SXR D pattern for the P3- $K_{0.5}[Mn_{0.8}Fe_{0.1}Ni_{0.1}]O_2$  electrode. B) The lattice parameters from  $K_{0.25}[Mn_{0.8}Fe_{0.1}Ni_{0.1}]O_2$  to  $K_{0.7}[Mn_{0.8}Fe_{0.1}Ni_{0.1}]O_2$  during the charge–discharge processes. C) Magnified operando SXR D patterns. D) XRD pattern of the P'3- $K_{0.7}[Mn_{0.8}Fe_{0.1}Ni_{0.1}]O_2$  in a simulated environment. E) Charge–discharge profiles at  $50\text{ mA g}^{-1}$  and charge–discharge profiles at various current rates of  $K_{0.5}[Mn_{0.8}Fe_{0.1}Ni_{0.1}]O_2$ . F) The rate capability of the P3- $K_{0.5}[Mn_{0.8}Fe_{0.1}Ni_{0.1}]O_2$  electrode in different states of charge. Reproduced with permission.<sup>[148]</sup> Copyright 2020, Elsevier. G) Ex situ XRD patterns of the  $Na_x[Mn_{0.8}Ni_{0.1}Fe_{0.1}]O_2$  electrode in different states of charge. H) In operando XRD patterns of P2- $K_{0.75}[Mn_{0.8}Ni_{0.1}Fe_{0.1}]O_2$  during the charge and discharge process. I) Cycle life test of the P2- $K_{0.75}[Mn_{0.8}Ni_{0.1}Fe_{0.1}]O_2$  cathode at rates of 10 and  $100\text{ mA g}^{-1}$ . J) Ex situ XRD patterns during the pristine  $K_{0.75}[Mn_{0.8}Ni_{0.1}Fe_{0.1}]O_2$  electrode and the electrode after 200 cycles at  $100\text{ mA g}^{-1}$ . K) Rate capability of the  $K_{0.75}[Mn_{0.8}Ni_{0.1}Fe_{0.1}]O_2$  cathode. Reproduced with permission.<sup>[149]</sup> Copyright 2019, The Royal Society of Chemistry.

In addition, the increased interlayer spacing after Ni-Mg codoping not only reduces the  $K^+$  migration energy barrier, but also contributes to the pseudocapacitive properties. Therefore, P3- $K_{1/2}Mn_{5/6}Mg_{1/12}Ni_{1/12}O_2$  also possesses the excellent electrochemical performance. Besides these two materials, Zhang et al. designed a zero-strain and low-cost cathode, named P3- $K_{0.4}Fe_{0.1}Mn_{0.8}Ti_{0.1}O_2$ .<sup>[152]</sup> This material exhibits a reversible capacity of  $117\text{ mAh g}^{-1}$  at  $20\text{ mA g}^{-1}$  and a rapid rate ability at  $1000\text{ mA g}^{-1}$ . In situ XRD results revealed the single-phase solid solution transformation mechanism of  $K_{0.4}Fe_{0.1}Mn_{0.8}Ti_{0.1}O_2$  with negligible volume change (0.5%) during  $K^+$  insertion/extraction, ensuring long-cycle stability for 300 cycles (Figure 19C). Xu et al. reported a P2-type layered material with the molecular formula  $K_{0.6}Mn_{0.8}Ni_{0.1}Ti_{0.1}O_2$ , exhibiting a reversible  $K^+$  insertion/extraction capability of  $4.2\text{ V}$ .<sup>[153]</sup> The co-doping of Ti and Ni can not only restrain the structural detrimental induced by the  $Mn^{3+}$  Jahn-Teller effect, but also suppress the damage lattice sliding of the transition metal

layer at high potential. Therefore, it shows a favorable single-phase solid solution reaction, successfully suppressing the destructive phase transition in the deeply de-potassium state (Figure 19D).

## 6. Advanced Characterization Techniques

Based on the aforementioned understanding and perspectives of layered transition-metal oxide cathodes, in-depth fundamental research and further improvement of optimization are crucial to the next-generation advanced PIBs. The following section focuses on the advanced characterization techniques applied to research the layered transition-metal oxide electrode materials, including high-resolution fine structure analysis, real-time spectroscopy monitoring, and theoretical simulation calculations.

High-resolution fine structure analysis is key to understanding and developing electrode materials for energy storage

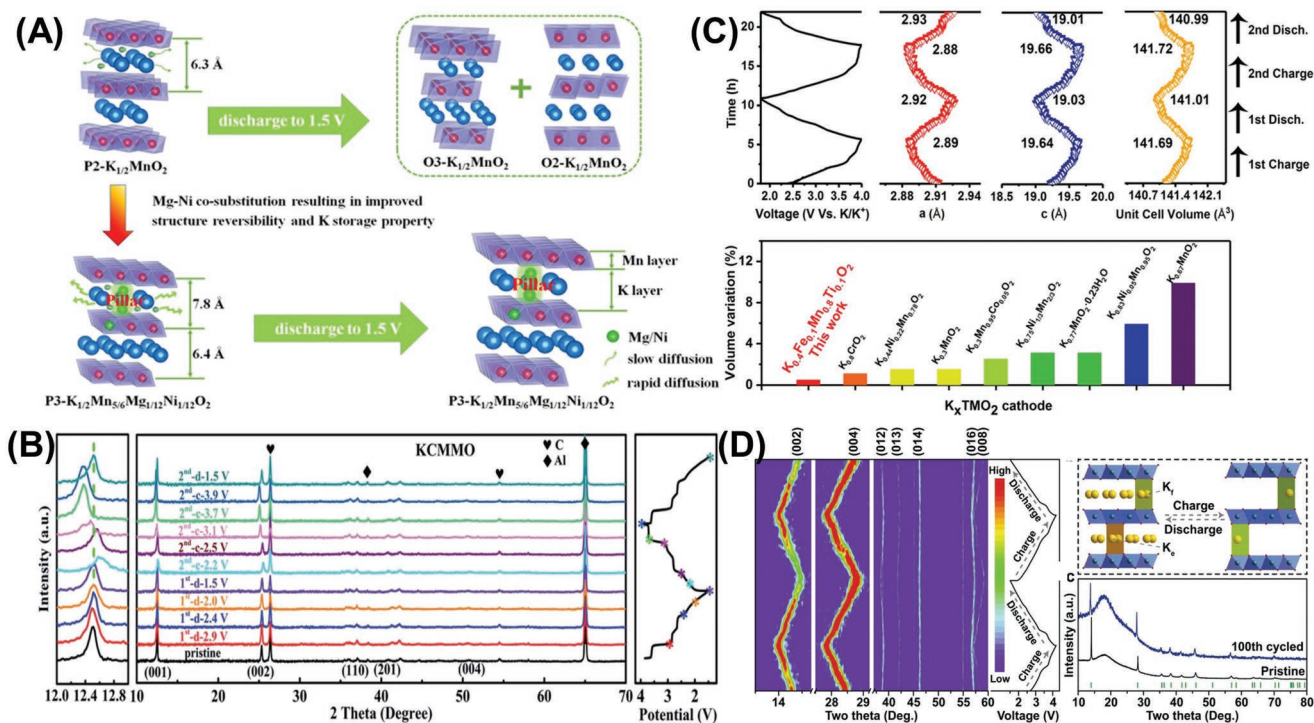


**Figure 19.** A) Schematic of the phase transition suppression in P3-K<sub>1/2</sub>Mn<sub>5/6</sub>Mg<sub>1/12</sub>Ni<sub>1/12</sub>O<sub>2</sub> compared with pristine K<sub>1/2</sub>MnO<sub>2</sub>. Reproduced with permission.<sup>[151]</sup> Copyright 2021, American Chemical Society. B) Ex situ XRD patterns of K<sub>0.45</sub>Co<sub>1/12</sub>Mg<sub>1/12</sub>Mn<sub>5/6</sub>O<sub>2</sub> electrode. Reproduced with permission.<sup>[150]</sup> Copyright 2021, The Royal Society of Chemistry. C) Variation of lattice constants for K<sub>0.4</sub>Fe<sub>0.1</sub>Mn<sub>0.8</sub>Ti<sub>0.1</sub>O<sub>2</sub> along with K<sup>+</sup> insertion and extraction and the comparison of unit-cell volume variation of previously reported K<sub>x</sub>TMO<sub>2</sub> electrode materials. Reproduced with permission.<sup>[152]</sup> Copyright 2021, American Chemical Society. D) In situ XRD pattern of the K<sub>0.6</sub>Mn<sub>0.8</sub>Ni<sub>0.1</sub>Ti<sub>0.1</sub>O<sub>2</sub>. Reproduced with permission.<sup>[153]</sup> Copyright 2021, Elsevier.

devices. Currently, spherical aberration-corrected scanning TEM (STEM) has been widely used as a powerful tool for studying the crystal structure information of electrode materials at the atomic scale.<sup>[10,126,154]</sup> Zhang et al. observed fine structure of P2-K<sub>0.44</sub>Ni<sub>0.22</sub>Mn<sub>0.78</sub>O<sub>2</sub> at atomic resolution by high-angle annular dark field STEM (HAADF-STEM) techniques.<sup>[135]</sup> The bright dots in the HAADF-STEM images are TM ions and the space between two adjacent transition metal atoms is 0.29 nm, which correspond with the cell parameter  $\alpha$  (Figure 20A). Enlarged HAADF-STEM image, the darker black dots are K<sup>+</sup> ions located in the 2d Wyckoff site (Ke) in the layered structure, while other ions with 2b Wyckoff sites (Kf) are in the same column as the TM atoms (Figure 20B). Moreover, hexagonal symmetric arrangement of one TM atom surrounded by six TM atoms agrees with the hcp crystal model in the ab plane (Figure 20C). Lin et al. obtained the position of the Mn slabs and K slabs in K<sub>0.77</sub>MnO<sub>2</sub>·0.23H<sub>2</sub>O under HR-STEM (Figure 20D).<sup>[10]</sup> It can be seen that the as-prepared K<sub>0.77</sub>MnO<sub>2</sub>·0.23H<sub>2</sub>O presents a larger interlayer distance (6.8 Å) compared to the reported P3-K<sub>0.5</sub>MnO<sub>2</sub> (6.3 Å).

In recent years, many advanced real-time spectroscopic monitoring techniques have been exploited and applied to detect the structural evolution of electrodes during charge/discharge processes, such as in situ XPS, in situ XRD, and in situ Raman.<sup>[155–160]</sup> These advanced in situ techniques are also gradually used in the research of layered transition-metal oxide cathodes for PIBs.<sup>[51,76,126,131]</sup> In order to research the phase transitions of K<sub>0.7</sub>Fe<sub>0.5</sub>Mn<sub>0.5</sub>O<sub>2</sub> nanowires in PIBs, the advanced in situ XRD

measurement are employed (Figure 20E).<sup>[51]</sup> Based on in situ XRD analysis, Wang et al. confirmed that K<sub>0.7</sub>Fe<sub>0.5</sub>Mn<sub>0.5</sub>O<sub>2</sub> could demonstrate a robust layered skeleton structure upon K<sup>+</sup> de-intercalation/intercalation. In situ XRD measurements are carried out by Jo et al. to investigate the structural transition of the P2-K<sub>0.75</sub>[Ni<sub>1/3</sub>Mn<sub>2/3</sub>]O<sub>2</sub>.<sup>[131]</sup> Upon de-potassiation to 4.3 V, the (100), (102), (103), and (104) peaks of K<sub>0.75</sub>[Ni<sub>1/3</sub>Mn<sub>2/3</sub>]O<sub>2</sub> move to higher angles, while the (004) and (002) peaks gradually shift to lower angle. During potassiation to 1.5 V, the main peaks reversibly shift to the original positions (Figure 20F). These results demonstrate that the K<sub>0.75</sub>[Ni<sub>1/3</sub>Mn<sub>2/3</sub>]O<sub>2</sub> experiences the single-phase reaction, in which the corresponding electrochemical activity is fitted with the Ni<sup>4+/2+</sup> redox pair. Zhang et al. adopted in situ XRD technology to detect the evolution of P2-K<sub>0.44</sub>Ni<sub>0.22</sub>Mn<sub>0.78</sub>O<sub>2</sub> cathode during the K<sup>+</sup> insertion/extraction.<sup>[126]</sup> Obviously, in the reversible charging and discharging process, the phase of P2-K<sub>0.44</sub>Ni<sub>0.22</sub>Mn<sub>0.78</sub>O<sub>2</sub> does not change, which indicates a solid-solution processes (Figure 20G). Combining the detailed variation of lattice parameters, the authors demonstrated that sustainable complete single-phase transition and structure evolution during K<sup>+</sup> extraction and insertion with only 1.5% volume variation calculated. Ceder group revealed the K-storage mechanism of P3-K<sub>0.5</sub>MnO<sub>2</sub> using in situ XRD technology.<sup>[76]</sup> A two-phase reaction when 0.316 < x < 0.364 and 0.395 < x < 0.425 in K<sub>x</sub>MnO<sub>2</sub>, as well as solid solution states at different K compositions was investigated. The (006) and (003) peaks move to lower angles during charging process, which implies the expansion of the MnO<sub>2</sub> layer (Figure 20H). More

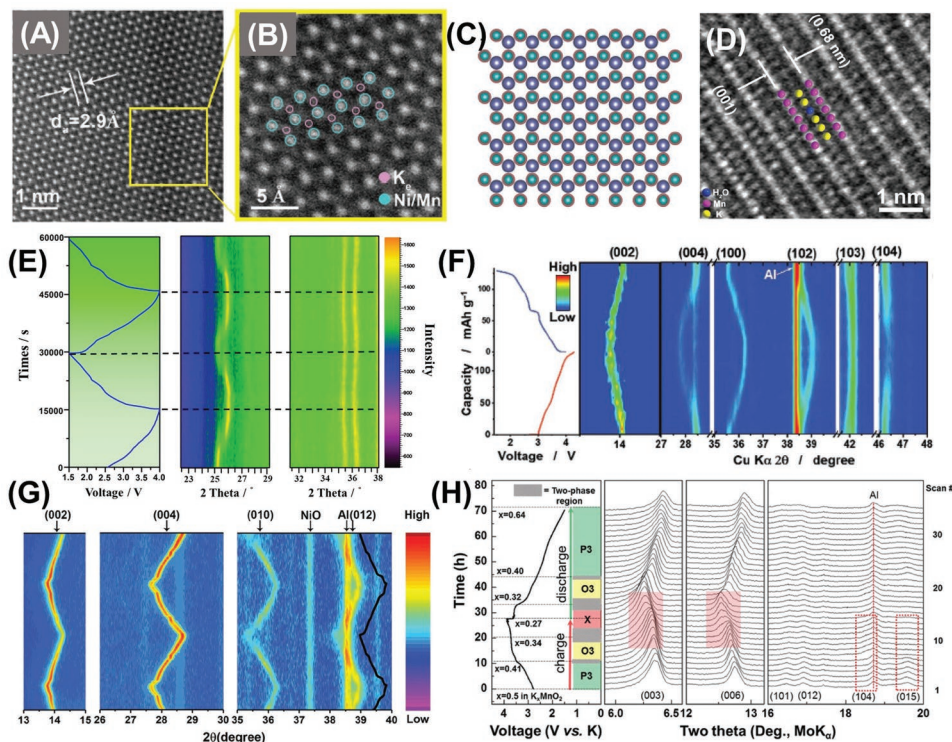


**Figure 20.** A) HAADF-STEM image of  $K_{0.44}Ni_{0.22}Mn_{0.78}O_2$  along the [001] zone axis. B) A closer look at the area highlighted in a) and the location of Ni/Mn and Ke atoms are designated. C) Schematic illustration of  $K_{0.44}Ni_{0.22}Mn_{0.78}O_2$  crystal along the [001] projection. Reproduced with permission.<sup>[126]</sup> Copyright 2019, John Wiley and Sons. D) Enlarged HRTEM image of  $K_{0.77}MnO_2 \cdot 0.23H_2O$ . Reproduced with permission.<sup>[10]</sup> Copyright 2017, John Wiley and Sons. E) In situ XRD patterns of interconnected  $K_{0.7}Fe_{0.5}Mn_{0.5}O_2$  nanowires during galvanostatic de-potassiation/potassiation at 100 mA  $g^{-1}$ . Reproduced with permission.<sup>[51]</sup> Copyright 2019, American Chemical Society. F) Operando-XRD result of P2- $K_{0.75}[Ni_{1/3}Mn_{2/3}]O_2$  electrode. Reproduced with permission.<sup>[13]</sup> Copyright 2019, John Wiley and Sons. G) 2D plot of in situ XRD patterns of  $K_{0.44}Ni_{0.22}Mn_{0.78}O_2$  electrode collected during the first and second charge/discharge at 10 mA  $g^{-1}$  in the voltage range of 1.5–4.0 V. Reproduced with permission.<sup>[126]</sup> Copyright 2019, John Wiley and Sons. H) In situ XRD pattern taken for 2 h scanning rate per pattern of P3- $K_{0.5}MnO_2$ . Reproduced with permission.<sup>[76]</sup> Copyright 2017, John Wiley and Sons.

importantly, a new (104) peak appears and the (015) peak disappears at  $x \approx 0.41$  in  $K_xMnO_2$ , which suggests a P3 to O3 phase transformation. With the development of real-time spectroscopy monitoring techniques, some new energy storage mechanisms and general phenomena are efficiently studied, which are good for demonstrating the intrinsic relationship of structure-property.

Theoretical simulation calculations also play important role in predicting and characterizing the structures and properties of electrodes at the atomic scale.<sup>[161]</sup> Choi et al. used first-principles calculation with the nudged elastic band (NEB) to reveal the intrinsic reasons of P3- $K_{0.75}[Co_{0.5}Mn_{0.5}]O_2$  exhibiting good rate performance.<sup>[134]</sup> A diffusion barrier energy of  $\approx 260$  meV is needed in P3- $K_{0.75}[Co_{0.5}Mn_{0.5}]O_2$  despite the large  $K^+$  (Figure 21A,B). Furthermore, only an extremely low diffusion barrier energy of  $\approx 170$  meV is needed for partial  $K^+$  ion by changing the binding of Co and Mn at transition metal sites (Figure 21C,D). Therefore, the superior rate performance of P3- $K_{0.75}[Co_{0.5}Mn_{0.5}]O_2$  was clearly presented. Further study on the mechanism of excellent electrochemical performance of bilayered  $\delta$ - $K_{0.51}V_2O_5$  nanobelts, the various trajectories K-diffusion barriers for  $\delta$ - $V_2O_5$  were researched by means of the climbing image NEB (CI-NEB) approach by Zhu et al.<sup>[71]</sup> There are three possible paths for  $\delta$ - $V_2O_5$ , two paths 1 and 2 in the middle layer of the (001) lattice plane and one path 3 along the [001] direction (Figure 21E,G). When  $K^+$  ions diffuse through Path 1, the diffusion direction is

the [010] direction (1/2/3/4), and the results show that K atoms diffuse from different points with the same 0.89 eV energy barrier (Figure 21F). For path 2, K atoms first diffused from site 1 to site 2 with 0.85 eV energy barrier (Figure 21H). Notably,  $\delta$ - $K_{0.51}V_2O_5$  nanobelts grew along the [010] direction (Figure 21I). Assuming that each nanoribbon has an average width of  $D$  and an average length of  $L$ ,  $K^+$  ions exhibit an average diffusion distance of  $0.5L$  as they diffuse in Path 1 along the [001] direction. On the contrary, the average diffusion distance is  $0.53D$  when  $K^+$  ions diffuse along path 2 (Figure 21J,K). Path 2 has a larger diffusion coefficient ( $D$ ) than Path 1 due to the smaller diffusion barrier, so Path 1 takes 10000 times longer to diffuse than Path 2. The results suggest that diffusion along path 2 is the primary cause of the ultrahigh rate capability of  $\delta$ - $K_{0.51}V_2O_5$ . Choi et al. demonstrated the reaction mechanism and theoretical properties of P3- $K_x[Mn_{0.8}Fe_{0.1}Ni_{0.1}]O_2$  upon  $K^+$  insertion/extraction by using the first principles calculation.<sup>[148]</sup> Moreover, the excellent rate performance of P3-/O3- $K_x[Mn_{0.8}Fe_{0.1}Ni_{0.1}]O_2$  was revealed via the first principles calculation with the NEB approach. The diffusion path of  $K^+$  in P3- $K_{0.75}[Mn_{0.8}Fe_{0.1}Ni_{0.1}]O_2$  is along the  $ab$  plane, and  $K^+$  diffusion within this structure is predicted to require an energy barrier of  $\approx 438$  meV (Figure 21L,M). In addition, the  $K^+$  diffusion energy barrier in the O3- $K_{0.25}[Mn_{0.8}Fe_{0.1}Ni_{0.1}]O_2$  drops to  $\approx 409$  meV after P3 to O3 transition (Figure 21N,O). Jo et al. synthesize some  $K^+$ /vacancy

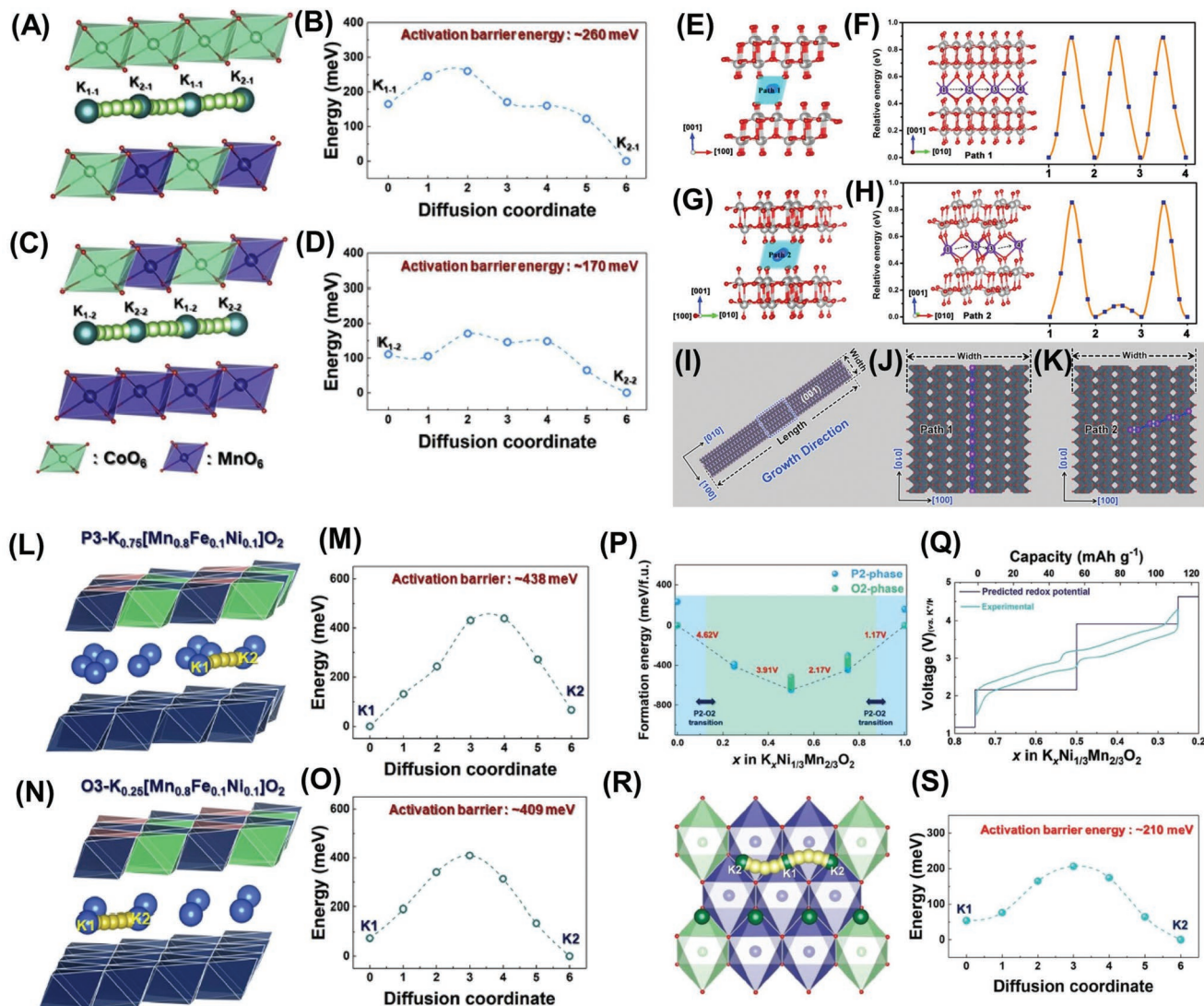


**Figure 21.** A,B) K1-1-K2-1 and C,D) K1-2-K2-2 diffusion paths predicted with activation barrier energy on P3-K<sub>0.75</sub>[Co<sub>0.5</sub>Mn<sub>0.5</sub>]O<sub>2</sub>. Reproduced with permission.<sup>[134]</sup> Copyright 2019, Elsevier. E–H) K-ion diffusion pathways and the corresponding migration activation energy through the interlayer of the (001) lattice plane of  $\delta$ -V<sub>2</sub>O<sub>5</sub>. I) Structure of the as-prepared bilayered  $\delta$ -K<sub>0.51</sub>V<sub>2</sub>O<sub>5</sub> nanobelts. Schematic diagram of the diffusion of K<sup>+</sup> ions through J) path 1 and K) path 2 in the selected area of (I). Reproduced with permission.<sup>[77]</sup> Copyright 2019, Elsevier. K<sup>+</sup> diffusion pathways and activation barriers of L,M) P3-K<sub>0.75</sub>[Mn<sub>0.8</sub>Fe<sub>0.1</sub>Ni<sub>0.1</sub>]O<sub>2</sub> and N,O) O3-K<sub>0.25</sub>[Mn<sub>0.8</sub>Fe<sub>0.1</sub>Ni<sub>0.1</sub>]O<sub>2</sub> obtained using NEB calculations. Reproduced with permission.<sup>[148]</sup> Copyright 2020, Elsevier. P) Formation energies and redox potentials predicted from first-principles calculations. Q) Comparison between experimentally measured charge/discharge curves and redox potentials predicted from first-principles calculations. R) Predicted K<sup>+</sup> diffusion motion in P2-K<sub>x</sub>[Ni<sub>1/3</sub>Mn<sub>2/3</sub>]O<sub>2</sub> structure, and S) activation barrier energy for K<sup>+</sup> diffusion between K1 and K2 sites predicted using NEB method. Reproduced with permission.<sup>[131]</sup> Copyright 2019, John Wiley and Sons.

configurations on various P2/O2-K<sub>x</sub>[Ni<sub>1/3</sub>Mn<sub>2/3</sub>]O<sub>2</sub> ( $0 \leq x \leq 1$ ) through cluster-assisted statistical mechanics software and then arranged and calculated their formation energies (Figure 21P). The predicted redox potential from first-principles calculations of P2-K<sub>x</sub>[Ni<sub>1/3</sub>Mn<sub>2/3</sub>]O<sub>2</sub>, corresponding to the experimentally measured electrochemical curves (Figure 21Q). The activation barrier energy required is only  $\sim 210$  meV, which is effectively to ensure K<sup>+</sup> facile migration in the K<sub>0.75</sub>[Ni<sub>1/3</sub>Mn<sub>2/3</sub>]O<sub>2</sub>. From this consideration, it is believed that the small Stokes radius and the weak Lewis acidity of K can provide fast ionic conductivity and thus high capacity even at high rates.

## 7. Conclusions and Outlook

PIBs have attracted considerable interest due to their notable general merits, including better ionic mobility, high-cell voltages, the use of aluminum as both the anode and cathode substrate, abundant potassium resources, and low cost. Recently, many layered-transition-metal oxide cathodes have been developed with reasonable electrochemical performance, such as single-transition-metal oxide, binary-transition-metal oxide, and multi-transition-metal oxide. Meanwhile, a table, including chemical formula, preparation method, test voltage

window, average output voltage, electrochemical performance, and optimization strategy of layered transition-metal oxide cathodes, has been listed to show the current research status (Table 1). While these pioneering works have been devoted to

develop advanced PIBs, significant progress is still required to achieve the required specifications of technological and practical applications. This article outlines several possible directions for layered transition-metal oxide cathodes in

**Table 1.** A summary of current layered transition-metal oxide cathodes in PIBs concentrating on chemical formula, preparation method, test voltage window, average output voltage, electrochemical performance, and optimization strategy.

Chemical formula	Preparation method	Test voltage window	Average output voltage (vs K/K <sup>+</sup> )	Electrochemical performance	Optimization strategy
P2-K <sub>0.6</sub> CoO <sub>2</sub> microspheres <sup>[69]</sup>	Self-templating method	1.7–4.0 V	2.7 V	82 mAh g <sup>-1</sup> (10 mA g <sup>-1</sup> ), 87% (40 mA g <sup>-1</sup> , 300 cycles)	Micro/Nano structure construction
K <sub>0.6</sub> CoO <sub>2-x</sub> N <sub>x</sub> porous nanoframe <sup>[162]</sup>	Co-precipitation method	1.5–4.0 V	2.6 V	86 mAh g <sup>-1</sup> (50 mA g <sup>-1</sup> ), 77.3% (50 mA g <sup>-1</sup> , 400 cycles)	Micro/Nano structure construction
P2-Na <sub>0.84</sub> CoO <sub>2</sub> platelets <sup>[74]</sup>	Solution combustion synthesis method	2.0–4.2 V	3.0 V	82 mAh g <sup>-1</sup> (4.1 mA g <sup>-1</sup> ), 80% (8.2 mA g <sup>-1</sup> , 50 cycles)	Interlamellar space optimization
P2-K <sub>0.6</sub> CoO <sub>2</sub> particles <sup>[76]</sup>	Solid-state method	1.7–4.0 V	2.7 V	80 mAh g <sup>-1</sup> (2 mA g <sup>-1</sup> ), 60% (100 mA g <sup>-1</sup> , 120 cycles)	Interlayer stacking control
P2-K <sub>0.41</sub> CoO <sub>2</sub> particles <sup>[78]</sup>	Solid-state method	2.0–3.9 V	3.1 V	58 mAh g <sup>-1</sup> (11.8 mA g <sup>-1</sup> ), 92% (11.8 mA g <sup>-1</sup> , 30 cycles)	Interlayer stacking control
P3-K <sub>2/3</sub> CoO <sub>2</sub> particles <sup>[78]</sup>	Solid-state method	2.0–3.9 V	2.9 V	60 mAh g <sup>-1</sup> (11.5 mA g <sup>-1</sup> ), 90% (11.5 mA g <sup>-1</sup> , 30 cycles)	Interlayer stacking control
K <sub>0.3</sub> MnO <sub>2</sub> particles <sup>[62]</sup>	Pyrolysis method	1.5–3.5 V	2.55 V	70 mAh g <sup>-1</sup> (27.9 mA g <sup>-1</sup> ), 57% (27.9 mA g <sup>-1</sup> , 685 cycles)	Interlayer stacking control
P3-K <sub>0.5</sub> MnO <sub>2</sub> particles <sup>[76]</sup>	Solid-state method	1.5–3.9 V	2.65 V	100 mAh g <sup>-1</sup> (5 mA g <sup>-1</sup> ), 70% (20 mA g <sup>-1</sup> , 50 cycles)	Interlayer stacking control
K <sub>0.77</sub> MnO <sub>2</sub> •0.23H <sub>2</sub> O nanosheets <sup>[10]</sup>	Hydrothermal method	1.5–4.0 V	2.6 V	134 mAh g <sup>-1</sup> (100 mA g <sup>-1</sup> ), 93% (100 mA g <sup>-1</sup> , 100 cycles)	Interlamellar space optimization
P2-K <sub>0.3</sub> MnO <sub>2</sub> particles <sup>[85]</sup>	Co-precipitation method	1.5–4.0 V	2.75 V	118.0 mAh g <sup>-1</sup> (20 mA g <sup>-1</sup> ), 61.1% (20 mA g <sup>-1</sup> , 100 cycles)	Interlayer stacking control
P3-K <sub>0.45</sub> MnO <sub>2</sub> particles <sup>[85]</sup>	Co-precipitation method	1.5–4.0 V	2.75 V	128.6 mAh g <sup>-1</sup> (20 mA g <sup>-1</sup> ), 70.8% (20 mA g <sup>-1</sup> , 100 cycles)	Interlayer stacking control
K <sub>0.5</sub> MnO <sub>2</sub> particles <sup>[163]</sup>	Solid-state calcination method	2.0–4.2 V	2.95 V	120 mAh g <sup>-1</sup> (20 mA g <sup>-1</sup> ), 83% (20 mA g <sup>-1</sup> , 50 cycles)	Interlayer stacking control
K <sub>1.39</sub> Mn <sub>3</sub> O <sub>6</sub> spheres <sup>[103]</sup>	Typical precipitation method	1.5–4.0 V	2.55 V	110 mAh g <sup>-1</sup> (10 mA g <sup>-1</sup> ), 94.9% (50 mA g <sup>-1</sup> , 100 cycles)	Surface modification and coating
P2-K <sub>0.67</sub> MnO <sub>2</sub> particles <sup>[164]</sup>	Sol-gel method	1.7–4.0 V	2.7 V	78.0 mAh g <sup>-1</sup> (50 mA g <sup>-1</sup> ), 90.5% (50 mA g <sup>-1</sup> , 300 cycles)	Surface modification and coating
P3-K <sub>0.5</sub> MnO <sub>2</sub> hollow submicrosphere <sup>[165]</sup>	Two-step self-templating strategy	1.5–3.9 V	2.6 V	104 mAh g <sup>-1</sup> (10 mA g <sup>-1</sup> ), 89.1% (200 mA g <sup>-1</sup> , 400 cycles)	Micro/Nano structure construction
δ-K <sub>0.51</sub> V <sub>2</sub> O <sub>5</sub> nanobelts <sup>[71]</sup>	Chemical preintercalation method	2.0–4.5 V	3.20 V	131 mAh g <sup>-1</sup> (30 mA g <sup>-1</sup> ), 61.3% (100 mA g <sup>-1</sup> , 100 cycles)	Micro/Nano structure construction
K <sub>0.5</sub> V <sub>2</sub> O <sub>5</sub> belts <sup>[110]</sup>	Hydrothermal method	1.5–3.8 V	2.7 V	90 mAh g <sup>-1</sup> (10 mA g <sup>-1</sup> ), 81% (100 mA g <sup>-1</sup> , 250 cycles)	Micro/Nano structure construction
K <sub>2</sub> V <sub>3</sub> O <sub>8</sub> /C composite <sup>[114]</sup>	Solvothermal method	1.0–4.2 V	2.0 V	75 mAh g <sup>-1</sup> (20 mA g <sup>-1</sup> ), 80% (20 mA g <sup>-1</sup> , 200 cycles)	Surface modification and coating
O3-KCrO <sub>2</sub> particles <sup>[119]</sup>	Solid-state method	1.5–4.0 V	2.73 V	92 mAh g <sup>-1</sup> (5 mA g <sup>-1</sup> ), 67% (10 mA g <sup>-1</sup> , 100 cycles)	Interlamellar space optimization
P3-K <sub>0.69</sub> CrO <sub>2</sub> particles <sup>[121]</sup>	Electrochemical ion-exchange method	1.53–8 V	2.5 V	100 mAh g <sup>-1</sup> (100 mA g <sup>-1</sup> ), 65% (100 mA g <sup>-1</sup> , 1000 cycles)	Interlamellar space optimization
P3-K <sub>0.8</sub> CrO <sub>2</sub> particles <sup>[122]</sup>	Solid-state method	1.5–3.9 V	2.5 V	91 mAh g <sup>-1</sup> (10.9 mA g <sup>-1</sup> ), 99% (218 mA g <sup>-1</sup> , 300 cycles)	Interlamellar space optimization
K <sub>0.7</sub> Fe <sub>0.5</sub> Mn <sub>0.5</sub> O <sub>2</sub> nanowires <sup>[51]</sup>	Electrospinning method	1.5–4.0 V	2.55 V	178 mAh g <sup>-1</sup> (20 mA g <sup>-1</sup> ), 87% (1000 mA g <sup>-1</sup> , 450 cycles)	Micro/Nano structure construction
P2-K <sub>0.65</sub> Fe <sub>0.5</sub> Mn <sub>0.5</sub> O <sub>2</sub> microspheres <sup>[70]</sup>	Solvothermal method	1.5–4.2 V	2.5 V	151 mAh g <sup>-1</sup> (20 mA g <sup>-1</sup> ), 78% (100 mA g <sup>-1</sup> , 350 cycles)	Micro/Nano structure construction

**Table 1.** Continued.

Chemical formula	Preparation method	Test voltage window	Average output voltage (vs K/K <sup>+</sup> )	Electrochemical performance	Optimization strategy
P2-K <sub>0.45</sub> Mn <sub>0.8</sub> Fe <sub>0.2</sub> O <sub>2</sub> particles <sup>[166]</sup>	Solid-state method	1.5–4.0 V	2.6 V	106.2 mAh g <sup>-1</sup> (20 mA g <sup>-1</sup> ), 77.3% (20 mA g <sup>-1</sup> , 100 cycles)	Interlamellar space optimization
P3-K <sub>0.3</sub> Mn <sub>0.95</sub> Co <sub>0.05</sub> O <sub>2</sub> particles <sup>[167]</sup>	Sol-gel method	2.0–3.6 V	2.45 V	99 mAh g <sup>-1</sup> (22 mA g <sup>-1</sup> ), 75% (173 mA g <sup>-1</sup> , 500 cycles)	Interlayer stacking control
P2-K <sub>0.44</sub> Ni <sub>0.22</sub> Mn <sub>0.78</sub> O <sub>2</sub> particles <sup>[135]</sup>	Solid-state method	1.5–4.0 V	2.4 V	125.5 mAh g <sup>-1</sup> (10 mA g <sup>-1</sup> ), 67% (200 mA g <sup>-1</sup> , 500 cycles)	Surface modification
Na <sub>0.9</sub> Cr <sub>0.9</sub> Ru <sub>0.1</sub> O <sub>2</sub> particles <sup>[59]</sup>	Solid-state method	1.5–3.8 V	2.7 V	100.6 mAh g <sup>-1</sup> (10 mA g <sup>-1</sup> ), 81.2% (500 mA g <sup>-1</sup> , 500 cycles)	Interlamellar space optimization
P3-K <sub>0.45</sub> Mn <sub>0.9</sub> Mg <sub>0.1</sub> O <sub>2</sub> particles <sup>[83]</sup>	Solid-state method	1.5–4.0 V	2.45 V	108 mAh g <sup>-1</sup> (20 mA g <sup>-1</sup> ), 74.8% (20 mA g <sup>-1</sup> , 500 cycles)	High-energy ion doping
K <sub>0.4</sub> Fe <sub>0.5</sub> Mn <sub>0.5</sub> O <sub>2</sub> particles <sup>[133]</sup>	Solid-state method	1.5–3.8 V	2.8 V	120 mAh g <sup>-1</sup> (6 mA g <sup>-1</sup> ), 85% (125 mA g <sup>-1</sup> , 26 cycles)	Interlamellar space optimization
P3-K <sub>0.54</sub> [Co <sub>0.5</sub> Mn <sub>0.5</sub> ]O <sub>2</sub> particles <sup>[134]</sup>	Typical combustion method	1.5–3.9 V	2.85 V	120.4 mAh g <sup>-1</sup> (20 mA g <sup>-1</sup> ), 62% (20 mA g <sup>-1</sup> , 500 cycles)	Interlayer stacking control
P3-K <sub>0.48</sub> Mn <sub>0.4</sub> Co <sub>0.6</sub> O <sub>2</sub> particles <sup>[168]</sup>	Solid-state method	1.0–4.2 V	3.0 V	64 mAh g <sup>-1</sup> (0.05 C), 81% (0.1C mA g <sup>-1</sup> , 180 cycles)	Interlayer stacking control
P3-K <sub>0.67</sub> Mn <sub>0.83</sub> Ni <sub>0.17</sub> O <sub>2</sub> particles <sup>[136]</sup>	Solid-state method	1.5–3.8 V	2.5 V	122 mAh g <sup>-1</sup> (20 mA g <sup>-1</sup> ), 75% (500 mA g <sup>-1</sup> , 200 cycles)	Interlamellar space optimization
P2-K <sub>0.75</sub> [Ni <sub>1/3</sub> Mn <sub>2/3</sub> ]O <sub>2</sub> particles <sup>[131]</sup>	Spray pyrolysis method	1.5–4.3 V	2.95 V	110 mAh g <sup>-1</sup> (20 mA g <sup>-1</sup> ), 86% (20 mA g <sup>-1</sup> , 300 cycles)	Interlamellar space optimization
P3-K <sub>0.5</sub> [Ni <sub>0.1</sub> Mn <sub>0.9</sub> ]O <sub>2</sub> particles <sup>[169]</sup>	Solid-state method	1.5–3.9 V	2.75 V	121 mAh g <sup>-1</sup> (10 mA g <sup>-1</sup> ), 82% (100 mA g <sup>-1</sup> , 100 cycles)	Interlamellar space optimization
P2-K <sub>0.83</sub> [Ni <sub>0.05</sub> Mn <sub>0.95</sub> ]O <sub>2</sub> particles <sup>[170]</sup>	Spray pyrolysis and electrochemical ion exchange	1.5–4.3 V	2.7 V	155 mAh g <sup>-1</sup> (52 mA g <sup>-1</sup> ), 77% (520 mA g <sup>-1</sup> , 500 cycles)	Interlamellar space optimization
P2-K <sub>0.64</sub> Na <sub>0.04</sub> [Ni <sub>1/3</sub> Mn <sub>2/3</sub> ]O <sub>2</sub> particles <sup>[171]</sup>	Solid-state method and electrochemical ion exchange	1.5–4.5 V	2.6 V	82 mAh g <sup>-1</sup> (86 mA g <sup>-1</sup> ), 75 mAh g <sup>-1</sup> (2580 mA g <sup>-1</sup> )	Interlamellar space optimization
P3-K <sub>0.7</sub> Mn <sub>0.7</sub> Ni <sub>0.3</sub> O <sub>2</sub> particles <sup>[172]</sup>	Solid-state method	1.5–3.9 V	3.0 V	125.4 mAh g <sup>-1</sup> (100 mA g <sup>-1</sup> ), 88.5% (1000 mA g <sup>-1</sup> , 800 cycles)	Interlamellar space optimization
K <sub>0.7</sub> Mn <sub>0.7</sub> Mg <sub>0.3</sub> O <sub>2</sub> microparticles <sup>[141]</sup>	Resorcinol-formaldehyde method	1.5–4.0 V	2.47 V	144.5 mAh g <sup>-1</sup> (20 mA g <sup>-1</sup> ), 82.5% (100 mA g <sup>-1</sup> , 400 cycles)	Interlamellar space optimization
K <sub>5/9</sub> Mn <sub>7/9</sub> Ti <sub>2/9</sub> O <sub>2</sub> particles <sup>[139]</sup>	Solid-state method	1.5–4.2 V	2.8 V	135 mAh g <sup>-1</sup> (20 mA g <sup>-1</sup> ), 70% (100 mA g <sup>-1</sup> , 100 cycles)	Interlamellar space optimization
P3-K <sub>0.5</sub> Mn <sub>0.8</sub> Co <sub>0.1</sub> Ni <sub>0.1</sub> O <sub>2</sub> porous microcuboids <sup>[147]</sup>	Co-precipitation method	1.5–4.0 V	2.4 V	94.5 mAh g <sup>-1</sup> (20 mA g <sup>-1</sup> ), 61% (100 mA g <sup>-1</sup> , 300 cycles)	Micro/Nano structure construction
P3-K <sub>0.5</sub> Mn <sub>0.72</sub> Ni <sub>0.15</sub> Co <sub>0.13</sub> O <sub>2</sub> microspheres <sup>[148]</sup>	Solvent-thermal method	1.5–4.0 V	2.6 V	82.5 mAh g <sup>-1</sup> (10 mA g <sup>-1</sup> ), 75% (200 mA g <sup>-1</sup> , 300 cycles)	Micro/Nano structure construction
P3-K <sub>0.48</sub> Ni <sub>0.2</sub> Co <sub>0.2</sub> Mn <sub>0.6</sub> O <sub>2</sub> microsphere and microcube <sup>[173]</sup>	Solvothermal method and solid-state method	1.5–4.0 V	2.3 V	57 mAh g <sup>-1</sup> (40 mA g <sup>-1</sup> ), 71% (400 mA g <sup>-1</sup> , 350 cycles)	Micro/Nano structure construction
K <sub>0.67</sub> Ni <sub>0.17</sub> Co <sub>0.17</sub> Mn <sub>0.66</sub> O <sub>2</sub> particles <sup>[147]</sup>	Co-precipitation method	2.0–4.3 V	3.10 V	76.5 mAh g <sup>-1</sup> (20 mA g <sup>-1</sup> ), 87% (20 mA g <sup>-1</sup> , 100 cycles)	Interlamellar space optimization
P3-K <sub>0.45</sub> Ni <sub>0.1</sub> Co <sub>0.1</sub> Al <sub>0.05</sub> Mn <sub>0.75</sub> O <sub>2</sub> particles <sup>[149]</sup>	Co-precipitation method	1.5–4.0 V	2.4 V	89.2 mAh g <sup>-1</sup> (10 mA g <sup>-1</sup> ), 77.4% (20 mA g <sup>-1</sup> , 100 cycles)	Interlamellar space optimization
K <sub>0.37</sub> Na <sub>0.3</sub> Ni <sub>0.17</sub> Co <sub>0.17</sub> Mn <sub>0.66</sub> O <sub>2</sub> particles <sup>[174]</sup>	Co-precipitation method	2.0–4.2 V	3.05 V	86.1 mAh g <sup>-1</sup> (20 mA g <sup>-1</sup> ), 91.5% (20 mA g <sup>-1</sup> , 100 cycles)	Interlayer stacking control
P3-K <sub>0.5</sub> [Mn <sub>0.8</sub> Fe <sub>0.1</sub> Ni <sub>0.1</sub> ]O <sub>2</sub> particles <sup>[148]</sup>	Typical combustion method	1.5–3.9 V	2.6 V	120 mAh g <sup>-1</sup> (50 mA g <sup>-1</sup> ), 74% (50 mA g <sup>-1</sup> , 300 cycles)	Interlayer stacking control
P2-K <sub>0.75</sub> [Mn <sub>0.8</sub> Ni <sub>0.1</sub> Fe <sub>0.1</sub> ]O <sub>2</sub> particles <sup>[149]</sup>	Solid-state method and electrochemical ion exchange	1.5–3.9 V	2.6 V	110 mAh g <sup>-1</sup> (10 mA g <sup>-1</sup> ), 70% (100 mA g <sup>-1</sup> , 200 cycles)	Interlayer stacking control
P3-K <sub>0.6</sub> Mn <sub>0.8</sub> Ni <sub>0.1</sub> Ti <sub>0.1</sub> O <sub>2</sub> particles <sup>[153]</sup>	Solid-state method	1.5–4.2 V	2.6 V	118 mAh g <sup>-1</sup> (10 mA g <sup>-1</sup> ), 88% (200 mA g <sup>-1</sup> , 100 cycles)	Interlayer stacking control
P3-K <sub>0.4</sub> Fe <sub>0.1</sub> Mn <sub>0.8</sub> Ti <sub>0.1</sub> O <sub>2</sub> particles <sup>[155]</sup>	Solid-state method	1.8–4.2 V	2.75 V	117 mAh g <sup>-1</sup> (20 mA g <sup>-1</sup> ), 74% (200 mA g <sup>-1</sup> , 300 cycles)	Interlayer stacking control

**Table 1.** Continued.

Chemical formula	Preparation method	Test voltage window	Average output voltage (vs K/K <sup>+</sup> )	Electrochemical performance	Optimization strategy
P3-K <sub>0.5</sub> Mn <sub>0.7</sub> Co <sub>0.2</sub> Fe <sub>0.1</sub> O <sub>2</sub> particles <sup>[175]</sup>	Solid-state method	1.7–3.9 V	2.6 V	104 mAh g <sup>-1</sup> (20 mA g <sup>-1</sup> ), 71% (200 mA g <sup>-1</sup> , 300 cycles)	Interlayer stacking control
P3-K <sub>1/2</sub> Mn <sub>5/6</sub> Mg <sub>1/12</sub> Ni <sub>1/12</sub> O <sub>2</sub> particles <sup>[176]</sup>	Sol-gel method	1.5–3.9 V	2.6 V	83.6 mAh g <sup>-1</sup> (120 mA g <sup>-1</sup> ), 70.4% (120 mA g <sup>-1</sup> , 200 cycles)	Interlayer stacking control
P3-K <sub>0.45</sub> Co <sub>1/12</sub> Mg <sub>1/12</sub> Mn <sub>5/6</sub> O <sub>2</sub> particles <sup>[150]</sup>	Sol-gel method	1.5–3.9 V	2.7 V	98 mAh g <sup>-1</sup> (120 mA g <sup>-1</sup> ), 54.8% (1000 mA g <sup>-1</sup> , 500 cycles)	Interlayer stacking control

high-performance PIB research, with the hope that the ideas presented will inspire researchers in the field of PIB research.

### 7.1. High-Throughput Computational Simulations and Machine Learning

In recent years, high-throughput computational simulation has greatly accelerated the search for new battery electrode materials. The purpose is to rely on first-principles methods to calculate the materials properties in advance through solving the basic equations of quantum and statistical mechanics, so as to achieve synthetic purpose.<sup>[177–179]</sup> Various electronic-structure methods in high-throughput computational simulations can be employed to determine the effective K<sup>+</sup> ion storage sites, K<sup>+</sup>/e<sup>-</sup> transport kinetics, structure of the layered cathode materials, achieving the purpose of developing high-capacity, high-rate, and long-life PIBs.<sup>[180]</sup>

Artificial intelligence (AI) provides a new way to bring breakthroughs in material science, and machine learning is the core of AI. Machine learning is a special application of AI in which computers learn from massive data and experience through a series of algorithms without reprogramming.<sup>[181,182]</sup> Recently, machine learning has emerged as an effective modeling approach in the energy storage field to determine relevant parameters of electrode materials, battery health and remaining useful life.<sup>[179,182]</sup> Electrode materials and cells will be screened quickly in parallel based on realistic working conditions (such as mass loading, open-circuit voltage, closed circuit current, initial specific capacity, and first coulombic efficiency) to generate huge volumes of meaningful data.<sup>[183]</sup> Once machine learning models are simulated using this data, they will further speed up the process of material design, electrode preparation and cell testing, eliminating potentially poor performing electrodes and batteries based on their initial state or initial cycling tests.<sup>[182,183]</sup> Therefore, the application of high-throughput computational simulations and machine learning will accelerate the research and development process of high-performance layered transition-metal oxide cathodes and PIB devices, with a view to achieving large-scale application of PIBs.

### 7.2. Preparation Science Innovation under Multi-Field and Extreme Conditions

An effective synthesis method is a prerequisite for the design and construction of electrode materials. We should combine

the knowledge of chemistry, physics, and materials science to deeply study micro-processes and internal synthesis mechanisms to achieve accurate design.<sup>[184]</sup> The breakthrough in synthetic method can obtain electrode materials with novel morphology and structure under multi-field (electric field, magnetic field, force field, etc.) and extreme conditions (Ultra-fast heating/cooling, ultra-high temperature, ultra-high pressure, etc.), which is expected to greatly improve the K storage performance of layered transition-metal oxide cathodes.

### 7.3. Multi-Scale and Multi-Dimensional Collaborative Optimization Strategy

Based on the research experience of LIBs and SIBs, micro/nano structure construction, interlayer stacking control, high-energy ion doping, surface modification and coating, interlaminar space optimization are important strategies to construct high-performance electrode materials and obtain efficient energy storage devices.<sup>[185,186]</sup> From the atomic, molecular, mesoscopic and other multi-scale levels, combining these optimization strategies is an effective means to obtain high performance layered transition-metal oxide cathodes.

### 7.4. High-Resolution In Situ Characterization

High-resolution structural in situ characterization is indispensable for the understanding and advance of electrode materials for electrochemical devices.<sup>[158]</sup> Recently, the upgrading of new electron microscope technology has promoted the rapid development of electrochemical materials and devices, such as Cryo-SEM, STEM, and spherical aberration corrected TEM. Therefore, the development of new in situ characterization methods based on these advanced electron microscope technologies, including detecting the real-time evolution of material morphology structure, crystal structure, interface structure, phase composition, is urgent and powerful. These new in situ methods will provide strong support for the advance of layered transition-metal oxide cathodes and analysis of the intrinsic storage mechanism.

### 7.5. Advanced Micro/Nano Devices for Direct Probing

The in-depth study of electrodes has an important impact on the realization of remarkable energy storage devices. In

practical condition, active electrodes are blended with binders, conductive agents, and electrolytes, which significantly hamper the exploration of electrochemical processes in conventional tests. Therefore, advanced in situ characterization techniques for micro/nanoscale electrochemical devices can directly probe electrochemical properties using single nanostructures, a powerful diagnostic tool to reveal the internal K storage mechanism of layered transition-metal oxide cathodes. The challenge for a micro-/nanoscale electrochemical device in situ characterization of layered transition-metal oxide cathodes is that synthesis and preparation a single nanostructure to meet the requirements of device construction, such as nanowire, nanofiber, nanosheet, and nanofilm.

### 7.6. Development and Optimization of High Voltage Electrolyte

The development of high-voltage electrolytes is the key to highlighting the advantages of high energy density in PIBs. For most layered transition-metal oxide cathodes, the theoretical operating voltage window can often reach more than 4.5 V, however, the working cut-off voltage of the electrolyte has been reported to be less than 4.0 V. Therefore, the development of new electrolytes that can work stably at higher voltages is critical to the development of layered cathode materials to take advantage of high specific energy and promote the development of PIBs. The development of low-fluoride polyether-based electrolytes with additives and sulfonylamide-based ionic liquids may be the main research directions of high-voltage electrolyte for PIBs in the future (Figure 22).

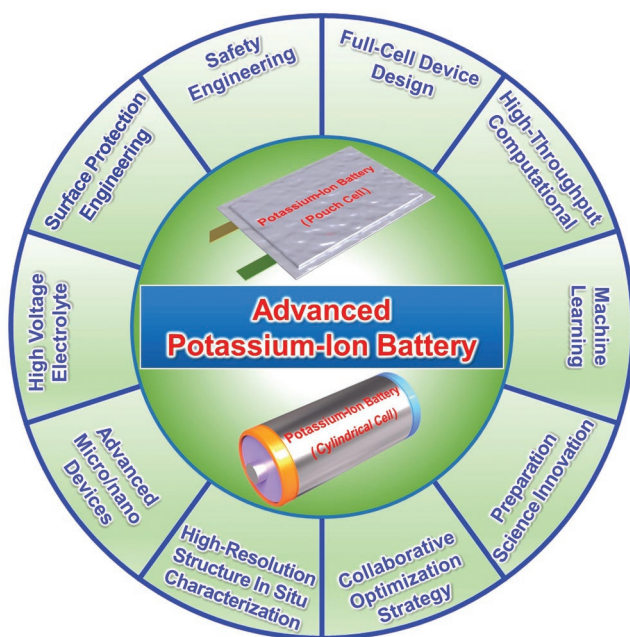


**Figure 22.** Forecast of the main research directions and hot spots of PIBs in the future.

### 7.7. Surface Protection Engineering to Improve Air Stability

Water contamination of electrodes should be effectively prevented in non-aqueous rechargeable batteries to restrain side reactions such as adsorbed water oxidation.<sup>[96]</sup> The easily desorbable deliquescent property is one of the important challenges facing cathode materials, which seriously affects the electrode preparation efficiency, electrochemical potassium storage characteristics, and material storage life.<sup>[148]</sup> Therefore, through the surface protection engineering to improve air stability and reduce water-absorbing deliquescence properties is the hotspot and frontier of future research in the field of layered transition-metal oxide cathodes.

### 7.8. Full-Cell Device Design and Safety Engineering for Practical Applications

In order to make electrode materials close to practical application or commercialization, full-cell research is very indispensable. However, making full cells of PIBs is relatively difficult because it requires careful calculations and pairings based on well-defined reaction mechanisms and each electrode (both cathode and anode).<sup>[187,188]</sup> Although a series of pioneering works have been emerged on full-cell PIBs with reasonable capacities, some of which show higher energy/power densities than full-cell SIBs, their cycle life and energy output are far from practical commercialization. Further investigation on full-cell PIBs will focus on individual electrode optimization, electrochemical mechanisms, and full-cell fabrication techniques.

Although LIBs have been successfully commercialized over the past few decades, safety concerns remain a major concern for batteries.<sup>[28,189]</sup> Its organic flammable electrolytes inherently pose a safety threat during charge/discharge, in which the possibility of thermal runaway seems to be a major safety hazard. The problem of thermal runaway still exists in PIBs with layered transition-metal oxide cathodes and organic electrolyte as important components. Based on the research experience of LIB packs, combining theory and experiments to monitor the thermal runaway mechanism and temperature distribution of PIBs.<sup>[37,184]</sup> Specifically, there are three possible ways to address the security issues of PIBs<sup>195</sup>: 1) the design and preparation of new-type layered transition-metal oxide cathodes and non-flame retardant separators with excellent thermal stability, high ignition point, and thermal blocking characteristics; 2) the development of quasi-solid and solid electrolytes to reduce the risk of internal short circuits and thermal explosions; 3) reduce the inherent oxygen content in the various components of the PIB cell.

### Acknowledgements

X.W., Z.X., and K.H. contributed equally to this work. This work was supported by the National Natural Science Foundation of China (21905218, 51832004), the National Key Research and Development Program of China (2020YFA0715000), the Guangdong Basic and Applied Basic Research Foundation (2020A1515110402), the Sanya Science and Education Innovation Park of Wuhan University of Technology (2021KF0019), and the Fundamental Research Funds for the Central Universities (WUT: 2021CG014).

## Conflict of Interest

The authors declare no conflict of interest.

## Keywords

in situ characterization techniques, crystal structures, layered transition-metal oxide, potassium-ion batteries

Received: August 21, 2022

Revised: October 8, 2022

Published online:

- [1] C. Niu, J. Meng, X. Wang, C. Han, M. Yan, K. Zhao, X. Xu, W. Ren, Y. Zhao, L. Xu, Q. Zhang, D. Zhao, L. Mai, *Nat. Commun.* **2015**, *6*, 7402.
- [2] B. Kang, G. Ceder, *Nature* **2009**, *458*, 190.
- [3] B. Dunn, H. Kamath, J.-M. Tarascon, *Science* **2011**, *334*, 928.
- [4] A. Manthiram, *Nat. Commun.* **2020**, *11*, 1550.
- [5] Y. Li, Y. Lu, P. Adelhelm, M.-M. Titirici, Y.-S. Hu, *Chem. Soc. Rev.* **2019**, *48*, 4655.
- [6] G. Li, B. Huang, Z. Pan, X. Su, Z. Shao, L. An, *Energy Environ. Sci.* **2019**, *12*, 2030.
- [7] K. Han, J. Meng, X. Hong, X. Wang, L. Mai, *Nanoscale* **2020**, *12*, 8255.
- [8] A. Manthiram, A. V. Murugan, A. Sarkar, T. Muraliganth, *Wiley Interdiscip. Rev. Energy Environ.* **2008**, *1*, 621.
- [9] K. Kubota, M. Dahbi, T. Hosaka, S. Kumakura, S. Komaba, *Chem. Rec.* **2018**, *18*, 459.
- [10] B. Lin, X. Zhu, L. Fang, X. Liu, S. Li, T. Zhai, L. Xue, Q. Guo, J. Xu, H. Xia, *Adv. Mater.* **2019**, *31*, 1900060.
- [11] N. Yabuuchi, K. Kubota, M. Dahbi, S. Komaba, *Chem. Rev.* **2014**, *114*, 11636.
- [12] X. Wang, C. Niu, J. Meng, P. Hu, X. Xu, X. Wei, L. Zhou, K. Zhao, W. Luo, M. Yan, L. Mai, *Adv. Energy Mater.* **2015**, *5*, 1500716.
- [13] X. Wang, C. Wang, K. Han, C. Niu, J. Meng, P. Hu, X. Xu, Z. Wang, Q. Li, C. Han, Y. Huang, L. Mai, *Adv. Energy Mater.* **2018**, *8*, 1802180.
- [14] X. Wei, X. Wang, X. Tan, Q. An, L. Mai, *Adv. Funct. Mater.* **2018**, *28*, 1804458.
- [15] Q. Liu, Z. Hu, M. Chen, C. Zou, H. Jin, S. Wang, S.-L. Chou, Y. Liu, S.-X. Dou, *Adv. Funct. Mater.* **2020**, *30*, 1909530.
- [16] H. Pan, Y.-S. Hu, L. Chen, *Energy Environ. Sci.* **2013**, *6*, 2338.
- [17] Y.-H. Zhu, X. Yang, T. Sun, S. Wang, Y.-L. Zhao, J.-M. Yan, X.-B. Zhang, *Electrochem. Energy Rev.* **2018**, *1*, 548.
- [18] X. Zou, P. Xiong, J. Zhao, J. Hu, Z. Liu, Y. Xu, *Phys. Chem. Chem. Phys.* **2017**, *19*, 26495.
- [19] A. Eftekhari, Z. Jian, X. Ji, *ACS Appl. Mater. Interfaces* **2017**, *9*, 4404.
- [20] Z. Liu, H. Deng, S. Zhang, W. Hu, F. Gao, *J. Mater. Chem. A* **2018**, *6*, 3171.
- [21] M. Huang, J. Meng, Z. Huang, X. Wang, L. Mai, *J. Mater. Chem. A* **2020**, *8*, 6631.
- [22] R. Rajagopalan, Y. Tang, X. Ji, C. Jia, H. Wang, *Adv. Funct. Mater.* **2020**, *30*, 1909486.
- [23] J. Wang, B. Yin, T. Gao, X. Wang, W. Li, X. Hong, Z. Wang, H. He, *Acta Phys.-Chim. Sin.* **2022**, *38*, 2104030.
- [24] Z. Zhang, L. Duan, Y. Xu, C. Zhao, J. Bao, J. Shen, X. Zhou, *J. Energy Chem.* **2022**, *73*, 126.
- [25] K. Guo, S. Qi, H. Wang, J. Huang, M. Wu, Y. Yang, X. Li, Y. Ren, J. Ma, *Small Sci.* **2022**, *2*, 2100107.
- [26] Y.-S. Xu, S.-Y. Duan, Y.-G. Sun, D.-S. Bin, X.-S. Tao, D. Zhang, Y. Liu, A.-M. Cao, L.-J. Wan, *J. Mater. Chem. A* **2019**, *7*, 4334.
- [27] X. Wu, D. P. Leonard, X. Ji, *Chem. Mater.* **2017**, *29*, 5031.
- [28] Y. An, Y. Liu, X. Xu, Y. Ma, H. Wei, C. Ma, J. Feng, *Funct. Mater. Lett.* **2019**, *12*, 1930002.
- [29] T. Hosaka, K. Kubota, A. S. Hameed, S. Komaba, *Chem. Rev.* **2020**, *120*, 6358.
- [30] X. Wang, K. Han, C. Wang, Z. Liu, X. Xu, M. Huang, P. Hu, J. Meng, Q. Li, L. Mai, *Chem. Commun.* **2018**, *54*, 11029.
- [31] H. Fei, Y. Liu, Y. An, X. Xu, G. Zeng, Y. Tian, L. Ci, B. xi, S. Xiong, J. Feng, *J. Power Sources* **2018**, *399*, 294.
- [32] B. Tian, W. Tang, C. Su, Y. Li, *ACS Appl. Mater. Interfaces* **2018**, *10*, 642.
- [33] M. Qin, W. Ren, J. Meng, X. Wang, X. Yao, Y. Ke, Q. Li, L. Mai, *ACS Sustainable Chem. Eng.* **2019**, *7*, 11564.
- [34] P. Hundekar, S. Basu, X. Fan, L. Li, A. Yoshimura, T. Gupta, V. Sarbada, A. Lakhot, R. Jain, S. Narayanan, Y. Shi, C. Wang, N. Koratkar, *Proc. Natl. Acad. Sci. U. S. A.* **2020**, *117*, 5588.
- [35] A. S. Hameed, A. Katogi, K. Kubota, S. Komaba, *Adv. Energy Mater.* **2019**, *9*, 1902528.
- [36] K. Yuan, R. Ning, M. Bai, N. Hu, K. Zhang, J. Gu, Q. Li, Y. Huang, C. Shen, K. Xie, *Energy Technol.* **2020**, *8*, 1900796.
- [37] J.-Y. Hwang, S.-T. Myung, Y.-K. Sun, *Adv. Funct. Mater.* **2018**, *28*, 1802938.
- [38] C. Han, K. Han, X. Wang, C. Wang, Q. Li, J. Meng, X. Xu, Q. He, W. Luo, L. Wu, L. Mai, *Nanoscale* **2018**, *10*, 6820.
- [39] W. Luo, F. Li, W. Zhang, K. Han, J.-J. Gaumet, H.-E. Schaefer, L. Mai, *Nano Res.* **2019**, *12*, 1025.
- [40] D. Yang, C. Liu, X. Rui, Q. Yan, *Nanoscale* **2019**, *11*, 15402.
- [41] J. Xu, Y. Dou, Z. Wei, J. Ma, Y. Deng, Y. Li, H. Liu, S. Dou, *Adv. Sci.* **2017**, *4*, 1700146.
- [42] S. Komaba, T. Hasegawa, M. Dahbi, K. Kubota, *Electrochem. Commun.* **2015**, *60*, 172.
- [43] L. Xue, H. Gao, Y. Li, J. B. Goodenough, *J. Am. Chem. Soc.* **2018**, *140*, 3292.
- [44] T. Hosaka, S. Muratsubaki, K. Kubota, H. Onuma, S. Komaba, *J. Phys. Chem. Lett.* **2019**, *10*, 3296.
- [45] Y. Ding, X. Guo, Y. Qian, L. Zhang, L. Xue, J. B. Goodenough, G. Yu, *Adv. Mater.* **2019**, *31*, 1806956.
- [46] Q. Qu, L. Li, S. Tian, W. Guo, Y. Wu, R. Holze, *J. Power Sources* **2010**, *195*, 2789.
- [47] T. Yamamoto, K. Matsumoto, R. Hagiwara, T. Nohira, *J. Phys. Chem. C* **2017**, *121*, 18450.
- [48] J. B. Goodenough, K.-S. Park, *J. Am. Chem. Soc.* **2013**, *135*, 1167.
- [49] H. Kim, J. C. Kim, M. Bianchini, D.-H. Seo, J. Rodriguez-Garcia, G. Ceder, *Adv. Energy Mater.* **2018**, *8*, 1702384.
- [50] J. Zheng, Y. Ye, T. Liu, Y. Xiao, C. Wang, F. Wang, F. Pan, *Acc. Chem. Res.* **2019**, *52*, 2201.
- [51] X. Wang, X. Xu, C. Niu, J. Meng, M. Huang, X. Liu, Z. Liu, L. Mai, *Nano Lett.* **2017**, *17*, 544.
- [52] J. C. Pramudita, D. Sehwat, D. Goonetilleke, N. Sharma, *Adv. Energy Mater.* **2017**, *7*, 1602911.
- [53] Z. Li, C. Ban, N. A. Chernova, Z. Wu, S. Upreti, A. Dillon, M. S. Whittingham, *J. Power Sources* **2014**, *268*, 106.
- [54] Z. Lu, H. Wang, D. Kong, K. Yan, P.-C. Hsu, G. Zheng, H. Yao, Z. Liang, X. Sun, Y. Cui, *Nat. Commun.* **2014**, *5*, 4345.
- [55] J.-L. Yue, W.-W. Yin, M.-H. Cao, S. Zulipiya, Y.-N. Zhou, Z.-W. Fu, *Chem. Commun.* **2015**, *51*, 15712.
- [56] A. Manthiram, B. Song, W. Li, *Energy Storage Mater.* **2017**, *6*, 125.
- [57] W. Liu, P. Oh, X. Liu, M. J. Lee, W. Cho, S. Chae, Y. Kim, J. Cho, *Angew. Chem., Int. Ed. Engl.* **2015**, *54*, 4440.
- [58] U. H. Kim, D. W. Jun, K. J. Park, Q. Zhang, P. Kaghazchi, D. Aurbach, D. T. Major, G. Goobes, M. Dixit, N. Leifer, C. M. Wang, P. Yan, D. Ahn, K. H. Kim, C. S. Yoon, Y. K. Sun, *Energy Environ. Sci.* **2018**, *11*, 1271.
- [59] H. Zhang, K. Xi, K. Jiang, X. Zhang, Z. Liu, S. Guo, H. Zhou, *Chem. Commun.* **2019**, *55*, 7910.

- [60] H. Zhang, L. Wang, X. He, *Battery Energy* **2022**, 1, 20210011.
- [61] C. Delmas, C. Fouassier, P. Hagenmuller, *J. Solid State Chem.* **1975**, 13, 165.
- [62] C. Vaalma, G. A. Giffin, D. Buchholz, S. Passerini, *J. Electrochem. Soc.* **2016**, 163, A1295.
- [63] S. Zhao, Z. Liu, G. Xie, Z. Guo, S. Wang, J. Zhou, X. Xie, B. Sun, S. Guo, G. Wang, *Energy Environ. Sci.* **2022**, 15, 3015.
- [64] J. Liao, Q. Hu, X. Sheng, Z. Zhang, Y. Xu, X. Mo, X. Zhou, *ACS Mater. Lett.* **2022**, 4, 1653.
- [65] A. Manthiram, J. C. Knight, S.-T. Myung, S.-M. Oh, Y.-K. Sun, *Adv. Energy Mater.* **2016**, 6, 1501010.
- [66] M. Leng, J. Bi, W. Wang, R. Liu, C. Xia, *Ionics* **2019**, 25, 1105.
- [67] H.-H. Ryu, K.-J. Park, D. R. Yoon, A. Aishova, C. S. Yoon, Y.-K. Sun, *Adv. Energy Mater.* **2019**, 9, 1902698.
- [68] G.-T. Park, H.-H. Ryu, N.-Y. Park, C. S. Yoon, Y.-K. Sun, *J. Power Sources* **2019**, 442, 227242.
- [69] T. Deng, X. Fan, C. Luo, J. Chen, L. Chen, S. Hou, N. Eidson, X. Zhou, C. Wang, *Nano Lett.* **2018**, 18, 1522.
- [70] T. Deng, X. Fan, J. Chen, L. Chen, C. Luo, X. Zhou, J. Yang, S. Zheng, C. Wang, *Adv. Funct. Mater.* **2018**, 28, 1800219.
- [71] Y.-H. Zhu, Q. Zhang, X. Yang, E.-Y. Zhao, T. Sun, X.-B. Zhang, S. Wang, X.-Q. Yu, J.-M. Yan, Q. Jiang, *Chem* **2019**, 5, 168.
- [72] J.-J. Braconnier, C. Delmas, C. Fouassier, P. Hagenmuller, *Mater. Res. Bull.* **1980**, 15, 1797.
- [73] C. Delmas, J.-J. Braconnier, C. Fouassier, P. Hagenmuller, *Solid State Ionics* **1981**, 3, 165.
- [74] K. Sada, B. Senthilkumar, P. Barpanda, *Chem. Commun.* **2017**, 53, 8588.
- [75] M. Jansen, R. Hoppe, *Z. Anorg. Allg. Chem.* **1975**, 417, 31.
- [76] A. R. Kamali, H.-K. Kim, K.-B. Kim, R. V. Kumar, D. J. Fray, *J. Mater. Chem. A* **2017**, 5, 19126.
- [77] M. Y. Toriyama, J. L. Kaufman, A. V. d. Ven, *ACS Appl. Electron. Mater.* **2019**, 2, 2629.
- [78] Y. Hironaka, K. Kubota, S. Komaba, *Chem. Commun.* **2017**, 53, 3693.
- [79] Y. Fang, X.-Y. Yu, X. W. Lou, *Angew. Chem., Int. Ed. Engl.* **2017**, 56, 5801.
- [80] J.-Y. Hwang, S.-M. Oh, S.-T. Myung, K. Y. Chung, I. Belharouak, Y.-K. Sun, *Nat. Commun.* **2015**, 6, 6865.
- [81] M. Guignard, C. Didier, J. Darriet, P. Bordet, E. Elkaïm, C. Delmas, *Nat. Mater.* **2013**, 12, 74.
- [82] M. Jansen, F. M. Chang, R. Hoppe, *Z. Anorg. Allg. Chem.* **1982**, 490, 101.
- [83] C.-I. Liu, S.-h. Luo, H.-b. Huang, Y.-c. Zhai, Z.-w. Wang, *ChemElectroChem* **2019**, 6, 2308.
- [84] C. Delmas, C. Fouassier, *Z. Anorg. Allg. Chem.* **1976**, 420, 184.
- [85] C.-I. Liu, S.-h. Luo, H.-b. Huang, Y.-c. Zhai, Z.-w. Wang, *Chem. Eng. J.* **2019**, 356, 53.
- [86] H. Kim, D.-H. Seo, J. C. Kim, S.-H. Bo, L. Liu, T. Shi, G. Ceder, *Adv. Mater.* **2017**, 29, 1702480.
- [87] K. W. Nam, S. Kim, E. Yang, Y. Jung, E. Levi, D. Aurbach, J. W. Choi, *Chem. Mater.* **2015**, 27, 3721.
- [88] A. Gao, M. Li, N. Guo, D. Qiu, Y. Li, S. Wang, X. Lu, F. Wang, R. Yang, *Adv. Energy Mater.* **2019**, 9, 1802739.
- [89] C. Li, H. P. Zhang, L. J. Fu, H. Liu, Y. P. Wu, E. Rahm, R. Holze, H. Q. Wu, *Electrochim. Acta* **2006**, 51, 3872.
- [90] J. H. Jo, J. U. Choi, A. Konarov, H. Yashiro, S. Yuan, L. Shi, Y.-K. Sun, S.-T. Myung, *Adv. Funct. Mater.* **2018**, 28, 1705968.
- [91] J. Cho, Y. J. Kim, T.-J. Kim, B. Park, *Angew. Chem., Int. Ed. Engl.* **2001**, 40, 3367.
- [92] S. Bao, S.-H. Luo, J.-L. Lu, *Ceram. Int.* **2020**, 46, 16080.
- [93] B. Xiao, H. Liu, J. Liu, Q. Sun, B. Wang, K. Kaliyappan, Y. Zhao, M. N. Banis, Y. Liu, R. Li, T.-K. Sham, G. A. Botton, M. Cai, X. Sun, *Adv. Mater.* **2017**, 29, 1703764.
- [94] S. Guo, Q. Li, P. Liu, M. Chen, H. Zhou, *Nat. Commun.* **2017**, 8, 135.
- [95] Y. Yu, W. Kong, Q. Li, D. Ning, G. Schuck, G. Schumacher, C. Su, X. Liu, *ACS Appl. Electron. Mater.* **2020**, 3, 933.
- [96] W. Liu, X. Li, D. Xiong, Y. Hao, J. Li, H. Kou, B. Yan, D. Li, S. Lu, A. Koo, K. Adair, X. Sun, *Nano Energy* **2018**, 44, 111.
- [97] Y. Zhang, L. Liu, S. Jamil, J. Xie, W. Liu, J. Xia, S. Nie, X. Wang, *Appl. Surf. Sci.* **2019**, 494, 1156.
- [98] J. Zheng, M. Gu, J. Xiao, B. J. Polzin, P. Yan, X. Chen, C. Wang, J.-G. Zhang, *Chem. Mater.* **2014**, 26, 6320.
- [99] Y.-K. Sun, M.-J. Lee, C. S. Yoon, J. Hassoun, K. Amine, B. Scrosati, *Adv. Mater.* **2012**, 24, 1192.
- [100] H.-H. Sun, J.-Y. Hwang, C. S. Yoon, A. Heller, C. B. Mullins, *ACS Nano* **2018**, 12, 12912.
- [101] E. Hu, X. Yu, R. Lin, X. Bi, J. Lu, S. Bak, K.-W. Nam, H. L. Xin, C. Jaye, D. A. Fischer, K. Amine, X.-Q. Yang, *Nat. Energy* **2018**, 3, 690.
- [102] B. C. Park, H. B. Kim, S. T. Myung, K. Amine, I. Belharouak, S. M. Lee, Y. K. Sun, *J. Power Sources* **2008**, 178, 826.
- [103] S. Zhao, K. Yan, P. Munroe, B. Sun, G. Wang, *Adv. Energy Mater.* **2019**, 9, 1803757.
- [104] R. Baddour-Hadjean, A. Boudaoud, S. Bach, N. Emery, J.-P. Pereira-Ramos, *Inorg. Chem.* **2014**, 53, 1764.
- [105] J. Meng, Z. Liu, C. Niu, X. Xu, X. Liu, G. Zhang, X. Wang, M. Huang, Y. Yu, L. Mai, *J. Mater. Chem. A* **2016**, 4, 4893.
- [106] G. Fang, J. Zhou, Y. Hu, X. Cao, Y. Tang, S. Liang, *J. Power Sources* **2015**, 275, 694.
- [107] G. Fang, J. Zhou, C. Liang, Y. Cai, A. Pan, X. Tan, Y. Tang, S. Liang, *J. Mater. Chem. A* **2016**, 4, 14408.
- [108] R. Chen, Z. Wang, Z. Chen, P. Wang, G. Fang, J. Zhou, X. Tan, S. Liang, *J. Alloys Compd.* **2019**, 772, 852.
- [109] S. Li, M. Chen, G. Fang, L. Shan, X. Cao, J. Huang, S. Liang, J. Zhou, *J. Alloys Compd.* **2019**, 801, 82.
- [110] L. Deng, X. Niu, G. Ma, Z. Yang, L. Zeng, Y. Zhu, L. Guo, *Adv. Funct. Mater.* **2018**, 28, 1800670.
- [111] Y. Hao, S. Zhang, P. Tao, T. Shen, Z. Huang, J. Yan, Y. Chen, *ChemNanoMat* **2020**, 6, 797.
- [112] Z. Tong, R. Yang, S. Wu, D. Shen, T. Jiao, K. Zhang, W. Zhang, C.-S. Lee, *Small* **2019**, 15, 1901272.
- [113] S. Bach, A. Boudaoud, N. Emery, R. Baddour-Hadjean, J. P. Pereira-Ramos, *Electrochim. Acta* **2014**, 119, 38.
- [114] J. H. Jo, J.-Y. Hwang, J. U. Choi, H. J. Kim, Y.-K. Sun, S.-T. Myung, *J. Power Sources* **2019**, 432, 24.
- [115] Z. Tomkowicz, A. Szytula, *Solid State Commun.* **1977**, 21, v.
- [116] E. Vielhaber, R. Hoppe, *Z. Anorg. Allg. Chem.* **1969**, 369, 14.
- [117] S. C. Han, W. B. Park, K.-S. Sohn, M. Pyo, *J. Solid State Electrochem.* **2019**, 23, 3135.
- [118] D.-W. Jung, J.-H. Jeong, E.-S. Oh, *J. Alloys Compd.* **2017**, 690, 42.
- [119] H. Kim, D.-H. Seo, A. Urban, J. Lee, D.-H. Kwon, S.-H. Bo, T. Shi, J. K. Papp, B. D. McCloskey, G. Ceder, *Chem. Mater.* **2018**, 30, 6532.
- [120] C. Delmas, C. Fouassier, P. Hagenmuller, *Physica B+C* **1980**, 99, 81.
- [121] J.-Y. Hwang, J. Kim, T.-Y. Yu, S.-T. Myung, Y.-K. Sun, *Energy Environ. Sci.* **2018**, 11, 2821.
- [122] N. Naveen, S. C. Han, S. P. Singh, D. Ahn, K.-S. Sohn, M. Pyo, *J. Power Sources* **2019**, 430, 137.
- [123] V. Anisimov, D. Boukhalvalov, T. Rice, *Phys. Rev. B* **1999**, 59, 7901.
- [124] Y. C. Hou, S. J. Jenkins, D. A. King, *Surf. Sci.* **2004**, 550, L27.
- [125] R. Hoppe, H. Sabrowsky, *Z. Anorg. Allg. Chem.* **1965**, 339, 144.
- [126] S. Wang, C. Sun, N. Wang, Q. Zhang, *J. Mater. Chem. A* **2019**, 7, 10138.
- [127] C. Ma, J. Alvarado, J. Xu, R. J. Clément, M. Kodur, W. Tong, C. P. Grey, Y. S. Meng, *J. Am. Chem. Soc.* **2017**, 139, 4835.
- [128] Y. Shen, S. Birgisson, B. B. Iversen, *J. Mater. Chem. A* **2016**, 4, 12281.
- [129] Y.-E. Zhu, X. Qi, X. Chen, X. Zhou, X. Zhang, J. Wei, Y. Hu, Z. Zhou, *J. Mater. Chem. A* **2016**, 4, 11103.
- [130] Z. Lu, J. R. Dahn, *J. Electrochem. Soc.* **2001**, 148, A1225.

- [131] J. H. Jo, J. U. Choi, Y. J. Park, Y. H. Jung, D. Ahn, T.-Y. Jeon, H. Kim, J. Kim, S.-T. Myung, *Adv. Energy Mater.* **2020**, *10*, 1903605.
- [132] X. Wang, P. Hu, C. Niu, J. Meng, X. Xu, X. Wei, C. Tang, W. Luo, L. Zhou, Q. An, L. Mai, *Nano Energy* **2017**, *35*, 71.
- [133] T. Masese, K. Yoshii, K. Tada, M. Kato, S. Uchida, K. Kubota, T. Ina, T. Okumura, Z.-D. Huang, J. Furutani, Y. Orikasa, H. Senoh, S. Tanaka, M. Shikano, *Energy Technol.* **2020**, *8*, 2000039.
- [134] J. U. Choi, J. Kim, J.-Y. Hwang, J. H. Jo, Y.-K. Sun, S.-T. Myung, *Nano Energy* **2019**, *61*, 284.
- [135] X. Zhang, Y. Yang, X. Qu, Z. Wei, G. Sun, K. Zheng, H. Yu, F. Du, *Adv. Funct. Mater.* **2019**, *29*, 1905679.
- [136] P. Bai, K. Jiang, X. Zhang, J. Xu, S. Guo, H. Zhou, *ACS Appl. Mater. Interfaces* **2020**, *12*, 10490.
- [137] K. Sada, P. Barpanda, *Chem. Commun.* **2020**, *56*, 2272.
- [138] J. Weng, J. Duan, C. Sun, P. Liu, A. Li, P. Zhou, J. Zhou, *Chem. Eng. J.* **2020**, *392*, 123649.
- [139] Y.-S. Xu, Q.-H. Zhang, D. Wang, J.-C. Gao, X.-S. Tao, Y. Liu, Y.-G. Sun, L. Gu, B.-B. Chang, C.-T. Liu, S.-Q. Shi, A.-M. Cao, *Energy Storage Mater.* **2020**, *31*, 20.
- [140] W. Xue, M. Huang, Y. Li, Y. G. Zhu, R. Gao, X. Xiao, W. Zhang, S. Li, G. Xu, Y. Yu, *Nat. Energy* **2021**, *6*, 495.
- [141] X. Li, J. Liu, M. N. Banis, A. Lushington, R. Li, M. Cai, X. Sun, *Energy Environ. Sci.* **2014**, *7*, 768.
- [142] G.-T. Park, N.-Y. Park, T.-C. Noh, B. Namkoong, H.-H. Ryu, J.-Y. Shin, T. Beierling, C. S. Yoon, Y.-K. Sun, *Energy Environ. Sci.* **2021**, *14*, 5084.
- [143] J. Y. Hwang, S. T. Myung, C. S. Yoon, S. S. Kim, D. Aurbach, Y. K. Sun, *Adv. Funct. Mater.* **2016**, *26*, 8083.
- [144] C. Liu, S. Luo, H. Huang, Z. Wang, A. Hao, Y. Zhai, Z. Wang, *Electrochim. Commun.* **2017**, *82*, 150.
- [145] Q. Deng, F. Zheng, W. Zhong, Q. Pan, Y. Liu, Y. Li, G. Chen, Y. Li, C. Yang, M. Liu, *Chem. Eng. J.* **2020**, *392*, 123735.
- [146] R. Dang, N. Li, Y. Yang, K. Wu, Q. Li, Y. L. Lee, X. Liu, Z. Hu, X. Xiao, *J. Power Sources* **2020**, *464*, 228190.
- [147] L. Duan, Y. Xu, Z. Zhang, J. Xu, J. Liao, J. Xu, Y. Sun, Y. He, X. Zhou, *J. Mater. Chem. A* **2021**, *9*, 22820.
- [148] J. U. Choi, J. Kim, J. H. Jo, H. J. Kim, Y. H. Jung, D.-C. Ahn, Y.-K. Sun, S.-T. Myung, *Energy Storage Mater.* **2020**, *25*, 714.
- [149] J.-Y. Hwang, J. Kim, T.-Y. Yu, H.-G. Jung, J. Kim, K.-H. Kim, Y.-K. Sun, *J. Mater. Chem. A* **2019**, *7*, 21362.
- [150] J. Liang, C. Lin, X. Meng, M. Liang, J. Lai, X. Zheng, Q. Huang, L. Liu, Z. Shi, *J. Mater. Chem. A* **2021**, *9*, 17261.
- [151] L. Liu, J. Liang, W. Wang, C. Han, Q. Xia, X. Ke, J. Liu, Q. Gu, Z. Shi, S. Chou, *ACS Appl. Mater. Interfaces* **2021**, *13*, 28369.
- [152] X. Zhang, D. Yu, Z. Wei, N. Chen, G. Chen, Z. X. Shen, F. Du, *ACS Appl. Mater. Interfaces* **2021**, *13*, 18897.
- [153] Y.-S. Xu, Y.-N. Zhou, Q.-H. Zhang, M.-Y. Qi, S.-J. Guo, J.-M. Luo, Y.-G. Sun, L. Gu, A.-M. Cao, L.-J. Wan, *Chem. Eng. J.* **2021**, *412*, 128735.
- [154] Y. Sun, L. Zhao, H. Pan, X. Lu, L. Gu, Y.-S. Hu, H. Li, M. Armand, Y. Ikuhara, L. Chen, X. Huang, *Nat. Commun.* **2013**, *4*, 1870.
- [155] H. Liu, F. C. Strobridge, O. J. Borkiewicz, K. M. Wiaderek, K. W. Chapman, P. J. Chupas, C. P. Grey, *Science* **2014**, *344*, 1252817.
- [156] C. Niu, X. Liu, J. Meng, L. Xu, M. Yan, X. Wang, G. Zhang, Z. Liu, X. Xu, L. Mai, *Nano Energy* **2016**, *27*, 147.
- [157] G. Jia, D. Chao, N. H. Tiep, Z. Zhang, H. J. Fan, *Energy Storage Mater.* **2018**, *14*, 136.
- [158] J. Meng, H. Guo, C. Niu, Y. Zhao, L. Xu, Q. Li, L. Mai, *Joule* **2017**, *1*, 522.
- [159] Y. Yang, X. Liu, Z. Dai, F. Yuan, Y. Bando, D. Golberg, X. Wang, *Adv. Mater.* **2017**, *29*, 1606922.
- [160] O. A. Bulavchenko, Z. S. Vinokurov, T. N. Afonassenko, P. G. Tsyrl'nikov, S. V. Tsybul'ya, A. A. Saraev, V. V. Kaichev, *Dalton Trans.* **2015**, *44*, 15499.
- [161] M. S. Islam, C. A. Fisher, *J. Chem. Soc. Rev.* **2014**, *43*, 185.
- [162] Q. Yu, J. Hu, W. A. Wang, Y. Li, G. Suo, L. Zhang, K. Xi, F. Lai, D. Fang, *Chem. Eng. J.* **2020**, *396*, 125218.
- [163] L. Deng, T. Wang, Y. Hong, M. Feng, R. Wang, J. Zhang, Q. Zhang, J. Wang, L. Zeng, Y. Zhu, L. Guo, *ACS Energy Lett.* **2020**, *5*, 1916.
- [164] K. Lei, Z. Zhu, Z. Yin, P. Yan, F. Li, J. Chen, *Chem* **2019**, *5*, 3220.
- [165] B. Peng, Y. Li, J. Gao, F. Zhang, J. Li, G. Zhang, *J. Power Sources* **2019**, *437*, 226913.
- [166] C.-I. Liu, S.-h. Luo, H.-b. Huang, X. Liu, Y.-c. Zhai, Z.-w. Wang, *Chem. Eng. J.* **2019**, *378*, 122167.
- [167] Q. Zhang, C. Didier, W. K. Pang, Y. Liu, Z. Wang, S. Li, V. K. Peterson, J. Mao, Z. Guo, *ACS Energy Mater.* **2019**, *9*, 1900568.
- [168] K. Sada, P. Barpanda, *Chem. Commun.* **2020**, *56*, 2272.
- [169] M. K. Cho, J. H. Jo, J. U. Choi, S.-T. Myung, *ACS Appl. Mater. Interfaces* **2019**, *11*, 27770.
- [170] J. U. Choi, Y. J. Park, J. H. Jo, Y. H. Jung, D.-C. Ahn, T.-Y. Jeon, K.-S. Lee, H. Kim, S. Lee, J. Kim, *Energy Storage Mater.* **2020**, *27*, 342.
- [171] M. G. T. Nathan, N. Naveen, W. B. Park, K.-S. Sohn, M. Pyo, *J. Power Sources* **2019**, *438*, 226992.
- [172] Z. Xiao, J. Meng, F. Xia, J. Wu, F. Liu, X. Zhang, L. Xu, X. Lin, L. Mai, *Energy Environ. Sci.* **2020**, *13*, 3129.
- [173] S. Xu, C. Bao, M. Yu, S. Liu, L. Chen, D. Zhang, *Mater. Lett.* **2020**, *270*, 127733.
- [174] C.-I. Liu, S.-h. Luo, H.-b. Huang, Y.-c. Zhai, Z.-w. Wang, *Electrochim. Acta* **2018**, *286*, 114.
- [175] W. Zhong, X. Liu, Q. Cheng, T. Tan, Q. Huang, Q. Deng, J. Hu, C. Yang, *Appl. Phys. Rev.* **2021**, *8*, 031412.
- [176] L. Liu, J. Liang, W. Wang, C. Han, W. Li, *ACS Appl. Mater. Interfaces* **2021**, *13*, 28369.
- [177] M. Aykol, S. Kim, V. I. Hegde, D. Snyder, Z. Lu, S. Hao, S. Kirklın, D. Morgan, C. Wolverton, *Nat. Commun.* **2016**, *7*, 13779.
- [178] L. Kahle, A. Marcolongo, N. Marzari, *Energy Environ. Sci.* **2020**, *13*, 928.
- [179] M.-F. Ng, J. Zhao, Q. Yan, G. J. Conduit, Z. W. Seh, *Nat. Mach. Intell.* **2020**, *2*, 161.
- [180] R. Xiao, H. Li, L. Chen, *J. Mater. Chem. A* **2020**, *8*, 5157.
- [181] P. M. Attia, A. Grover, N. Jin, K. A. Severson, T. M. Markov, Y.-H. Liao, M. H. Chen, B. Cheong, N. Perkins, Z. Yang, P. K. Herring, M. Aykol, S. J. Harris, R. D. Braatz, S. Ermon, W. C. Chueh, *Nature* **2020**, *578*, 397.
- [182] A. Garg, S. Singh, W. Li, L. Gao, X. Cui, C.-T. Wang, X. Peng, N. Rajasekar, *Int. J. Energy Res.* **2020**, *44*, 9513.
- [183] R. P. Joshi, J. Eickholt, L. Li, M. Fornari, V. Barone, J. E. Peralta, *ACS Appl. Mater. Interfaces* **2019**, *11*, 18494.
- [184] K. Yu, X. Pan, G. Zhang, X. Liao, X. Zhou, M. Yan, L. Xu, L. Mai, *Adv. Energy Mater.* **2018**, *8*, 1802369.
- [185] G. Li, Q. Li, L. Li, J. Fan, Q. Ge, D. Xie, J. Zheng, G. Li, *Appl. Surf. Sci.* **2018**, *427*, 226.
- [186] C. Tian, F. Lin, M. M. Doeff, *Acc. Chem. Res.* **2018**, *51*, 89.
- [187] W. Zhang, Y. Liu, Z. Guo, *Sci. Adv.* **2019**, *5*, eaav7412.
- [188] X. Wang, K. Han, D. Qin, Q. Li, C. Wang, C. Niu, L. Mai, *Nanoscale* **2017**, *9*, 18216.
- [189] Y. Xing, W. He, M. Pecht, K. L. Tsui, *Appl. Energy* **2014**, *113*, 106.



**Xuanpeng Wang** is an Assistant Professor at the School of Science, Wuhan University of Technology (WUT). He received his Ph.D. degree from WUT in 2019. His current research focuses on material synthesis, device design, in situ characterization of new-type potassium-ion batteries and sodium-ion batteries.



**Liqiang Mai** is the Chair Professor of Materials Science and Engineering at WUT, Dean of School of Materials Science and Engineering at WUT, Fellow of the Royal Society of Chemistry. He received his Ph.D. from WUT in 2004 and carried out his postdoctoral research at Georgia Institute of Technology in 2006–2007. He worked as an Advanced Research Scholar at Harvard University and University of California, Berkeley. His current research interests focus on new nanomaterials for electrochemical energy storage and micro/nano energy devices.